University of Nevada, Reno

# Evaluation of a Multiwavelength Characterization of Brown and Black Carbon from Filter Samples

A thesis submitted in partial fulfillment of the requirements
for the degree of Master of Science in Atmospheric Science

By

Megan M. Johnson

Dr. John G. Watson/Thesis Advisor

December, 2015

THE GRADUATE SCHOOL

We recommend that the thesis
prepared under our supervision by

**MEGAN M. JOHNSON**

Entitled

**Evaluation Of A Multiwavelength Characterization Of Brown And Black Carbon From Filter Samples**

be accepted in partial fulfillment of the
requirements for the degree of

MASTER OF SCIENCE

John G. Watson, Advisor

Judith C. Chow, Committee Member

W. Patrick Arnott, Graduate School Representative

David W. Zeh, Ph.D., Dean, Graduate School

December, 2015

**Abstract**

An ultraviolet – visible (UV-VIS) spectrometer coupled with an integrating sphere was used to measure diffuse reflectance and transmittance of particulate matter (PM) samples collected on quartz-fiber (QF) and Teflon-membrane (TM) filter media over the wavelength range 250 – 1000 nm at 1 nm resolution. These measurements were used to calculate PM sample attenuation, absorption, and Ångstrom absorption exponents (AAE). Samples included laboratory generated source samples (e.g. biomass burning emissions, diesel engine exhaust, and resuspended dusts) and ambient samples. PM sample attenuation and absorption were compared to other PM light absorption measurement methods including densitometer, dual-wavelength (370 & 880 nm) transmissometer, and 3-$\lambda$ (405, 532, 781 nm) photoacoustic spectrometer (PAS). Large differences were found between filter-based methods and QF and TM absorption was found to be higher than PAS by average factors of 5.1 and 3.6, respectively. AAE values calculated for all samples compared well with values previously reported in literature. Comparison of the filter media showed that attenuation and absorption values from TM samples are, on average, ~1/2 of the values obtained using QF samples. Filter media comparison also revealed evidence of shadowing effects on TM filter media with high sample loading. Comparison of absorption approximation methods using various AAEs and a power law extrapolation exhibited large differences in radiative forcing estimates, indicating that PM absorption is not always well represented by the power law assumption.

**Acknowledgements**

I would like to first thank my advisory committee for their guidance and critiques of this research. I would also like to extend thanks to Joseph Knue for his tireless sampling assistance; to Brenda Cristani, Steve Kohl, and Matthew Tompkins for their immeasurable knowledge and aid in the laboratory; to Tasha Pascal and Gustavo Riggio for their valuable feedback; and to Robert David for the unwavering encouragement. Finally, I wish to express my gratitude for my parents' continued support throughout my academic endeavors.

**Table of Contents**

## List of Tables

## List of Figures

# 1. Introduction

## 1.1 Background

Particulate matter (PM) is an important constituent of the Earth's climate system. Aerosolized PM scatters and absorbs solar radiation and thereby affects visibility (Watson 2002), the Earth's radiation balance, and properties and lifetimes of clouds (IPCC 2013). Fine PM (with an aerodynamic diameter < 2.5 μm) has adverse effects on human health (Pope et al., 2009). PM that contains large fractions of sulfate, nitrate, and/or sea salt scatters more light than it absorbs, there by causing a cooling effect. Carbonaceous PM that absorbs strongly at visible wavelengths ($\lambda$ = 400-700 nm) is referred to as light absorbing carbon (LAC) and causes a warming effect. LAC is made up of black carbon (BC), also referred to as elemental carbon (EC) or soot, and brown carbon (BrC), a class of organic carbon (OC) that absorbs more strongly than BC at shorter (< 600 nm) wavelengths (Andreae and Gelencser 2006). Understanding PM light absorption at multiple wavelengths is needed to reduce the uncertainty of anthropogenic radiative forcing (RF) (IPCC 2013) and visibility degradation.

## 1.2 Light Absorption by Particulate Matter

When light interacts with PM it is either scattered or absorbed. When light is scattered, it is diverted from the direction in which it was originally travelling. Absorbed light heats the PM and is re-radiated at longer (infrared) wavelengths that heat the

surrounding air. Magnitudes of PM light scattering and absorption depend on the wavelength of the incident light, the particle size distribution, particle shape and composition (Petty 2006, Chakrabarty et al., 2007, Moosmüller et al., 2009).

The degree of particle scattering and absorption varies with the ratio of its diameter ($d_p$) to the incident wavelength ($\lambda$), a relationship often expressed as the size parameter, $x$:

$$x = \frac{\pi d_p}{\lambda} \tag{1}$$

When $x \ll 1$, the particle is small compared to the incident wavelength and this is referred to as the Rayleigh scattering regime. In this regime a particle's scattering cross section is proportional to $\lambda^{-4}$, so shorter wavelengths are scattered more efficiently than longer wavelengths. For example, blue light (~450 nm) is scattered more efficiently than red light (~650 nm) by air molecules, resulting in blue skies and red sunsets. (Petty 2006). Absorption by particles in this regime is proportional to the particle volume when the penetration depth ($\lambda/4\pi k$) is larger than $d_p$ (Petty 2006, Moosmüller et al., 2009).

The complex refractive index of a particle (N) is written as:

$$N = n + ik \tag{2}$$

where $n$ and $k$ are the real and imaginary parts of the refractive index, respectively, and $i$ is the imaginary quantity equal to the square root of -1. Both n and k are wavelength dependent properties. A non-absorbing particle would have a refractive index

comprised only of $n$. The refractive index of the particle ($N$) is usually normalized by the refractive index of the medium ($N_0$) which surrounds it, as

$$m = \frac{N}{N_o} \tag{3}$$

For atmospheric applications this medium is air, for which $N_0 = \sim 1$. So $m = N$, making Equation (2) (Petty 2006, Moosmüller et al., 2009, Arnott 2014):

$$m = n + ik \tag{4}$$

When $x \cong 1$, the particle is approximately the same size as the incident wavelength and this is called the Mie regime. Mie theory can be applied to spheres of any size to calculate scattering and absorption cross sections and the scattering phase function. Particles that fall within the Mie regime ($x \cong 1$) exhibit large scattering and absorption efficiencies due to internal resonances and they absorb proportionally to their mass, depending in the penetration depth (Moosmüller et al., 2009, Arnott 2014). The lower size limit ($x \ll 1$) of Mie theory is equivalent to the Rayleigh approximation for small spheres, while the upper size limit ($x \gg 1$) can be accurately approximated using geometric optics (Petty 2006, Moosmüller et al., 2009).

When $x \gg 1$, the particle is large compared to the incident wavelength and this is called the geometric Regime. Particles in the geometric regime absorb light proportional to their surface area, depending on the penetration depth (Arnott 2014). Geometric

optics, or ray tracing, is more applicable to large cloud ice particles and raindrops, and is used to explain phenomena such as rainbows and sundogs (Petty 2006).

Most PM, with $d_p$ between 0.01 and 10 μm, falls into the Mie or Rayleigh regimes at wavelengths of interest for RF and visibility (visible to thermal infrared, 0.4 – 100 μm). Figure 1-1 illustrates the approximate boundaries of the scattering regimes with respect to particle radius and wavelength of light.

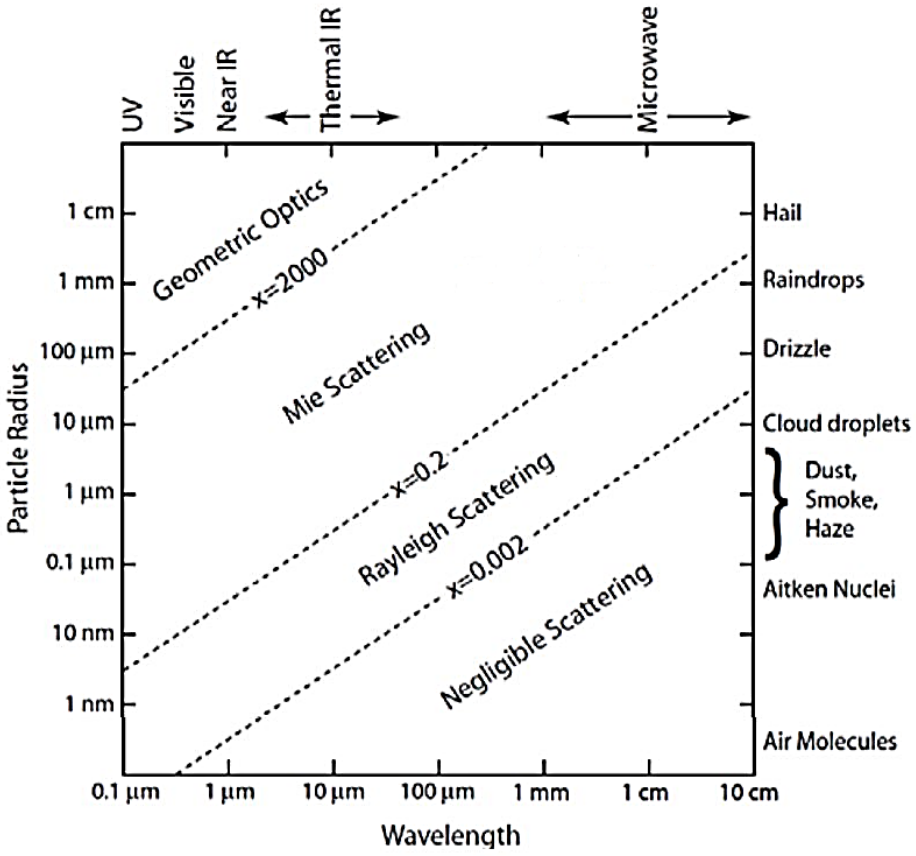


**Figure 1-1.** Scattering regimes defined as a function of particle size and wavelength of incident radiation (Petty 2006).

Moosmüller et al. (2009) outline the typical methods and terminology of expressing scattering and absorption properties of PM:

- Extinction – sum of scattering and absorption
- Extinction/Scattering/Absorption cross section ($\sigma_{ext/sca/abs}$) – used to characterize extinction/scattering/absorption of an individual particle. Expressed as area, usually $m^2$. The extinction cross section is the sum of the scattering and absorption cross sections.

$$\sigma_{ext} = \sigma_{sca} + \sigma_{abs} \tag{5}$$

- Extinction/Scattering/Absorption Efficiency ($Q_{ext/sca/abs}$) – ratio of the respective cross section to the geometric cross section (if particle is spherical, $\sigma_{geo} = \pi r^2$).

$$Q_{abs} = \frac{\sigma_{abs}}{\sigma_{geo}} \tag{6}$$

- Absorption coefficient ($\beta_{abs}$) – Equal to the sum of the particles' absorption cross sections divided by the volume of air, as shown in Equation (7). Units of inverse distance, typically reported as inverse megameters ($Mm^{-1}$).

$$\beta_{abs} = \frac{\sum_{i=1}^{n} \sigma_{abs\_i}}{V} \tag{7}$$

- Single scattering albedo (SSA or ω) – for numerous particles, the ratio of the scattering coefficient and the extinction coefficient. An SSA of 1 represents a purely scattering particle and an SSA of 0 represents a completely absorbing particle.

$$\omega = \frac{\beta_{sca}}{\beta_{ext}} = \frac{\beta_{sca}}{\beta_{sca} + \beta_{abs}} \tag{8}$$

- Mass absorption efficiency ($E_{abs}$) – in units of $m^2/g$. Absorption coefficient ($\beta_{abs}$) divided by the mass concentration of the absorber, usually EC ($\mu g/m^3$) :

$$E_{abs} = \frac{\beta_{abs}}{[EC]} \tag{9}$$

- Absorption Ångström exponent – power-law expression for wavelength dependence of an optical property, such as the absorption coefficient:

$$\frac{\beta_{abs}(\lambda_1)}{\beta_{abs}(\lambda_2)} = \left(\frac{\lambda_1}{\lambda_2}\right)^{-AAE} \tag{10}$$

This relationship with scattering coefficients would give the Scattering Ångström exponent ($SAE$). The AAE can be calculated using two wavelengths, as indicated in Equation (10), but it can also be approximated using a power-law curve fit equation of multiple data points as:

$$\beta_{abs\,(\lambda)} = \frac{C}{\lambda^{AAE}} \tag{11}$$

where $C$ is a constant and $\lambda$ is the wavelength.

### 1.3 Importance for Radiative Forcing (RF)

RF is a change imposed on the Earth's radiation balance, or a change in the radiative flux (incoming minus outgoing) at some level of the atmosphere. Direct RF affects the Earth's radiation balance through gas or PM scattering and absorption (i.e. volcanic eruptions will have a cooling effect) while indirect RF affects the radiation balance by first affecting something else, like cloud formation through droplet nucleation on small particles or droplet evaporation through heating from LAC within the droplet (Seinfeld and Pandis, 2006).

One of the large uncertainties left in understanding contributions to anthropogenic RF is that of aerosols. The IPCC (2013) states that "the large uncertainty in aerosol ERF (effective radiative forcing) is the dominant contributor to overall net Industrial Era forcing uncertainty." As defined by IPCC, ERF is the "change in net downward radiative flux at the top of the atmosphere (TOA) after allowing for atmospheric temperatures, water vapor, clouds and land albedo to adjust, but with global mean surface temperature or ocean and sea ice conditions unchanged (IPCC, 2013)."

Measuring the light absorption of PM collected on filters at multiple wavelengths can help constrain the uncertainty in aerosol ERF and thus the net Industrial Era forcing. Measuring archived PM filter samples can provide historical insight into changes in RF due to changes in PM sources and emissions.

## 1.4 Importance for Visibility

PM light scattering and absorption affects visual air quality. Scattering has a greater effect on visibility than absorption because the scattering introduces a radiation source along the sight path (Petty 2006), thereby reducing the contrast of the object being viewed.

Visual range is the greatest distance at which an object can be clearly detected (Pitchford and Malm 1994, Petty 2006). The extinction coefficient ($\beta_{ext}$) has been used as a measurement of visibility with respect to pollutant concentrations. Visual range and

$\beta_{ext}$ are approximately inversely proportional, and are also not linear with perceived visual scene changes caused by haze (Pitchford and Malm, 1994). Due to this non-linearity, a "haziness" index was developed to be linear with respect to fractional changes in $\beta_{ext}$. This index is measured in units of deciview (dv) and follows the relationship:

$$haziness\ (dv) = 10 \ln\left(\frac{\beta_{ext}}{0.01}\right) \tag{12}$$

where $\beta_{ext}$ is in units of $km^{-1}$ (Pitchford and Malm, 1994).

In 1999, the U.S. Environmental Protection Agency (EPA) issued a Regional Haze Rule (RHR) to protect and improve visibility in national parks and wilderness areas (U.S.EPA 1999a). This rule set out to achieve the visibility goals set forth by the Clean Air Act (CAA), specifically the 1977 amendment that called for "the prevention of any future, and the remedying of any existing, impairment of visibility in the mandatory Class I areas which impairment results from manmade air pollution"(U.S.EPA 1999b).

Due to long-range transport of $PM_{2.5}$, many states are affected by the RHR even if the state does not contain one of the 156 designated mandatory Class I areas. Participation includes planning, analysis, and emission controls. States are required to create long-term strategies to achieve natural background visibility conditions by 2065 (U.S.EPA 1999b). Natural visibility conditions are defined as "the atmospheric state where visibility would be imperceptibly different from that which would exist in the absence of any man-made emissions in the world"(Tombach and Pitchford 2007).

Transport of man-made emissions from other countries, like Canada, Mexico and Asia cannot be controlled by the U.S. This makes the differentiation of source regions and source types important for attaining future visibility goals.

Under the RHR, the Interagency Monitoring of Protected Visual Environments (IMPROVE) network was expanded from 30 to over 100 sites by 2002. These sites provide 24 hour mass concentrations of coarse ($PM_{10}$) and fine ($PM_{2.5}$) PM, as well as $PM_{2.5}$ chemical concentrations (e.g. elements, ions and carbon fractions) (Tombach and Pitchford 2007).

Some IMPROVE sites have nephelometers, which measure the scattering coefficient of sampled air, but many do not. Chemical light extinction is calculated using an algorithm that multiplies $PM_{2.5}$ constituent concentrations measured at IMPROVE sites by typical extinction efficiencies and relative humidity functions. The algorithm was revised in 2005 to include more recent understanding of aerosol optical properties (Pitchford et al., 2007, Tombach and Pitchford 2007). The algorithm is listed in Equation (13), where all constituents are in units of $\mu g/m^3$ except $NO_2$.

$$\begin{aligned}\beta_{ext}(Mm^{-1}) \approx 2.2 \times f_S(RH) \times [Small\ Sulfate] \\ + 4.8 \times f_L(RH) \times [Large\ Sulfate] \\ + 2.4 \times f_S(RH) \times [Small\ Nitrate] \\ + 5.1 \times f_L(RH)[Large\ Nitrate] \\ + 2.8 \times [Small\ Organic\ Mass] \\ + 6.1 \times [large\ Organic\ Mass] \\ + 10 \times [Elemental\ Carbon] \\ + 1 \times [Fine\ Soil] \\ + 1.7 \times f_{SS}(RH) \times [Sea\ Salt] \\ + 0.6 \times [Coarse\ Mass] \\ + Rayleigh\ Scattering\ (site\ specific) \\ + 0.33 \times [NO_2(ppb)]\end{aligned} \quad (13)$$

where $[Organic\ Mass] = 1.8\ x\ [Organic\ Carbon]$,

$$[Large\ Sulfate] = \frac{[Total\ Sulfate]}{20\frac{\mu g}{m^3}} \times [Total\ Sulfate], \text{for } [Total\ Sulfate] < 20\frac{\mu g}{m^3}$$

$$[Large\ Sulfate] = [Total\ Sulfate], \text{for } [Total\ Sulfate] \geq 20\frac{\mu g}{m^3}$$

and $[Small\ Sulfate] = [Total\ Sulfate] - [Large\ Sulfate]$. These small and large fraction equations are also used to apportion small and large fractions of Nitrate and Organic Mass. The algorithm produces an estimate of $\beta_{ext}$, which is then converted to deciviews using Equation (12). The mean of the 20% worst hazy days at each IMPROVE site defines the benchmark for improving visibility. The 20$^{th}$-percentile of poorest visibility days need to reach the natural visibility conditions by 2065 without degrading the mean of the 20$^{th}$-percentile of the best visibility days. However, Park et al. (2006) observed that some of the 20% worst days show important contributions of pollution from Canada and Mexico, which cannot be controlled by the U.S. These means were to be determined during the baseline period of 2000 – 2004 and linear rates of reduction for the deciview

values were calculated to provide reduction goals (Pitchford et al., 2007). Improvements in visibility have already been observed, though at lower rates in the western U.S. than in the east (Hand et al., 2014), mainly due to already low sulfur dioxide emissions compared to those in the eastern U.S.

## 1.5 PM of Importance to RF and Visibility

### 1.5.1 Light Absorbing Carbon (LAC)

LAC is the general term for all carbonaceous substances that absorb light. This includes what is conventionally referred to as BC and BrC.

BC is a strong absorber across all wavelengths and thus appears visually black. The term BC is used to describe many types of visually black carbon, including soot and EC (thermal EC is operationally defined as the fraction of carbon that is oxidized above a certain temperature threshold) (Andreae and Gelencser 2006). EC and BC are products of high temperature combustion and are typically found in exhausts from fossil fuel burning (e.g. coal and petroleum products) and flaming biomass (e.g. residential wood burning and wildfires). Freshly emitted BC particles, termed "soot carbon" by Andreae and Gelencsér (2006), form long fractal aggregates. The individual monomers that make up these chains tend to fall into the Rayleigh regime ($x \ll 1$) which means scattering is small at most visible wavelengths and $\sigma_{abs}$ is proportional to particle volume. However as these particles age, they collapse into larger spherical particles which tend to absorb proportional to their surface area (Moosmüller et al., 2009, Arnott 2014). Aged BC

particles can also acquire coatings which may alter their scattering and absorption properties (Lack and Cappa 2010). BC has a large imaginary component of its refractive index ($k$) that is independent of wavelength in the visible and near-visible spectral ranges (~450 – 1000 nm). This means that the $AAE$ for BC is theoretically inversely proportional to the wavelength of radiation ($\lambda^{-1}$) (Moosmüller et al., 2009).

BrC is a more loosely defined term which encompasses light absorbing organic carbon. BrC does not absorb as strongly as BC across the entire spectrum, but it absorbs more strongly at shorter, ultraviolet (UV) and visible wavelengths (250-700 nm) and often appears yellow or brown (Kirchstetter et al., 2004b, Andreae and Gelencser 2006). This means the $k$ value of BrC is wavelength dependent and $AAE$ values can be much larger than 1 (Kirchstetter et al., 2004b, Andreae and Gelencser 2006, Moosmüller et al., 2009). Absorption at these shorter wavelengths alters RF (0.1 – 0.25 W/m$^2$, ~25% of BC RF, (Feng et al., 2013) and can affect concentrations of photochemically active gaseous compounds like ozone and hydroxyl radicals (Li et al., 2011). BrC is produced through low-temperature combustion (i.e. smoldering biomass) and photo-oxidation of biogenic materials (Kirchstetter et al., 2004b, Andreae and Gelencser 2006). The optical properties of BrC are variable and are dependent on the temperature of combustion, the moisture content of the fuel and the type of fuel. It is thought that BrC emissions are highest in areas with large amounts of biomass burning, like Asia, South America, and sub-Saharan Africa (Chakrabarty et al., 2014).

### 1.5.2. Mineral Dust (MD)

Mineral dust (MD) is important to consider, especially when discerning international transport of pollution. While MD contributes to light extinction through scattering, MD absorption is also important to understand at shorter wavelengths (Yang et al., 2009).

## 1.6 Light Absorption Measurement Methods

Many instruments that measure PM $\beta_{abs}$ have used light at near-infrared (NIR; e.g., 880 nm) or red (e.g., 633 nm) wavelengths. Measuring $\beta_{abs}$ at multiple wavelengths, especially between 350-600 nm, allows for contributions from BC and BrC to be differentiated, which can help to determine emission sources and ERF effects. The ratio of $\beta_{abs}$ (350 nm) to $\beta_{abs}$ (880 nm) has been used to separate biomass smoldering from other $PM_{2.5}$ contributions in communities with large amounts of residential wood combustion (Sandradewi et al., 2008a, Sandradewi et al., 2008b). Yang et al. (2009) used wavelength dependent aethalometer measurements to apportion light absorption to BC, BrC, and dust in China. Detailed absorption spectra can also help distinguish among different dust contributions (Tomza et al., 2001, Fialho et al., 2005).

For filter-based PM absorption measurements, $\beta_{abs}$ is typically obtained using the difference in the reflection or transmission of light through a filter before and after PM sampling (i.e. the fundamentals of Beer's Law). Filter-based measurements are advantageous because they are simple, cheap, and don't measure absorption due to

gases. These measurements, however, are subject to effects caused by the filter, including multiple scattering enhancement due to the filter media, particle shadowing effects, and particle morphology after contact with the filter (Petzold and Schönlinner 2004, Arnott et al., 2005, Cappa et al., 2008, Lack et al., 2008, Moosmüller et al., 2009, Presser et al., 2014). If not properly accounted for, these measurement methods can systematic biases for PM light absorption. Light transmitted through the PM-loaded filter is more attenuated than that caused solely by the PM deposit, resulting in an overestimation of $\beta_{abs}$, but still highly correlated with the true atmospheric absorption.

Many filter-based methods for measuring PM absorption use an integrating plate (IP) or integrating sphere (IS) to diffuse the incident radiation or measure the diffuse reflectance or transmittance from the sample, respectively. These methods characterize the forward and/or back scattering component of the PM sample. Methods or instruments that use IP or IS include the Densitometer Integrating Plate Method (DIPM)(Chow et al., 2010), the Hybrid Integrating Plate System (HIPS)(Campbell et al., 1995), the Particle Soot Absorption Photometer (PSAP), which measures $\beta_{abs}$ on filter substrate continuously (Bond et al., 1999), and the Multi-Angle Absorption Photometer (MAAP), which reports hourly averaged BC in $\mu g/m^3$ using manufacturer assumed $E_{abs}$ (Petzold and Schönlinner 2004). These methods all originally used a white light source or one centered at a single wavelength between 500 and 700 nm. Some have expanded to include one or more additional wavelengths, ranging from the UV to the NIR.

Some filter-based methods can provide real-time measurements, like the PSAP, the MAAP and the aethalometer. The aethalometer is based on light transmittance and uses one or more LEDs at specified wavelengths to measure the attenuation through spots of PM that are continuously sampled onto a filter tape. Reference measurements are made through blank areas of the filter tape (Hansen et al., 1982) and light absorption is calculated using the Beer-Lambert Law (see Section 2.2.2).

In-situ methods provide real-time measurements of aerosol absorption and scattering without the need for collection of PM onto filter media. These techniques also tend to measure the absorption properties of the PM and the surrounding air, so it is important to account for this absorption by making reference measurements (of clean, PM free air) or by using a wavelength that will minimize this absorption. The photoacoustic spectrometer determines the $\beta_{abs}$ by illuminating sampled air with a modulated light source (single or multiwavelength) and measuring the sound emitted. The energy from the absorbed light causes heating, expansion, and thus a sound wave at the frequency of the incident light pulses. The magnitude of the sound emitted is detected with a microphone and is converted to a $\beta_{abs}$ value for the particular wavelength (Moosmüller et al., 1997). The Single Particle Soot Photometer (SP2) estimates BC mass over a limited size range using intracavity laser-induced particle incandescence, which causes the particles in the sampled air to absorb the incident radiation (1064 nm) and heat to a point of incandescence. The radiation emitted from the particles is measured and correlated to BC mass, determined by calibration with

graphite or fullerene dusts. Scattering from the particles is also measured and used to estimate particle size (Droplet Measurement Technologies 2014). The CIMEL sun photometer provides aerosol absorption optical depth (AOD) and SSA of a column of the atmosphere at six wavelength channels (340, 380, 440, 675, 870, and 1020 nm) by measuring direct and diffuse solar radiation at multiple angles (CIMEL Electronique 2015). These instruments are used by many different organizations in the worldwide Aerosol Robotic Network (AERONET), run by the National Aeronautics and Space Administration (NASA)(NASA Goddard Space Flight Center 2015).

## 1.7 Research Objectives and Overview

$PM_{2.5}$ filter samples are routinely acquired in long-term monitoring networks. Multiwavelength measurements on existing filters, including specific source samples (e.g. diesel and gasoline engine exhaust, biomass burning, and dust), can provide additional insight into PM light absorption and chemical properties. In addition, multiwavelength absorption measurements of archived filter samples from speciation monitoring networks (IMPROVE, Chemical Speciation Network) can provide information on spatial and temporal variability in PM light absorption for both visibility and RF research.

By using an ultraviolet-visible spectrometer capable of making diffuse reflectance and transmittance measurements at ~1 nm resolution across the spectral range of 250 – 1000 nm, more information can be gained from existing samples that can:

1) improve understanding of sources and RF of BrC, 2) delineate source contributions affecting visibility in Class I visually protected areas, and 3) constrain climate models. This requires an understanding of light absorption measurements made on quartz-fiber and Teflon-membrane. These filter types are the most widely in compliance networks, speciation networks, and continuous monitors such as the aethalometer, MAAPS and PSAP.

This research aims to narrow the knowledge gaps related to optical properties of BrC and other pollution sources while broadening the pool from which data can be gathered by applying multiwavelength methods to measure a range of filter-based laboratory-generated source samples and ambient samples. The objectives of this project are to 1) compare spectral absorption measurements between quartz-fiber and Teflon-membrane filter types and between absorption measurement instruments, 2) examine the variability of AAE for biomass burning and fossil fuel combustion, and 3) evaluate the extent to which source contributions can be differentiated from ambient samples using light absorption ratios at different wavelengths. The following three hypotheses will be tested:

1. This method can provide comparable data to PM light absorption techniques currently in use.
2. This method can be used to identify BrC, BC and MD in filter samples using absorption spectra, AAE, and reflectance and transmittance spectra.

3. The relationship of absorption of a PM sample to wavelength is not always well represented by the commonly used AAE power law assumption and extrapolation.

## 1.8 Guide to Thesis

Section 1 provides the background to the study and the hypotheses to be tested. Section 2 gives an overview of the instrumentation, filter samples, and analysis methods used for this study. Section 3 presents and discusses the results of the methods tested. Section 4 discusses the main conclusions of this study as well as possibilities for future work.

# 2. Instrumentation and Methods

## 2.1 Description of Instrumentation

### 2.1.1 Components and Diagrams

The ultraviolet – visible (UV-Vis) spectrometer (Lambda 35, PerkinElmer, Waltham, MA) is a commercially available instrument that couples a monochromator with a two-port integrating sphere in order to provide diffuse reflectance and transmittance measurements of a sample. The instrument uses a holographic concave grating with 1053 lines/mm in the center and two lamps (i.e. deuterium and halogen), in order to scan across the wavelength range of 250 – 1000 nm at approximately one nm resolution. The optical path of the Lambda 35 is shown in Figure 2-1and instrument specifications are outlined in Table 2-1.

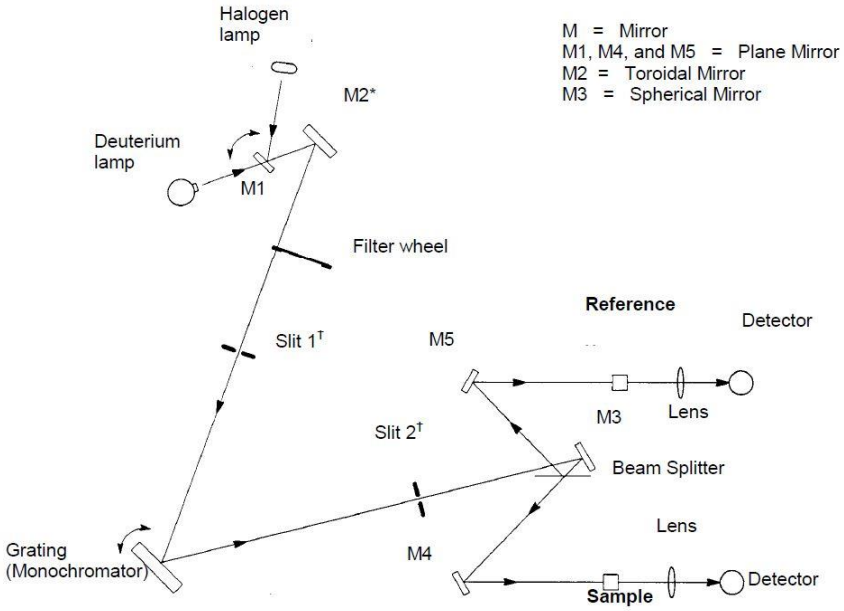


**Figure 2-1.** Optical path of the Lambda 35. Two light sources allow for scans across the wavelength range 250-1000 nm. The beam is split between the sample detector and a reference detector to monitor changes in beam intensity.

**Table 2-1.** Specifications of Lambda 35 UV-Visible Spectrometer

| Observable | Specification |
|---|---|
| Beam Center Height | 15 mm above sample holder base |
| Slit Width | 2 nm |
| Beam Cross-Section | 1 mm x 7.5 mm (width x height) |
| Optical Path Length in Sample Compartment | 121 mm |
| Grating (Monochromator) | Holographic concave grating with 1053 lines/mm in the center |
| Radiation Sources | Pre-aligned deuterium and halogen lamps |
| Wavelength Scan Range | 250 – 1000 nm |
| Scan Speed | 120 nm per minute |
| Data Interval | 1 nm |
| Detectors | Silicon photodiodes (one at base of integrating sphere, other for reference beam) |

To achieve diffuse reflectance and transmittance measurements, the interior of the integrating sphere is coated with Labsphere Spectralon® and equipped with a silicon photodiode detector at the base of the sphere. Spectralon® is a chemically inert, thermally stable (to >400 ºC), porous material which exhibits >99% diffuse reflectance – the highest diffuse reflectance over the UV-Visible-NIR spectrum (250 – 2500 nm) of any known material[1]. Across this spectrum, it is optically flat within ± 4%. It has a National Institute of Standards and technology (NIST) traceable calibration and is used in optical components, as a reflectance standard, and as targets for remote sensing.

The principle of an integrating sphere is to capture all the scattered light (in one or more hemispherical directions) from a sample in order to increase the amount of light which reaches a detector. There are two ports on the integrating sphere: the transmittance port, where light from the monochromator enters the sphere, and the reflectance port, where light would exit the sphere if not blocked. By making reflectance and transmittance measurements of a sample, the forward and backscattering of a sample are both accounted for and it is possible to calculate a sample's absorption. Transmittance and reflectance measurements are made in reference to a Spectralon® 99% reflectance standard, the same material coating the integrating sphere.

Figure 2-2 shows a diagram of the integrating sphere set-up. Samples and Spectralon® reflectance standards are held flush against the sphere ports by sample holders, at either a 0°or 8° angle of incidence. The 8° angle reduces the amount of directly

[1] https://www.labsphere.com/products/category/diffuse-reflectance-coatings-materials/

backscattered light lost through the sphere entrance. In order to place a filter sample in a sample holder, a filter holder was designed using a filter slide as a model and fabricated with a 3-D printer (Makerbot, Brooklyn, NY). Figure 2-3 shows photographs of a filter holder for use with the sample holder.

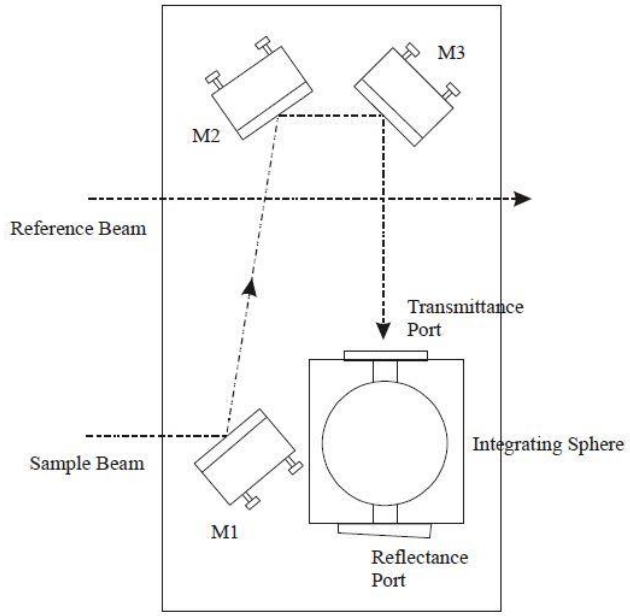


**Figure 2-3.** Diagram of integrating sphere set-up. The detector (not pictured) is located at the bottom of the sphere.

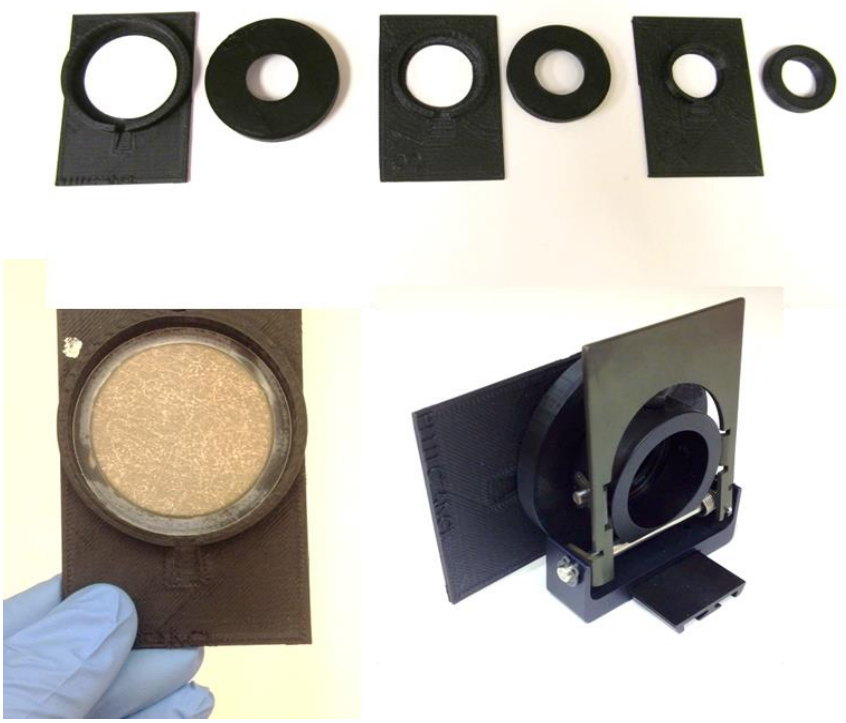

**Figure 2-2.** Filter holders for 47, 37 and 25 mm filters (top row from left to right) and example of 47 mm holder loaded with a filter sample (bottom left). The filter holder in standard Lambda 35 sample holder is shown at bottom right.

### 2.1.2 Optical Standards and Calibration

As stated previously, all reflectance and transmittance measurements are made in reference to a near-perfect reflector (i.e. a 99% Spectralon ® reflectance standard) as the operational calibration standard for the method. Before any samples are measured, two baseline measurements must be made: 100% transmittance (T) and 0% T. The first, 100% T, is made by placing the Spectralon® standard at the reflectance port. The second, 0% T, is made by either blocking the light from entering the sphere or not allowing it to reflect back into the sphere. The set-up for these baseline measurements differ slightly depending on whether reflectance or transmittance measurements are being made, but they essentially define the upper and lower limits of the sample measurements. These procedures are further outlined in Section 2.1.4.

Further performance checks can be conducted using Spectralon® reflectance standards with different degrees of darkening from white to black. Like the 99% standard, these standards are NIST-traceable and are optically flat within ±4% across the 250 – 2500 nm range. As these reflectances are certified by Labsphere, the reflectance measurements of the Spectralon® standards made by the Lambda 35 can be compared with those provided by Labsphere (North Sutton, NH). Figure 2-4 shows the Labsphere Spectralon® standards in the range of 5 to 99% reflectance. The reflectance spectrum of each Spectralon® standard is shown in Figure 2-4.

Wavelength checks, to assure the monochromator is achieving the specified wavelength, can also be made using a protocol within the UV Win Lab software. The protocol instructs the monochromator to position itself to produce a specific wavelength, and the wavelength produced is measured by the detector.

**Figure 2-4.** Spectralon® reflectance standards. From left: 5%, 20%, 75% and 99% reflectance.

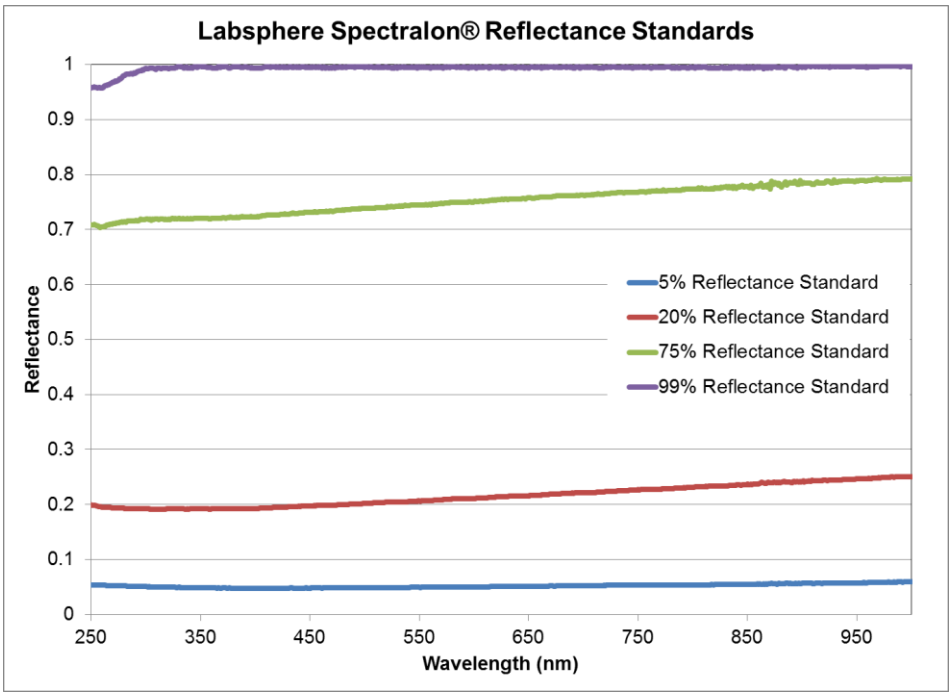


**Figure 2-5.** Reflectance spectra of Labsphere Spectralon® reflectance standards.

### 2.1.3 Detection Limits and Reproducibility

Table 2-2 presents the detection limits of the Lambda 35. The detection limits were determined by averaging six measurements of 100% (upper limit) or 0% T (lower limit) and subtracting three-times the standard deviation of the measurements from the average. Lower detection limits were determined using blocked beam measurements and upper detection limits were determined using reflection from the 99% Spectralon® reflectance standard. The upper detection limits range from 99.77 – 99.94%, with the lowest limit in the UV wavelength range. The lower detection limits range from 0.014 – 0.122%, with the highest limit in the UV range. The silicon detector has lower

photosensitivity in the UV region than in the visible and NIR regions, which translates into the difference in detection limits (i.e. higher signal to noise ratio).

Table 2-3 presents the standard deviation in measurements of blank QF and TM filter types. Reproducibility (i.e. precision) was calculated by measuring the same blank filter 10 times, rotated within the filter holder each time, and calculating the standard deviation. Similar precisions (0.66 – 0.69%) are found for QF filters irrespective of the wavelength range. Better precisions (0.45 – 0.46%) are found for TM filters with the best reproducibility (0.45%) found in the UV range. The precisions are likely better for the TM filters due to variations in surface roughness of the QF filter type.

**Table 2-2.** Lambda 35 Detection Limits

| Wavelength Range | Lower Detection Limit (%) | Upper Detection Limit (%) |
|---|---|---|
| Ultra Violet (250 – 399 nm) | 0.122 | 99.77 |
| Visible (400 – 700 nm) | 0.014 | 99.90 |
| Near Infrared (701 – 1000 nm) | 0.019 | 99.94 |

**Table 2-3.** Reproducibility of Measurements by Filter Type

| Wavelength Range | TM Standard Deviation (%) | QF Standard Deviation (%) |
|---|---|---|
| Ultra Violet (250 – 399 nm) | 0.45 | 0.69 |
| Visible (400 – 700 nm) | 0.46 | 0.69 |
| Near Infrared (701 – 1000 nm) | 0.46 | 0.66 |

### 2.1.4 Procedure for Reflectance and Transmittance Measurements

Baseline measurements must be made before any reflectance or transmittance measurements, and the baseline measurement is slightly different for each measurement so it has to be repeated before switching between measurement procedures. Photos of the procedure and set-up are shown in Figure 2-6.

For transmittance measurements, the 8° sample holder is installed at the reflectance port and the 99% Spectralon® standard is uncapped and inserted into the holder. The 0° sample holder should be installed at the transmittance port and left empty. The 100% T baseline measurement is made with this exact set-up. The 0% T baseline measurement is made by inserting a capped Spectralon® standard into the sample holder at the transmittance port in order to block the incoming light. To measure the transmittance of a filter sample, the capped Spectralon® standard is removed from the 0° sample holder at the transmittance port and the filter holder containing the filter sample is placed into the sample holder at this port, deposit-side facing away from the sphere (or towards the incident light).

Reflectance measurements require the installation of only the 8° sample holder at the reflectance port. The 100% R baseline measurement is made with the uncapped 99% Spectralon® standard inserted into the 8° sample holder. The 0% R baseline measurement is made by removing the Spectralon® standard from the 8° sample holder and leaving it empty. To make a reflectance measurement of a filter sample, the filter

holder containing the filter sample is placed into the 8° sample holder, deposit-side facing the sphere. A typical scan (reflectance or transmittance) takes approximately six

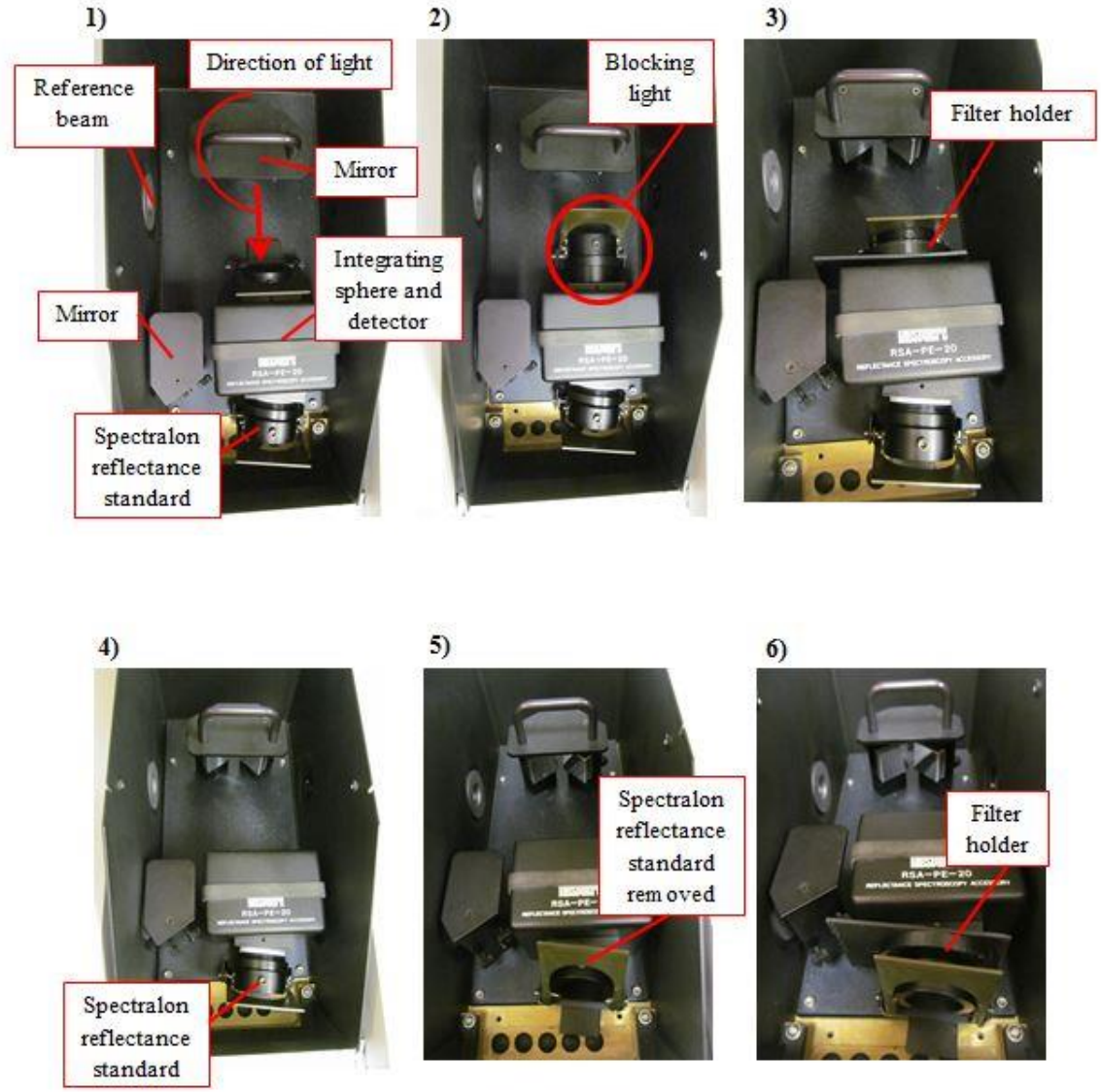


**Figure 2-6.** Procedure for reflectance and transmittance baseline calibration and sample measurement: 1) scan across wavelengths for 100% T with beam unblocked and Spectralon reflectance standard at reflectance port; 2) scan across wavelengths for 0% T with beam blocked from entering sphere; 3) insert filter at transmittance port with deposit toward beam and scan across wavelengths for transmittance measurement; 4) scan across wavelengths for 100% R with beam unblocked and Spectralon reflectance standard at reflectance port; 5) scan across wavelengths for 0% R with Spectralon standard removed; 6) insert filter at reflectance port with deposit facing beam and scan across wavelengths for reflectance measurement.

minutes and scans downward from 1000 nm to 250 nm.

## 2.2 Optical Theories as Applied to Filter Samples

### 2.2.1 Kirchoff Relationship

The general theory of operation when using the Lambda 35 spectrometer with the integrating sphere follows the Kirchoff relationship

$$R + T + A = 1 \tag{14}$$

where R is reflectance, T is transmittance and A is absorption. When making a reflectance measurement, the detector signal represents the amount of light that is not being transmitted or absorbed. When making a transmittance measurement, the detector signal represents the amount of light that is not being back-scattered or absorbed (Labsphere, 2000). However, when making these measurements on a particle-laden filter, additional multiple scattering effects are introduced by the filter medium that make the Kirchoff relationship too simplistic to be used directly with the R and T measurements provided by the Lambda 35 (i.e. a sample's R and T measured by the Lambda cannot simply be subtracted from 1 to find the sample A).

### 2.2.2 Beer-Lambert Law and Attenuation Approximation

Absorption due to aerosols has often been approximated using an attenuation coefficient ($\beta_{ATN}$) that is calculated using the Beer-Lambert Law. This law represents a linear correlation between absorption and the concentration of the absorber:

$$A = \varepsilon l c \tag{15}$$

In this equation $A$ is absorbance, ε is the molar absorptivity of the substance, $l$ is the path length or thickness, and $c$ is the concentration of the absorber. This law is also expressed as:

$$A = \ln\frac{I_0}{I} \tag{16}$$

where $I_0$ is the incident light and $I$ is the amount of light transmitted through the absorber. When applied to filter samples, $I_0$ becomes the measured light transmission through a filter before PM loading and $I$ becomes the measured light transmission through a filter after PM loading. Because this law only deals with the transmitted intensity of light, this equation essentially provides extinction or attenuation. However, this expression is a good absorption approximation for small particles ($x \ll 1$). To get $\beta_{ATN}$, the equation becomes:

$$\beta_{ATN} = \frac{a}{V}\ln\frac{I_0}{I} \tag{17}$$

where $a$ is the area of the filter deposit and V is the volume of air sampled. $\beta_{ATN}$ has the units of inverse distance, typically $Mm^{-1}$.

### 2.2.3 Two-Stream Model

A two-stream or two-layer approximation of the general radiation transfer theory has been applied to model optical measurements of particle-laden filters. Figure 2-7 depicts a two-layer model that can be used to represent PM deposits on filter media. The general form of this model comes from Kubelka and Munk (1931), has been simplified by Bohren (1987) and slightly modified by others (Gorbunov et al., 2002, Arnott et al., 2005).

This model assumes that the two layers are independent and do not change the optical properties of the other. However, PM often penetrates within the top layer of a filter and can change the filter optical properties. This can also change the way the PM

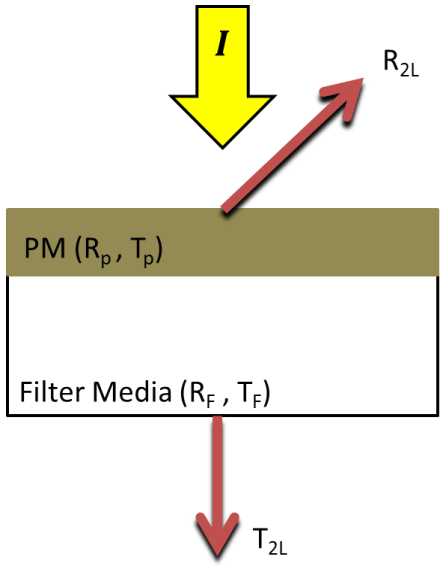


**Figure 2-7.** Two-layer model. Incident light is indicated by the letter I. The top layer is the PM deposit, denoted by the subscript P. The bottom layer is the filter media, denoted by the subscript F. The sample reflectance and transmittance measured by the Lambda 35 are of the PM and filter media together and are denoted by the subscript 2L.

behaves due to multiple scattering of light from the filter media, which essentially provides more incident light on the sample.

The R and T of an exposed filter sample measured by the Lambda 35 represent measurements of the combined reflectance of the PM and the filter media and thus gain a subscript of 2L. In order to get the measurements of just the PM on the filter, the following relationships are used (Arnott et al., 2005):

$$R_{2L} = R_P + \frac{R_F T_P^2}{1 - R_P R_F} \tag{18}$$

$$T_{2L} = \frac{T_P T_F}{1 - R_P R_F} \tag{19}$$

where $R_P$ and $T_P$ represent the reflectance and transmittance of the PM deposit and $R_F$ and $T_F$ are the reflectance and transmittance measurements of the blank filter media. Thus, to best approximate absorption of the PM layer on a filter, $R_F$ and $T_F$ measurements should be made before the filter is used for sampling. Equations 18 and 19 are solved simultaneously for $R_P$ and $T_P$. $R_P$ and $T_P$ are then used in the following equations adapted from Kubelka-Munk Theory to solve for absorption:

$$R_P = \frac{\beta\tau_s(1 - e^{-2p})}{(p - \tau_a - \beta\tau_s)e^{-2p} + (p + \tau_a + \beta\tau_s)} \tag{20}$$

$$T_P = \frac{2pe^{-p}}{(p - \tau_a - \beta\tau_s)e^{-2p} + (p + \tau_a + \beta\tau_s)} \quad (21)$$

where $\tau_a$ and $\beta\tau_s$ are the absorption optical depth and the scattering optical depth of the PM layer, respectively, and

$$p = \sqrt{\tau_a(\tau_a + 2\beta\tau_s)} \quad (22)$$

To obtain the $\beta_{abs}$ of the PM deposit, the $\tau_a$value is divided by the "depth" of the column of air sampled onto the filter:

$$\beta_{abs} = \frac{a}{V}\tau_a \quad (23)$$

For this study, both the Beer-Lambert attenuation calculation and the two-layer model were applied to QF and TM filter samples and compared. Sample attenuation and $\beta_{ATN}$ were found using Lambda 35 measurements of $T_F$ (in place of $I_o$) and $T_{2L}$ (in place of $I$) in equations 15 and 16. The $\tau_a$values of the measured filter samples were found using the Lambda 35 measurements of $R_F, T_F, R_{2L}$ and $T_{2L}$, Equations 18 - 22 and a solver function in Matlab ($fminsearch$). $\beta_{abs}$ of the PM deposit was found using Equation 23. All attenuation and absorption calculations were carried out for each wavelength in the Lambda 35 scan range (i.e. 250 – 1000 nm). The sample AAE was then calculated using: 1) the relationship in Section 1.2, Equation 10 for several wavelength pairs and 2) by

fitting the data with a power law curve approximation (i.e. $\lambda^{-AAE}$). AAEs were calculated for both the sample attenuation and absorption values and compared.

## 2.3 Methods for Characterization

### 2.3.1 Quartz-fiber and Teflon-membrane Filter Comparisons

The first step towards characterizing this light absorption measurement method was to compare measurements made on QF and TM filter media, both in situ and for later laboratory analysis. These tests characterize the reproducibility of filter measurements made by the Lambda 35 (see Section 2.1.3) as well as optical differences between filters.

The reflectance and transmittance of blank QF and TM filters were measured. Repeated measurements of a single filter, rotated within the filter holder, were made to characterize the reproducibility of a measurement. Measurements of different blank filters provided insight into differences among filters of the same type. TM filters are quite smooth and hold their shape, though the thickness of the membrane can be visually distinguishable. Some brands are rather opaque and white in color while others are more translucent and streaky. QF filters are white, very much opaque, and tend to have a rough front side and a smooth back side. The QF filter types examined were relatively similar, though the surface of each is rather rough and variable. Figure 2-8 shows blank TM and QF filters. Figure 2-9 shows the variation in reflectance and transmittance spectra among different blank TM and QF filters.

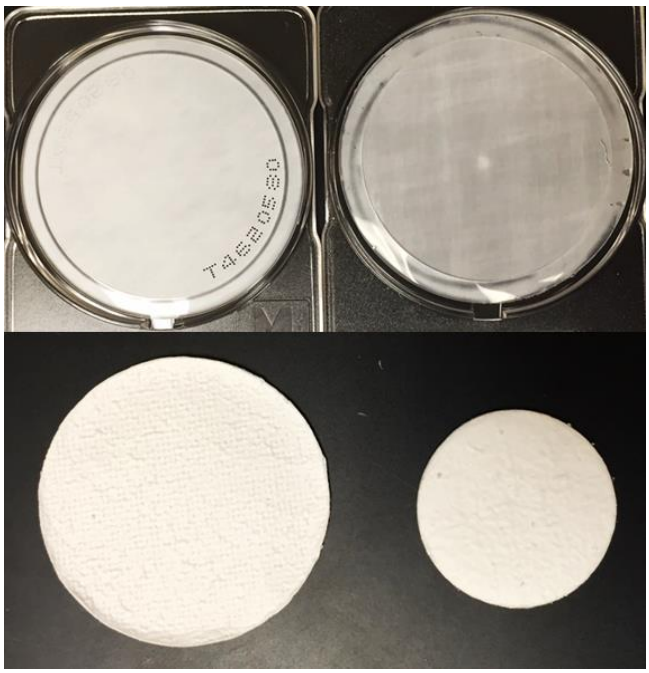

**Figure 2-8.** Blank filters. Top: Teflon-membrane (TM). Bottom: Quartz-fiber (QF). TM can vary in opacity and QF can vary in surface roughness.

Within the same batch, TM filters can vary as much as 17% in reflectance and 19% in transmittance. Across batches, these differences can increase to 41%. The measurement differences are largest (17 – 19%) in the shorter (UV) wavelengths for TM filters. The QF filters examined vary less dramatically, by maximums of only 9% (R) and 3.3% (T), though repeated measurements of the same filter can vary by up to 2.5%. The differences in QF measurements are smallest at shorter wavelengths. These differences contrast those found for single filter reproducibility measurements, where the reproducibility is best for TM measurements. The greater measurement differences between multiple TM filters is likely due to variations in membrane opacity among filters.

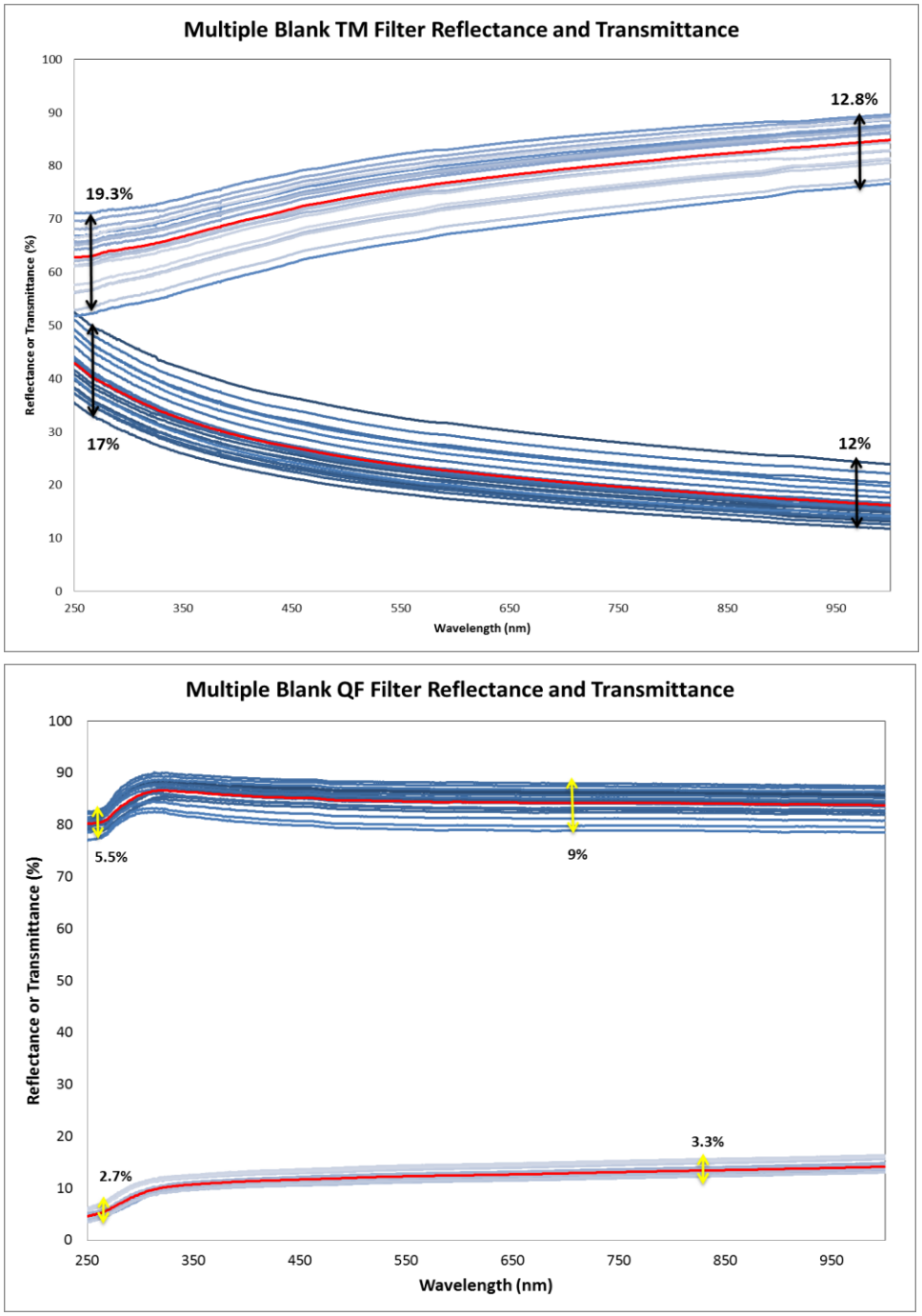


**Figure 2-9.** Reflectance and transmittance spectra of multiple blank TM (top panel) and QF (bottom panel) filters. The lighter colored groups of curves in each panel are the transmittance measurements while the darker colored groups are the reflectance measurements. The average value for each group of measurements is shown in red. TM filter measurements vary the most at shorter wavelengths (17 – 19%) while QF filter measurements vary more at longer wavelengths (3.3 – 9%). Within the same batch, TM measurements can vary up to 19.3% (UV reflectance) and QF measurements can vary up to 9% (Vis-NIR reflectance).

### 2.3.2 Source Filters

In order to use the Lambda 35 as a method to delineate contributions from separate sources, reflectance and transmittance measurements were made of laboratory-generated emissions collected onto TM and QF filters. The source samples used were previously generated from other studies and were chosen from the filter archive of the Desert Research Institute's (DRI) Environmental Analysis Facility (EAF). Sources include diesel, wood burning, flaming and smoldering phases of biomass combustion, and various resuspended dust. Attenuation, $\beta_{ATN}$, $\beta_{abs}$ and AAE values were calculated for these samples using Equations 15 - 22. Some of these laboratory-generated source aerosols were simultaneously sampled by a collocated three-wavelength photoacoustic spectrometer (PAS), so the $\beta_{abs}$ and AAEs of the filter samples were calculated and compared with those measured by the PAS. Details of these source filters are listed in Table 2-4. Figure 2-10 and Figure 2-11 show photos of the source samples listed in Table 2-4.

**Table 2-4.** Source Sample Information

| Filter ID | Source Type | Filter Medium | PM Size [a] | Deposit Mass (µg/m$^3$) [b] | Other Analyses Performed [c] |
|---|---|---|---|---|---|
| BIOTK072 | Bitterbrush Stems | TM | TSP | 1229.41 | MSG, NHC, SOI, ANI, N4C, NAA, KPA, OET, ELX |
| BIOTK086 | Carpet Leaves (50% wet) | TM | TSP | 7238.94 | |
| BIOTK088 | Duff Composite (100% wet) | TM | TSP | 3262.18 | |
| BIOTK102 | Litter Composite (100% wet) | TM | TSP | 5008.49 | |
| REST339 | Paved Parking Lot Dust | TM | 10 | 29046.05 | MSG, ANI, N4C, KPA, OET, ELX |
| REST1856 | Paved Road Dust | TM | 10 | 34690.66 | MSG, ELX |
| REST2015 | Pellet Dust (Taconite) | TM | 2.5 | 55503.77 | MSG, ANI, N4CF, NAAF, MGA, KPA, CAA, OET, ELX |
| REST2102 | Deicing Material | TM | 2.5 | 73546.51 | MSG, ATT, ANI, CAI, OET, ELX |
| REST2183/Q2193 | Red-colored Soil | TM & QF | 2.5 | 7.50 | MSG |
| REST2184/Q2194 | Red-colored Soil | TM & QF | 10 | 22.12 | |
| REST2185/Q2195 | Red-colored Soil | TM & QF | 2.5 | 10.39 | |
| REST2186/Q2196 | Red-colored Soil | TM & QF | 10 | 36.16 | |
| STRST052 | Diesel | TM | 2.5 | 206.10 | MSG, BBD, ANI, CAI, MGA, CAA, OET, ELX |
| STRST061 | Diesel | TM | 2.5 | 314.88 | |
| STRST064 | Diesel | TM | 2.5 | 433.05 | |
| STRST103 | Acetylene Flame | TM | 2.5 | 686.96 | |
| STRST104 | Acetylene Flame | TM | 2.5 | 279.23 | |
| STRST111 | Acetylene Flame | TM | 2.5 | 343.01 | |
| STRST123 | Wood Smoke | TM | 2.5 | 505.00 | |
| STRST133 | Wood Smoke | TM | 2.5 | 279.80 | |
| STRST136 | Wood Smoke | TM | 2.5 | 119.19 | |
| NCAQ094 | Diesel | QF | 2.5 | Lightest | OET, FGI |
| NCAQ088 | Diesel | QF | 2.5 | | |
| NCAQ090 | Diesel | QF | 2.5 | | |
| NCAQ089 | Diesel | QF | 2.5 | | |
| NCAQ091 | Diesel | QF | 2.5 | | |
| NCAQ092 | Diesel | QF | 2.5 | | |
| NCAQ093 | Diesel | QF | 2.5 | | |
| NCAQ095 | Diesel | QF | 2.5 | Heaviest | |
| NCAQ072 | Smoldering Peat | QF | 2.5 | Lightest | |
| NCAQ073 | Smoldering Peat | QF | 2.5 | | |
| NCAQ075 | Smoldering Peat | QF | 2.5 | | |
| NCAQ074 | Smoldering Peat | QF | 2.5 | | |
| NCAQ042 | Smoldering Peat | QF | 2.5 | | |
| NCAQ077 | Smoldering Peat | QF | 2.5 | | |
| NCAQ078 | Smoldering Peat | QF | 2.5 | | |
| NCAQ079 | Smoldering Peat | QF | 2.5 | Heaviest | |
| NCAQ080 | Pine Needles | QF | 2.5 | Lightest | |
| NCAQ081 | Pine Needles | QF | 2.5 | | |
| NCAQ082 | Pine Needles | QF | 2.5 | | |

| | | | | | |
|---|---|---|---|---|---|
| NCAQ083 | Pine Needles | QF | 2.5 | | |
| NCAQ084 | Pine Needles | QF | 2.5 | | |
| NCAQ085 | Pine Needles | QF | 2.5 | | |
| NCAQ086 | Pine Needles | QF | 2.5 | Heaviest | |
| NCAQ087 | Pine Needles | QF | 2.5 | | |
| NCAQ045 | Pine Cone | QF | 2.5 | Lightest | |
| NCAQ048 | Pine Cone | QF | 2.5 | | |
| NCAQ047 | Pine Cone | QF | 2.5 | | |
| NCAQ049 | Pine Cone | QF | 2.5 | | |
| NCAQ051 | Pine Cone | QF | 2.5 | | |
| NCAQ046 | Pine Cone | QF | 2.5 | | |
| NCAQ052 | Pine Cone | QF | 2.5 | | |
| NCAQ053 | Pine Cone | QF | 2.5 | Heaviest | |
| DBIT001/Q1001 | Ponderosa Pine Needles | TM & QF | TSP | 10328.70 | |
| DBIT002/Q1002 | Ponderosa Pine Needles | TM & QF | TSP | 13617.92 | |
| DBIT003/Q1003 | Ponderosa Pine Needles | TM & QF | TSP | 4972.09 | |
| DBIT005/Q1005 | Cheat Grass | TM & QF | TSP | 4172.04 | |
| DBIT006/Q1006 | Cheat Grass | TM & QF | TSP | 15330.26 | |
| DBIT007/Q1007 | Cheat Grass | TM & QF | TSP | 8346.43 | |
| DBIT008/Q1008 | Speat25,rep1 | TM & QF | TSP | 2193.89 | |
| DBIT009/Q1009 | Speat25,rep2 | TM & QF | TSP | 456.38 | MSG, OET |
| DBIT010/Q1010 | Speat25,rep3 | TM & QF | TSP | 385.62 | |
| DBIT011/Q1011 | Speat50,rep1 | TM & QF | TSP | 1975.68 | |
| DBIT012/Q1012 | Speat50,rep2 | TM & QF | TSP | 1675.82 | |
| DBIT013/Q1013 | Speat50,rep3 | TM & QF | TSP | 762.45 | |
| DBIT014/Q1014 | Apeat25,rep1 | TM & QF | TSP | 391.39 | |
| DBIT015/Q1015 | Apeat25,rep2 | TM & QF | TSP | 1139.38 | |
| DBIT016/Q1016 | Apeat25,rep3 | TM & QF | TSP | 769.12 | |

[a] TSP: Total suspended particles, usually in range of ≤ 30 – 50 μm.

[b] Masses are not known for several QF source samples so samples are listed in table in order of lightest to heaviest visual loading.

[c] Other analyses descriptions. ANI: anion analysis; ATT: transmissometer attenuation analysis; BBD: densitometer analysis; CAA: soluble calcium analysis; CAI: cation analysis; ELX: x-ray fluorescence analysis; FGI: FTIR analysis; KPA: soluble potassium analysis; MGA: soluble magnesium analysis; MSG: gravimetric analysis (filter mass); N4C: ammonium analysis; NAA: soluble sodium analysis; NHC: $NH^+$ analysis; SOI: $SO_2$ analysis.


**Figure 2-10.** Photos of source filter samples analyzed for this study. Source type is listed above the filter samples. Of the samples in this image , only the red soil have QF and TM filter pairs (QF pictured). All others are either TM or QF only.

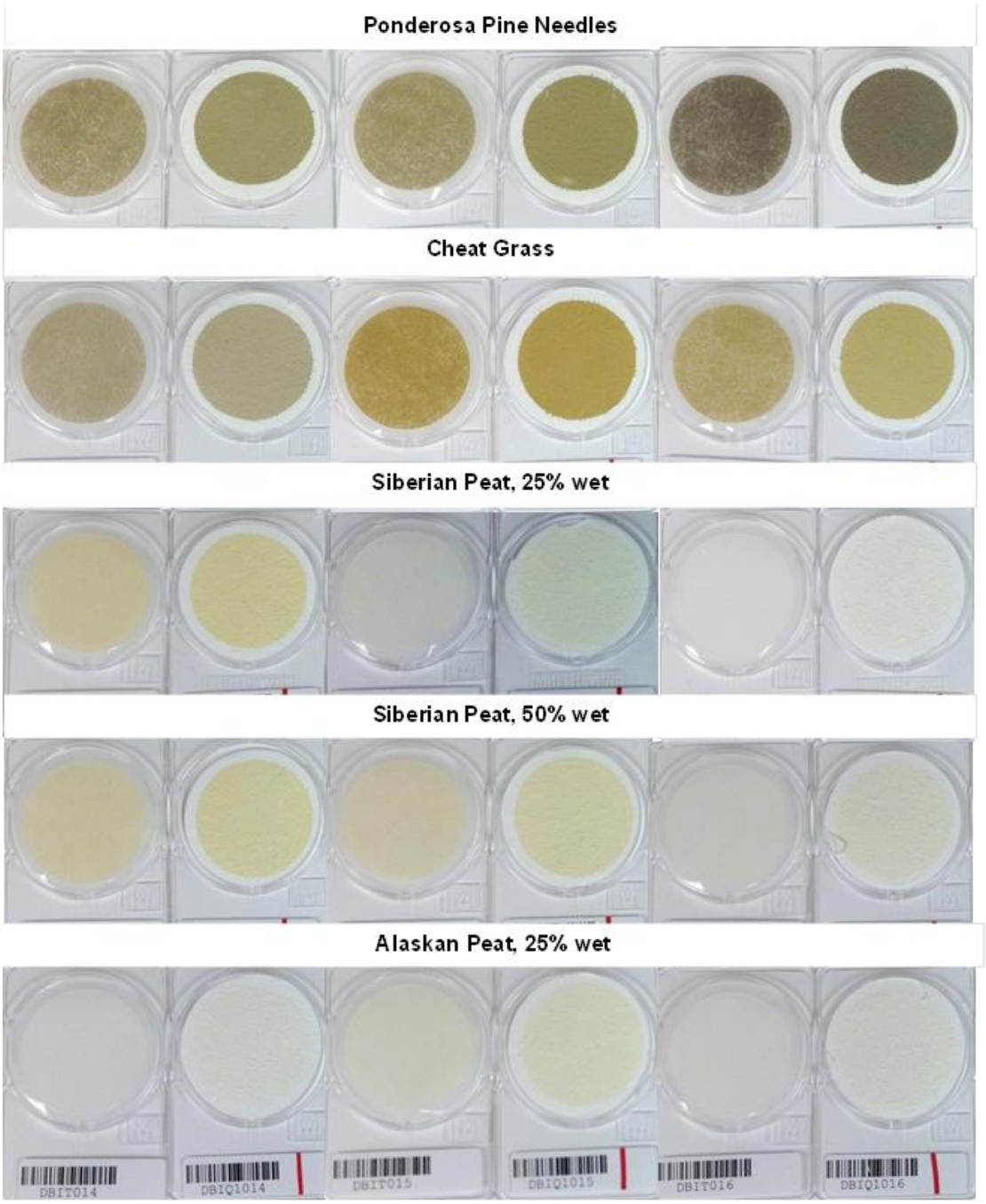


**Figure 2-11.** Photos of smoldering and flaming biomass burning samples analyzed in this study (filter ID DBIT and DBIQ). Source type is listed above the filter photos. TM and QF sample pairs are placed side by side.

### 2.3.3 Layered Source Filters

As an intermediate step between single source filters and ambient samples, several filter samples were created with known amounts of both diesel exhaust and biomass burning emissions. These filters were created with the intention of examining the absorption effects of various ratios of BC to BrC as well as to examine layering effects (as the sources had to be layered in order to establish known source amounts on the filters,).

Diesel-engine exhaust and biomass (cheat grass) combustion emissions were sampled onto pairs of QF and TM filters using a manifold equipped with a $PM_{2.5}$ cyclone. The manifold set-up is depicted in Figure 2-12. Diesel-engine exhaust was sampled from the exhaust pipe of a Cummins Onon 12500 Quiet Diesel generator (Columbus, IN). Dry cheat grass was burned, in both flaming and smoldering phases, in an outdoor stove as depicted in Figure 2-12. For each set of filters, the first source layer was sampled then the filter was weighed in order to determine how much of the second source was needed to achieve the desired ratio. A simple ratio of sample time to sample mass was used to calculate the sampling time for the second layer.

Two sets of eight QF and TM filter pairs (16 pairs, 32 filters total) were created with the intent of achieving the following mass ratios of sources: 50/50, 70/30, 30/70, and 90/10 with alternated layers of diesel and biomass. Specific details of the sampling are listed in Table 2-5. Photos of these filters are shown in Figure 2-13.

As shown in Table 2-5, the two samples MJ010 and MJ014 represent two separate runs using diesel as the bottom layer with the intent of achieving 70/30 diesel to biomass ratio. The samples had actual mass ratios of 77/23 and 79/21, respectively. The second sets of filter pairs were created in order to achieve lighter sample loadings.

**Figure 2-12.** Layered source sampling set up. At left, a photo of the manifold set up for use in collecting the layered samples. Also shown in this photo are the diesel generator used for exhaust sampling and the outdoor stove used to burn cheat grass. At right, a photo of cheat grass in stove before being burned.

**Table 2-5.** Layered Source Filter Sampling Details

| Filter ID (QF & TM) | Desired Mass Ratio[a] | Mass of Diesel (mg) | Mass of Biomass (mg) | Actual Mass Ratio | Flow Rates (L/min)[b] | | Sampling Times |
|---|---|---|---|---|---|---|---|
| MJ002 | 90/10 B to D | 0.058 | 2.026 | 97/3 B to D | BT: 21.8 BQ: 21.1 | DT: 20.9 DQ: 20.7 | B: 50 sec D: 56 sec |
| MJ006 | 90/10 D to B | 2.463 | 0.134 | 95/5 D to B | BT: 21.1 BQ: 21.4 | DT: 20.2 DQ: 21.4 | B: 30 sec D: 10.7 min |
| MJ015[c] | 90/10 D to B | 0.646 | 0.096 | 87/13 D to B | BT: 21.4 BQ: 21.4 | DT: 21.4 DQ: 21.4 | B: 30 sec D: 2.83 min |
| MJ018[c] | 90/10 B to D | 0.106 | 1.248 | 92/8 B to D | BT: 21.4 BQ: 21.4 | DT: 21.4 DQ: 21.4 | B: 45 sec D: 45 sec |
| MJ004 | 50/50 B to D | 0.661 | 0.647 | 50/50 B to D | BT: 21.8 BQ: 21.1 | DT: 20.9 DQ: 20.7 | B: 70 sec D: 2.78 min |
| MJ009 | 50/50 D to B | 1.480 | 1.632 | 48/52 D to B | BT: 20.9 BQ: 21.4 | DT: 20.7 DQ: 21.4 | B: 90 sec D: 5.9 min |
| MJ013[c] | 50/50 D to B | 0.284 | 0.350 | 45/55 D to B | BT: 21.4 BQ: 21.4 | DT: 21.4 DQ: 21.4 | B: 30 sec D: 90 sec |
| MJ016[c] | 50/50 B to D | 0.630 | 0.443 | 41/59 B to D | BT: 21.4 BQ: 21.4 | DT: 21.4 DQ: 21.4 | B: 60 sec D: 2.33 min |
| MJ003 | 30/70 B to D | 0.915 | 0.372 | 29/71 B to D | BT: 21.8 BQ: 21.1 | DT: 20.9 DQ: 20.7 | B: 30 sec D: 3.7 min |
| MJ005 | 70/30 B to D | 0.478 | 1.090 | 70/30 B to D | BT: 21.8 BQ: 21.1 | DT: 20.9 DQ: 20.7 | B: 90 sec D: 2 min |
| MJ008 | 30/70 D to B | 0.701 | 1.908 | 27/73 D to B | BT: 20.9 BQ: 21.4 | DT: 20.7 DQ: 21.4 | B: 90 sec D: 3.5 min |
| MJ010 | 70/30 D to B | 2.286 | 0.696 | 77/23 D to B | BT: 20.9 BQ: 21.4 | DT: 20.7 DQ: 21.4 | B: 60 sec D: 8.3 min |
| MJ012[c] | 30/70 D to B | 0.178 | 0.345 | 34/66 D to B | BT: 21.4 BQ: 21.4 | DT: 21.4 DQ: 21.4 | B: 60 sec D: 58 sec |
| MJ014[c] | 70/30 D to B | 0.489 | 0.127 | 79/21 D to B | BT: 21.4 BQ: 21.4 | DT: 21.4 DQ: 21.4 | B: 30 sec D: 2.25 min |
| MJ017[c] | 30/70 B to D | 0.448 | 0.203 | 31/69 B to D | BT: 21.4 BQ: 21.4 | DT: 21.4 DQ: 21.4 | B: 30 sec D: 2.5 min |
| MJ019[c] | 70/30 B to D | 0.461 | 0.966 | 68/32 B to D | BT: 21.4 BQ: 21.4 | DT: 21.4 DQ: 21.4 | B: 90 sec D: 2.17 min |

[a] First source listed is the bottom layer. B stands for Biomass (cheat grass) and D stands for Diesel. Ratios given in percent of total mass.

[b] BQ and BT denote flow rates for biomass sampling on quartz-fiber and Teflon-membrane filters, respectively. Similarly, DQ and DT denote flow rates for diesel sampling on quartz-fiber and Teflon-membrane filters, respectively.

[c] Samples MJ012-019 are the second set of eight filter pairs. These were sampled separately from MJ002-010 and were created to have lighter loadings.

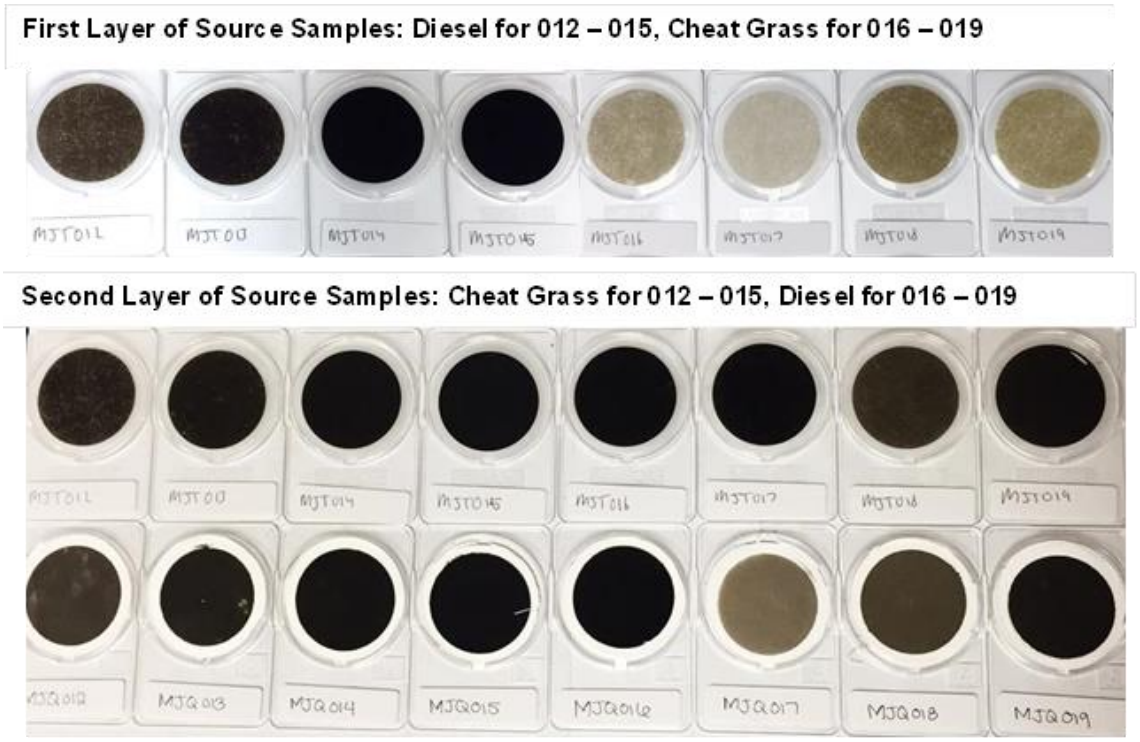


**Figure 2-13.** Photos of layered source samples. Top row: bottom layer of TM filter samples MJT012 – 019 (diesel-exhaust for 012 – 015 and cheat grass emissions for 016-019). Second and third row: TM and QF layered samples (012 – 019) after collection of top layer. TM samples are in second row and QF samples are in third row, directly below their TM counterpart.

### 2.3.4 Ambient Samples

A total of 31 ambient samples were chosen from 1) the Texas Commission on Environmental Quality (TCEQ) PM2.5 air monitoring network, 2) the Port of Los Angeles (LA), and 3) 2013 Rim Fire and American Fire influence on Reno, NV. All samples are listed in Table 2-6.

The TCEQ samples were collected from the Clinton St. site in Houston, TX. A map indicating the location of the sampling site is shown in Figure 2-14 This site is in an urban location with likely source contributions from fossil fuel combustion. Several samples were chosen due to the likely presence of African dust transported from the Sahara. Photos of the filter samples are shown in Figure 2-15.

The Port of LA samples were collected at the Terminal Island Treatment Plant (TITP) site, in the center of port operations. A map of this site is shown in Figure 2-16. At this site, the likely source contributions are from ship crude oil emissions and diesel-engine emissions, so large contributions from BC are expected. Photos of the filter samples are shown in Figure 2-17.

Samples during the 2013 Rim and American Fires took place on the rooftop of the DRI Northern Nevada Science Center Building in Reno, NV in August of 2013. The Rim Fire was burning in and around Yosemite National Park in California, approximately 120 miles south of the sampling location. The American Fire was burning in Placer County, CA, west of Lake Tahoe and approximately 50 miles west of the

sampling location. The Rim Fire burned approximately 257,314 acres over the course of 68 days, and the American fire burned approximately 27,440 acres over the course of 20 days. Smoke from both fires was advected into the Reno/Tahoe basin and as far north as Idaho. Contributions from both BrC and BC are expected in these samples. Photos of the filter samples are shown in Figure 2-18.

**Table 2-6.** Ambient Sample Information

| Filter ID | Ambient Sample Location | Filter Medium | PM Size | Deposit Mass ($\mu g/m^3$) | Other Analyses Performed [a] |
|---|---|---|---|---|---|
| SLAFT/Q6759 | Port of LA, CA | TM & QF | 2.5 | 10.05 | |
| SLAFT/Q6804 | Port of LA, CA | TM & QF | 2.5 | 7.44 | |
| SLAFT/Q6808 | Port of LA, CA | TM & QF | 2.5 | 9.46 | MSG, OET |
| SLAFT/Q6824 | Port of LA, CA | TM & QF | 2.5 | 11.79 | |
| Port of LA, CA | Port of LA, CA | TM & QF | 2.5 | 7.78 | |
| TC135T/Q14015 | Clinton St., Houston, TX | TM & QF | 2.5 | 14.96 | |
| TC135T/Q14016 | Clinton St., Houston, TX | TM & QF | 2.5 | 18.75 | |
| TC135T/Q14050 | Clinton St., Houston, TX | TM & QF | 2.5 | 17.17 | |
| TC135T/Q14053 | Clinton St., Houston, TX | TM & QF | 2.5 | 12.37 | |
| TC135T/Q14055 | Clinton St., Houston, TX | TM & QF | 2.5 | 13.20 | |
| TC135T/Q14056 | Clinton St., Houston, TX | TM & QF | 2.5 | 13.46 | |
| TC135T/Q14074 | Clinton St., Houston, TX | TM & QF | 2.5 | 11.75 | MSG, OET |
| TC135T/Q14102 | Clinton St., Houston, TX | TM & QF | 2.5 | 28.63 | |
| TC135T/Q14108 | Clinton St., Houston, TX | TM & QF | 2.5 | 19.29 | |
| TC135T/Q14109 | Clinton St., Houston, TX | TM & QF | 2.5 | 32.58 | |
| TC135T/Q14111 | Clinton St., Houston, TX | TM & QF | 2.5 | 26.04 | |
| TC135T/Q14112 | Clinton St., Houston, TX | TM & QF | 2.5 | 14.04 | |
| TC135T/Q14113 | Clinton St., Houston, TX | TM & QF | 2.5 | 9.08 | |
| SDKT083/Q0459 | Rim Fire, Reno, NV | TM & QF | 2.5 | 36.41 | |
| SDKT085/Q0464 | Rim Fire, Reno, NV | TM & QF | 2.5 | 12.93 | |
| SDKT082/Q0469 | Rim Fire, Reno, NV | TM & QF | 2.5 | 26.02 | |
| SDTK084/Q0474 | Rim Fire, Reno, NV | TM & QF | 2.5 | 36.24 | |
| SDKT086/Q0479 | Rim Fire, Reno, NV | TM & QF | 2.5 | 16.77 | |
| SDKT087/Q0484 | Rim Fire, Reno, NV | TM & QF | 2.5 | 35.40 | |
| SDKT088/Q0489 | Rim Fire, Reno, NV | TM & QF | 2.5 | 5.24 | MSG, OET |
| SDKT090/Q0494 | Rim Fire, Reno, NV | TM & QF | 2.5 | 5.26 | |
| SDKT089/Q0499 | Rim Fire, Reno, NV | TM & QF | 2.5 | 4.37 | |
| SDKT091/Q0505 | Rim Fire, Reno, NV | TM & QF | 2.5 | 6.26 | |
| SDKT092/Q0510 | Rim Fire, Reno, NV | TM & QF | 2.5 | 7.35 | |
| SDKT093/Q0515 | Rim Fire, Reno, NV | TM & QF | 2.5 | 6.82 | |
| SDKT094/Q0520 | Rim Fire, Reno, NV | TM & QF | 2.5 | 5.43 | |

[a] Other analysis descriptions. MSG: gravimetric analysis (filter mass); OET: thermal-optical carbon analysis.

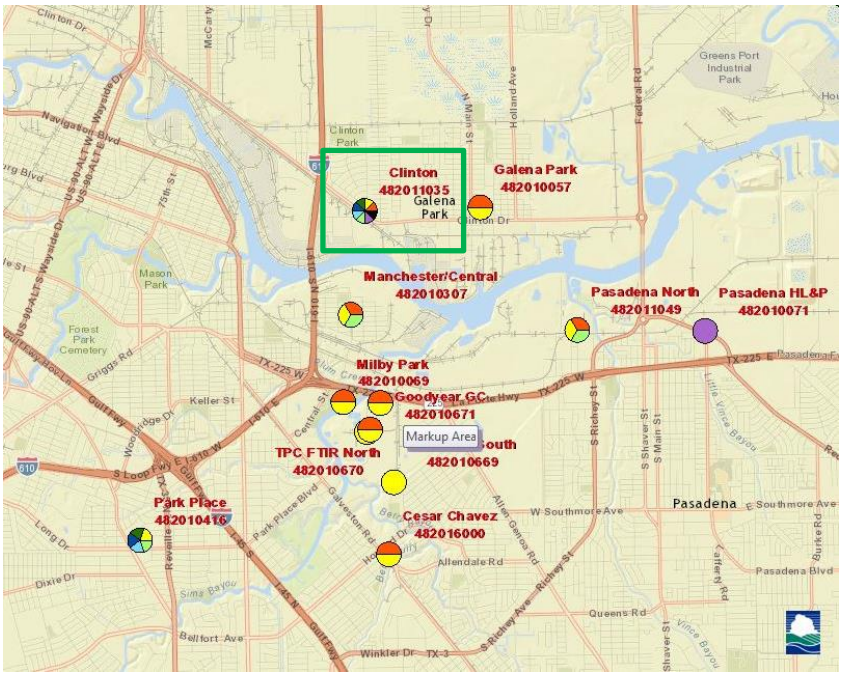


**Figure 2-14.** Map of Houston, TX, highlighting the TCEQ Clinton St. monitoring site (outlined by green box).

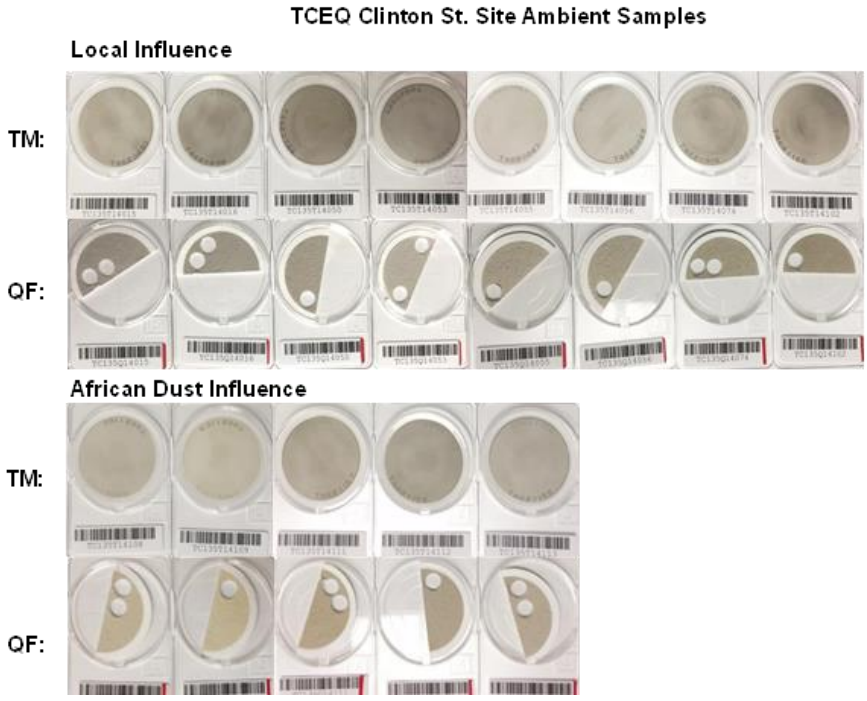


**Figure 2-15.** Photos of TM and QF filter samples from the TCEQ Clinton St. Site. The top two rows are samples from local influence and the bottom two rows are samples from a time of African dust transport. TM samples are above their QF counterparts. 0.5 $cm^2$ punches were removed previously from QF filters for carbon analysis.

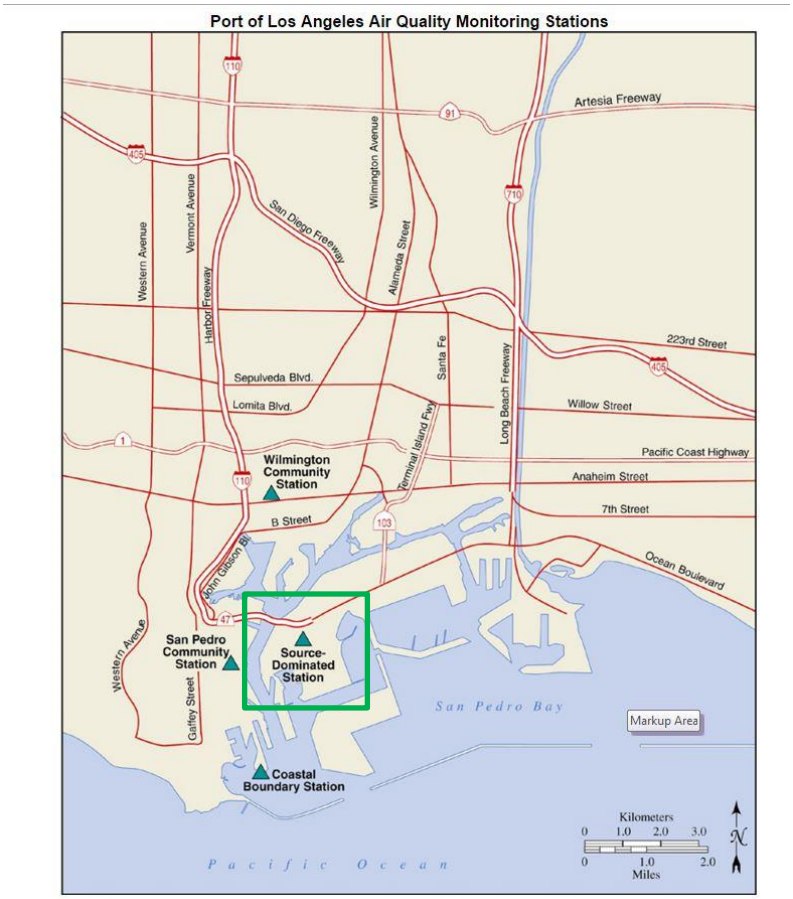


**Figure 2-16.** Map of the Port of LA air quality monitoring stations. The samples examined in this study come from the TITP site, indicated by the green box.

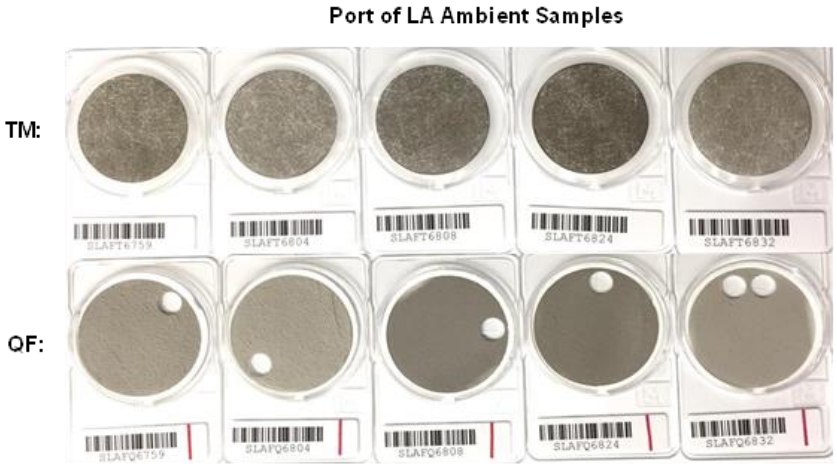


**Figure 2-17.** Photos of TM and QF filter samples from the Port of LA TITP site. TM samples are above their QF counterparts. 0.5 $cm^2$ punches were removed previously from QF filters for carbon analysis.


**Figure 2-16.** Photos of TM and QF filter samples collected in Reno, NV, during smoke transport from the Rim Fire. TM samples are shown above their QF counterparts. 0.5 $cm^2$ punches were removed previously from QF filters for carbon analysis.

# 3. Results and Discussion

Section 3.1 covers the reflectance and transmittance measurements of the filter samples. Section 3.2 examines the attenuation and absorption calculations of the filter samples. Section 3.3 presents the AAEs calculated for the filter samples and Section 3.4 inspects the inherent discrepancies in extrapolation methods of absorption measurements with regards to radiative forcing.

## 3.1 Reflectance and Transmittance Measurements

### 3.1.1 Source Samples

Reflectance and transmittance measurements of five source-specific filter samples, including smoldering and flaming biomass, paved road dust, taconite dust, and diesel exhaust, are shown in Figure 3-1. The spectra are normalized by each sample's average reflectance or transmittance value over the wavelength range of 250 – 1000 nm. Through this juxtaposition, the varied wavelength dependences of the different source samples are evident.

Figures 3-2 and 3-3 show variations of reflectance and transmittance spectra for biomass burning samples (QF and TM), respectively. These samples show a flat reflectance response in the NIR wavelengths (800 – 1000 nm) with a sharp drop beginning in the visible range (~550 nm) into the UV. A moderate peak within the visible range is observed for the TM samples with the highest reflectance in the NIR range for QF samples. The response is similar for transmittance of QF biomass samples, though a

gentler drop is observed for TM samples from 950 to 450 nm. Both the reflectance and transmittance curves can be approximated using a polynomial curve fit of a high order ($5^{th}$ or $6^{th}$). Samples with a very low (e.g. 0.01) EC/TC ratio have the most prominent reflectance peaks and sharpest decreases in response into the visible and UV ranges.

The flaming wood burning samples (shown in Figures 3-2 and 3-3 in green) are more BC dominated than many of the other biomass samples due to the flaming nature of the burn, thus the transmittance responses drop off more linearly in the NIR and visible range than those for smoldering biomass burning. The reflectance spectra for these flaming phase samples are generally more flat; though, depending on the BC and BrC composition, the spectra may resemble that of smoldering biomass burning. The reflectance curves are well approximated by a $6^{th}$ order polynomial while the transmittance curves are well represented by a $3^{rd}$ order polynomial.

Reflectance and transmittance spectra for various dust samples are shown in Figure 3-4. Dust samples show a minor reflectance peak in the visible range and a decreasing trend into the UV, though the decline is not as sharp as that for biomass samples. The transmittance response for dust tends to decrease with decreasing wavelength. The dust sample reflectance curve-fits range from $4^{th}$ to $6^{th}$ order polynomials while the transmittance curve-fits range from $3^{rd}$ to $6^{th}$ order, though the more colorful dust spectra (e.g. red soil and Taconite) are not well represented by a curve-fit.

The reflectance and transmittance response of diesel samples (Figure 3-5) are both relatively flat across the measured wavelength range, though the responses do slowly decrease with decreasing wavelength. Samples that are more heavily loaded tend to be the most spectrally flat and have the lowest reflectance and transmittance response. The reflectance and transmittance spectra can be fit well with 3$^{rd}$ and 2$^{nd}$ order polynomials and, for more heavily loaded samples, sometimes a purely linear fit.

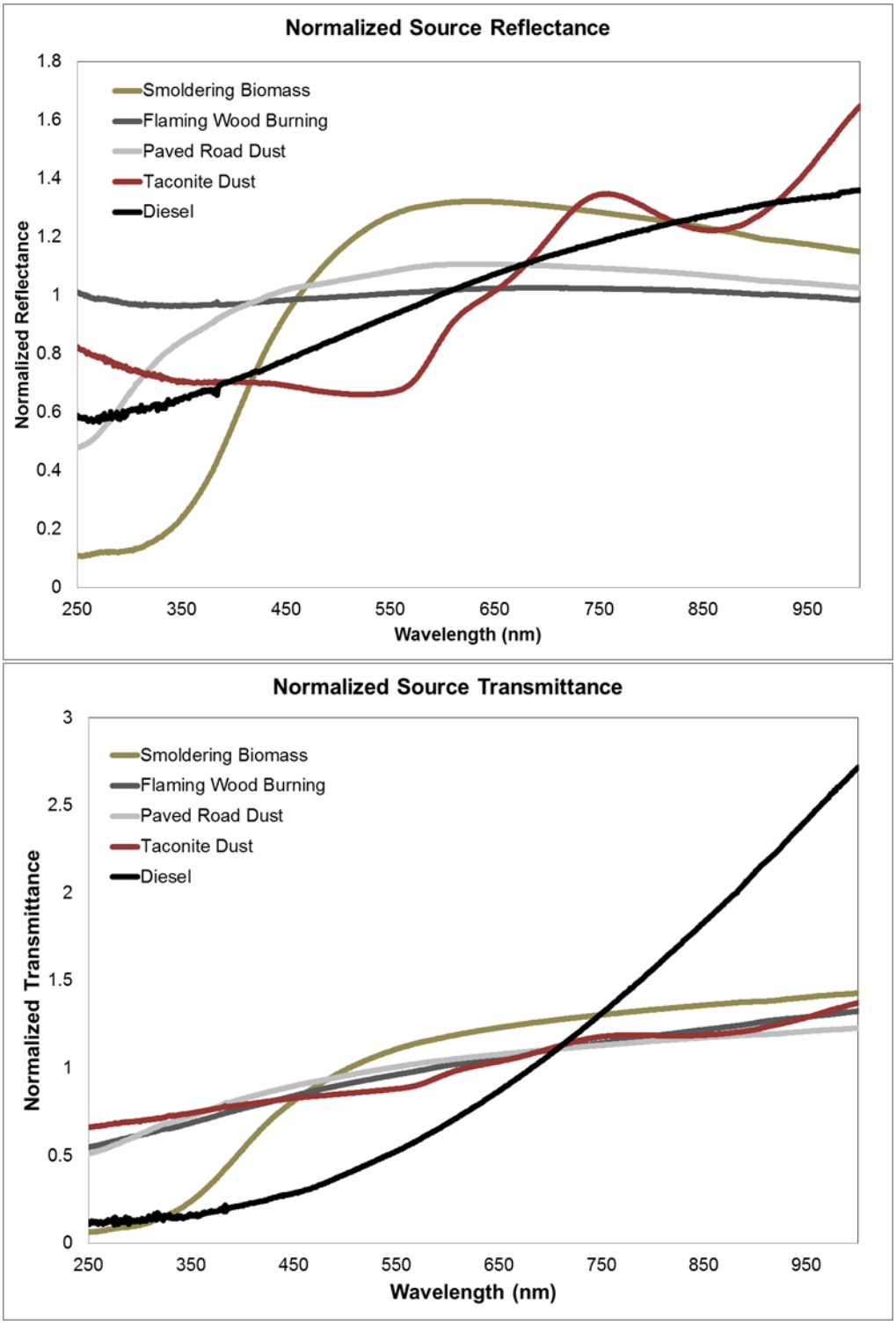


**Figure 3-1.** Reflectance (top) and transmittance (bottom) spectra of various source samples, normalized to the average sample reflectance or transmittance. When plotted in this way, the differences between source types are clearly evident.

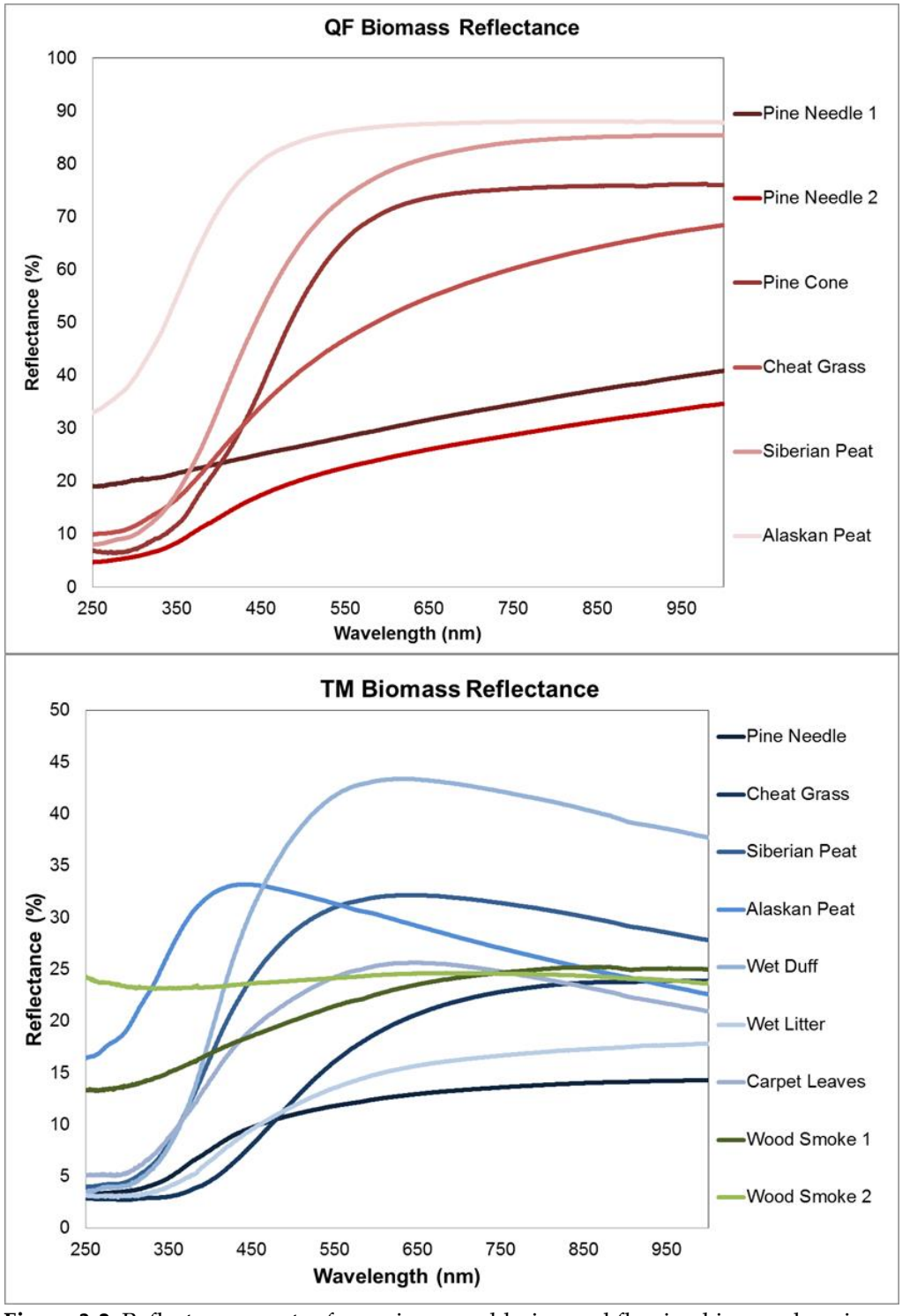


**Figure 3-2.** Reflectance spectra for various smoldering and flaming biomass burning samples. QF spectra are shown in the top plot in red while TM spectra are shown in blue in the bottom plot. Not all samples are part of a QF and TM pair so source types differ. Flaming wood burning samples are highlighted in the bottom plot in green.

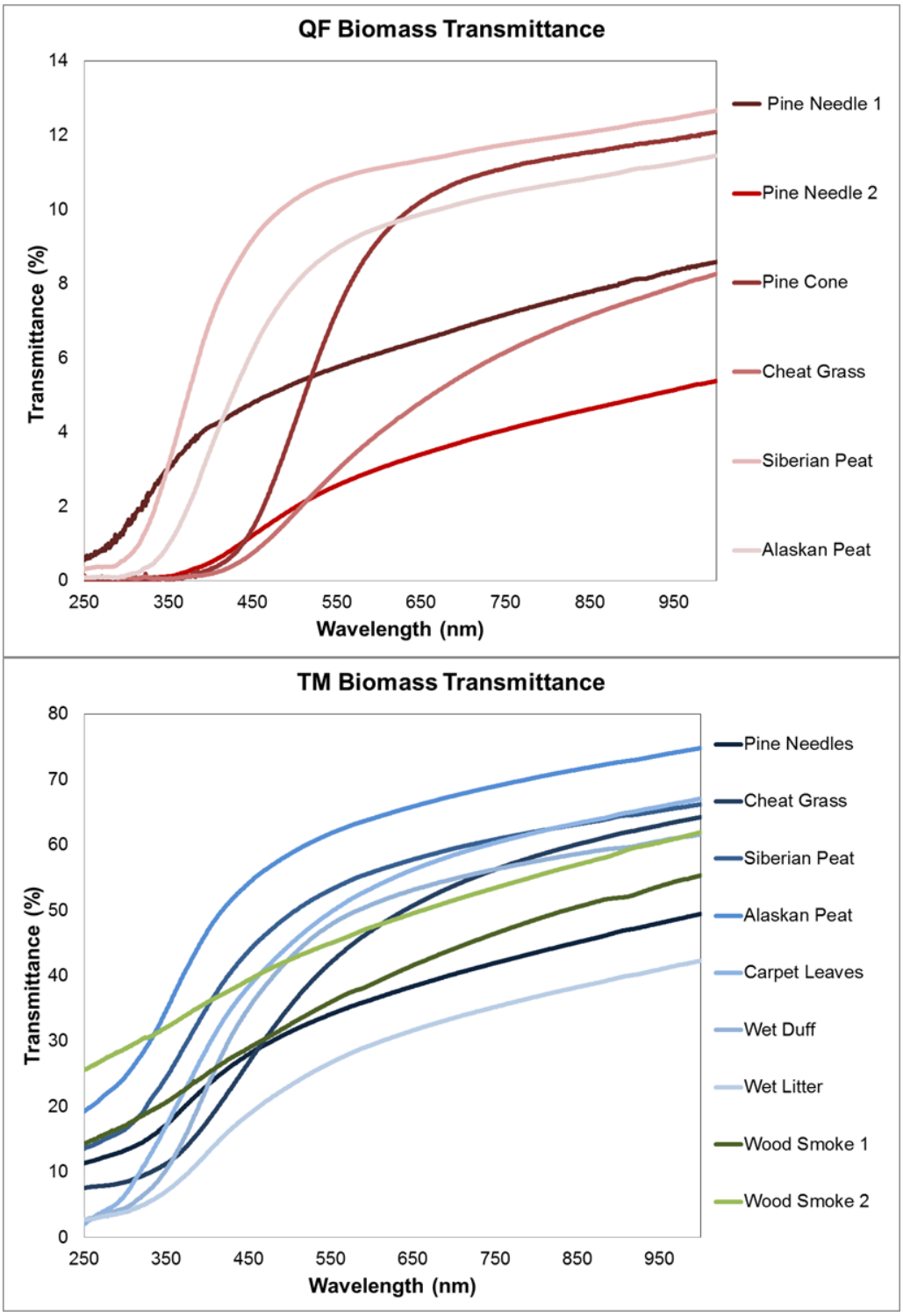


**Figure 3-3.** Transmittance spectra for various smoldering and flaming biomass burning samples (same set of samples shown in Figure 3-2). QF spectra are shown in the top plot in red while TM spectra are shown in blue in the bottom plot. Not all samples are part of a QF and TM pair so source types differ between plots. Flaming wood burning samples are highlighted in the bottom plot in green.

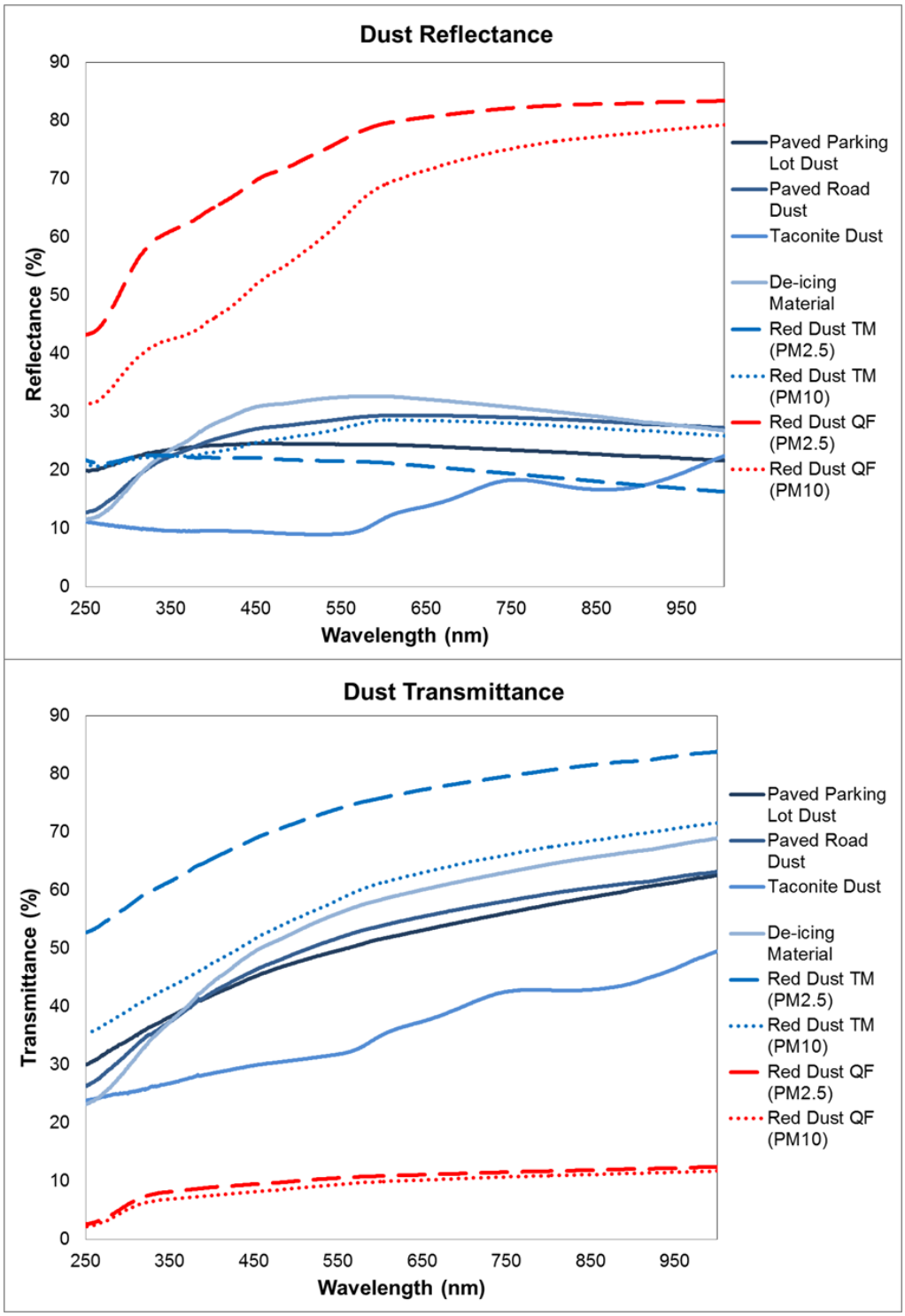


**Figure 3-4.** Reflectance (top) and transmittance (bottom) spectra for QF (red) and TM (blue) dust samples. The only samples with QF and TM filter pairs are those of resuspended red soil. The $PM_{2.5}$ QF & TM pair spectra are indicated by dashed lines and the $PM_{10}$ pair are indicated by dotted lines.

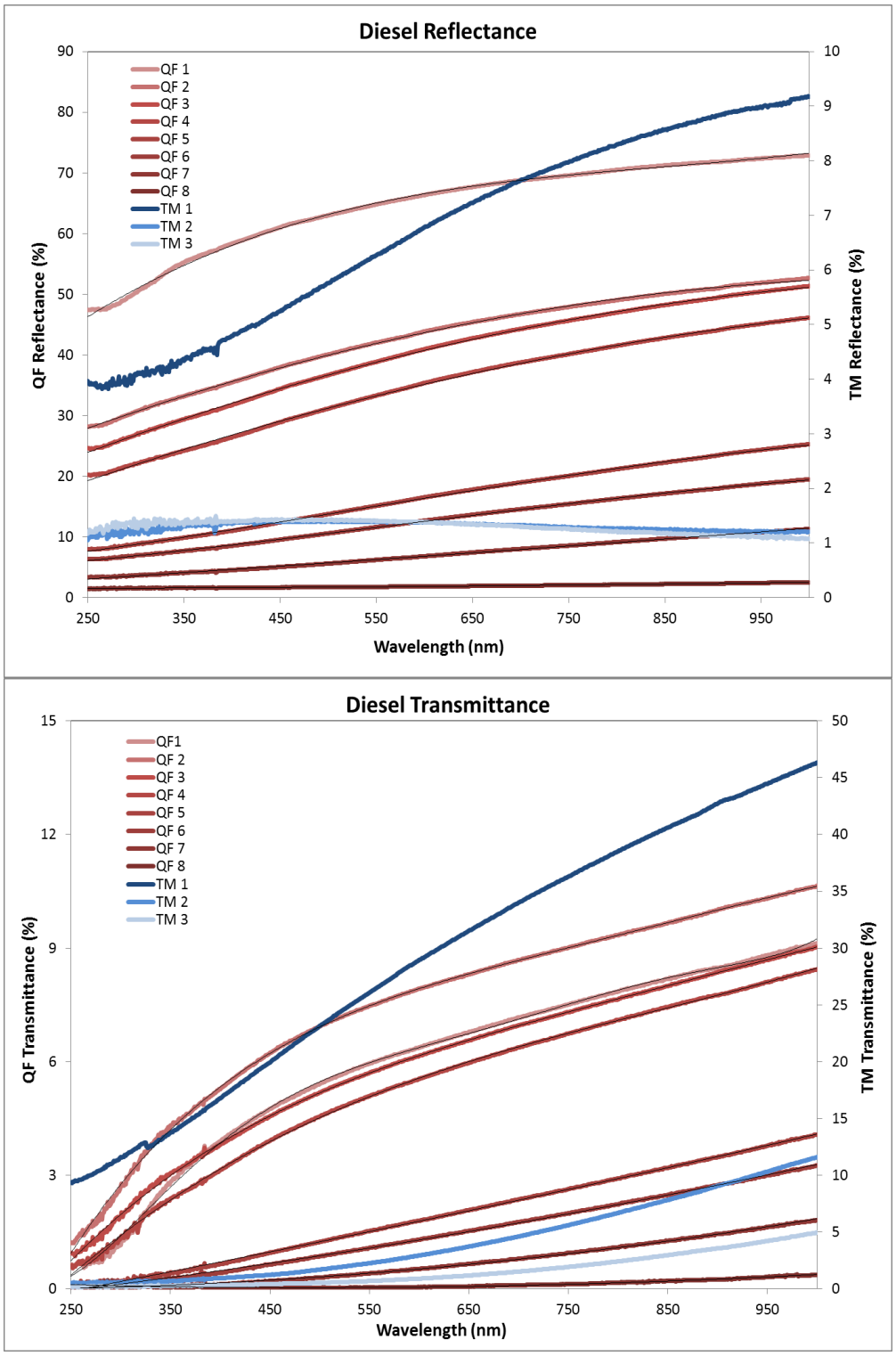


**Figure 3-5.** Reflectance (top) and transmittance (bottom) spectra for diesel-engine exhaust samples. Red curves represent QF samples and blue curves represent TM samples. Sample loading increases from QF 1 to QF 8, and for TM 1 to TM 3. There are no QF and TM filter pairs for the diesel–engine exhaust samples.

### 3.1.2 Layered Source Samples

The layered source filter reflectance and transmittance spectra shown and discussed in this section are those for the second set of eight filter pairs (see Table 2-5 for Samples MJQ/T012-018) as they are more lightly loaded than the first set. TM sample #16 was damaged post-sampling and is thus not included in further analysis.

Figures 3-7 and 3-8 show the reflectance and transmission measurements, respectively, of the QF and TM layered sample filters. Several samples visually exhibit reflectance and transmittance characteristics of smoldering biomass (rapidly decreasing response from the visual range into the UV). Sample #18, which has the highest percentage of biomass (92%), displays this most clearly and generally has the highest reflectance and transmittance values at NIR wavelengths for both QF and TM samples. Only QF sample #12 has higher transmittance than #18 and this may be due to its lighter mass loading.

The order of the layers seems to play some role in the amount of light reflected or transmitted. For QF, higher transmittances were observed for samples with a top layer of biomass emission (Figure 3-8). These curves have a general decreasing response from 950 to 350 nm, similar to the diesel source samples. The transmittances decrease with reduced percentages of biomass content (or increased percentages of diesel content). The top panel of Figure 18 shows the highest transmittance response for sample #12 (66% biomass on top layer), followed by sample #13 (55% biomass), sample #14 (21% biomass)

and sample #15 (13% biomass). The exception is for sample #18 (8% diesel top layer), which responded more like a biomass sample. A similar pattern is observed for the transmittance and reflectance response from the TM samples. However, this pattern is less clear for the reflectance response of the QF samples (top panel of Figure 3-7).

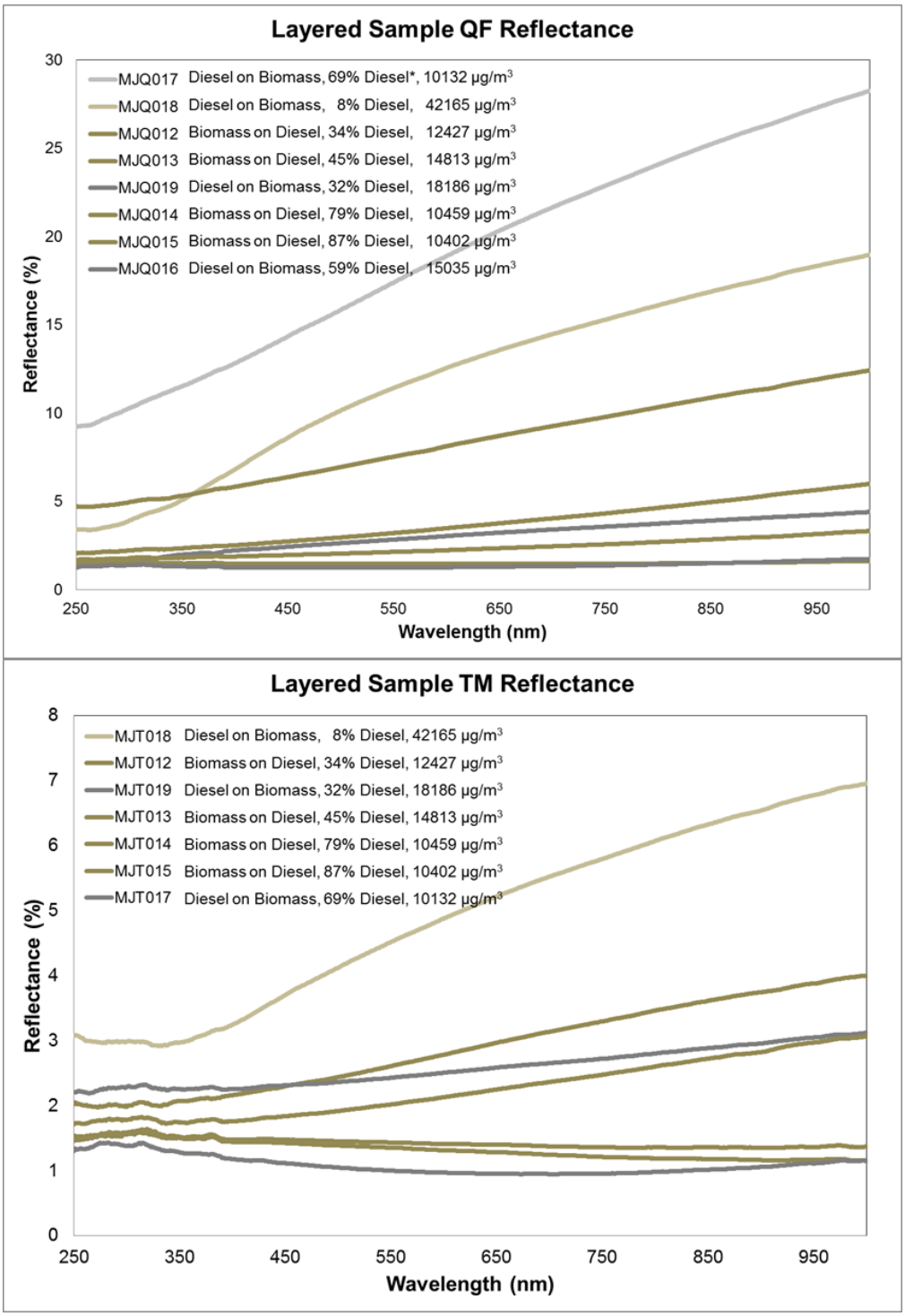


**Figure 3-6.** Layered sample reflectance for QF (top) and TM (bottom) samples. B on D samples are plotted in brown and D on B samples are plotted in gray. Legend follows order of highest to lowest response. QF sample #17 is visually different from TM sample #17 and it is likely that the QF sample has less diesel mass than the TM sample. TM sample reflectance tends to be lower for samples with higher percentages of diesel content while the pattern is harder to discern for the QF samples.

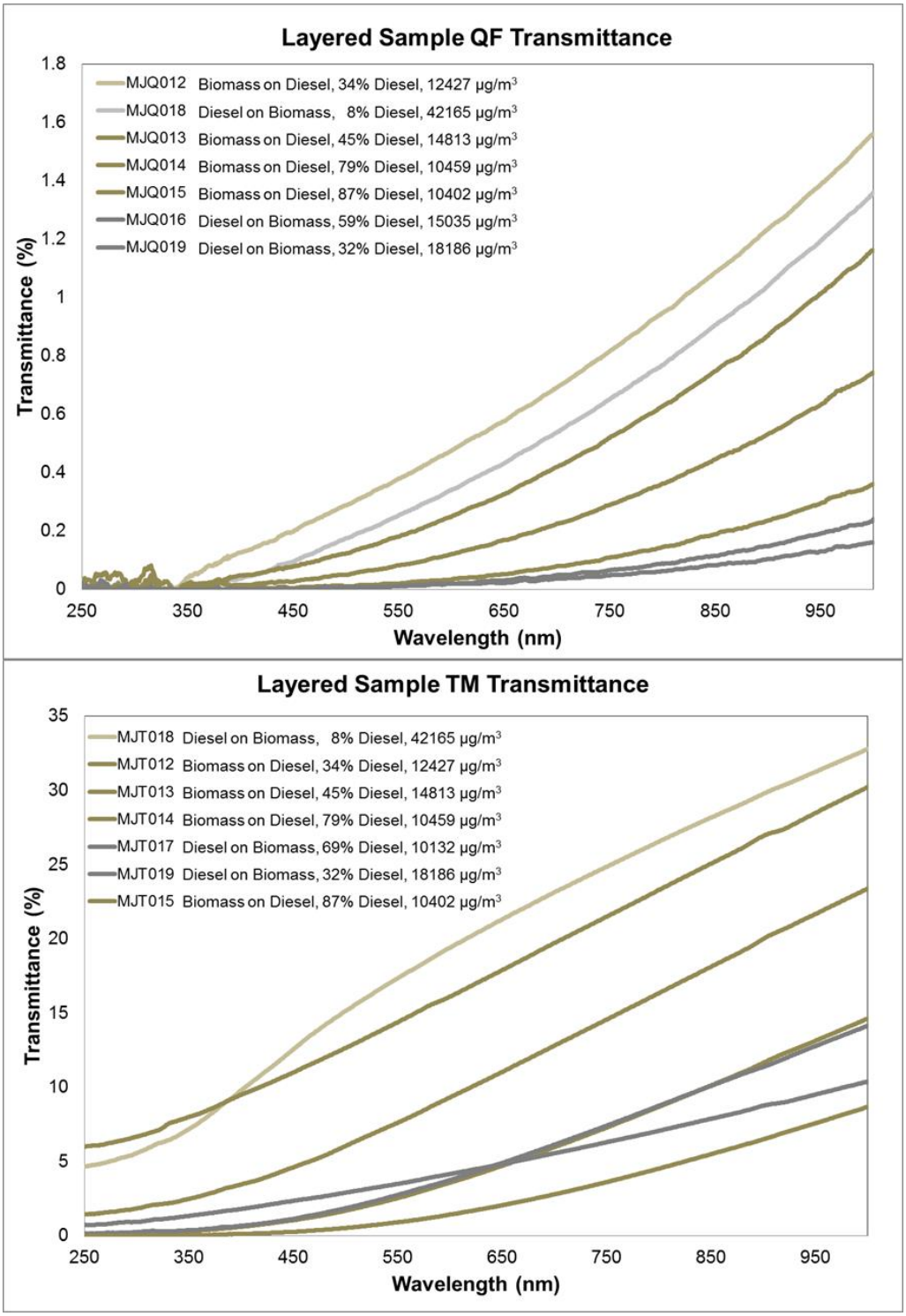


**Figure 3-7.** Layered sample transmittance for QF (top) and TM (bottom) samples. B on D samples are plotted in brown and D on B samples are plotted in gray. Legend follows order of highest to lowest response. Due to lighter loading, QF sample #17 was not included in the QF transmittance figure in order to better distinguish among the other samples. Both QF and TM sample transmittance is generally lower for samples with a smaller biomass emission content.

### 3.1.3 Ambient Samples

In the reflectance and transmittance figures for the ambient samples, TM samples are displayed as dashed lines and QF samples are displayed as solid lines. The matching TM and QF samples are the same color and numbered in the legend.

The reflectance of the Port of LA samples (Figure 3-8) is quite low and relatively flat, as might be expected for an urban, BC dominated sample. The reflectance of the TM samples is lower than that of the QF, but the transmittance of the TM samples is higher than that of the QF.

Figures 3-9 and 3-10 show the Rim Fire reflectance and transmittance spectra, respectively. Not unexpectedly, the first half of the Rim Fire samples (i.e. BrC dominated) exhibits reflectance and transmittance characteristics similar to the biomass emission source samples. The second half are much more lightly loaded and are more spectrally flat, indicative of less ambient smoke and a more normal, urban sample.

The TCEQ Clinton St. site measurements display, for the most part, rather spectrally flat reflectance and transmittance, as shown in Figures 3-11 and 3-12, respectively. The first five samples listed in Table 2-4 were during events of high local influence (BC dominant), and the remaining were during a time of African dust transport. The dust influence can be seen in the increase of reflectance response in the visible wavelengths and decrease into the UV wavelengths. It also seems that within the local influence samples there are days that are less influenced by BC based on the

reflectance spectra that curve downward strongly beginning in the visible range (Figure 3-11). The transmittance spectra for both TM and QF decrease from the NIR to the UV but do not exhibit much difference between the local and dust influences. Note: there are no reflectance measurements for the QF TCEQ Clinton filters due to the difficult nature of measuring a halved filter with punches removed.

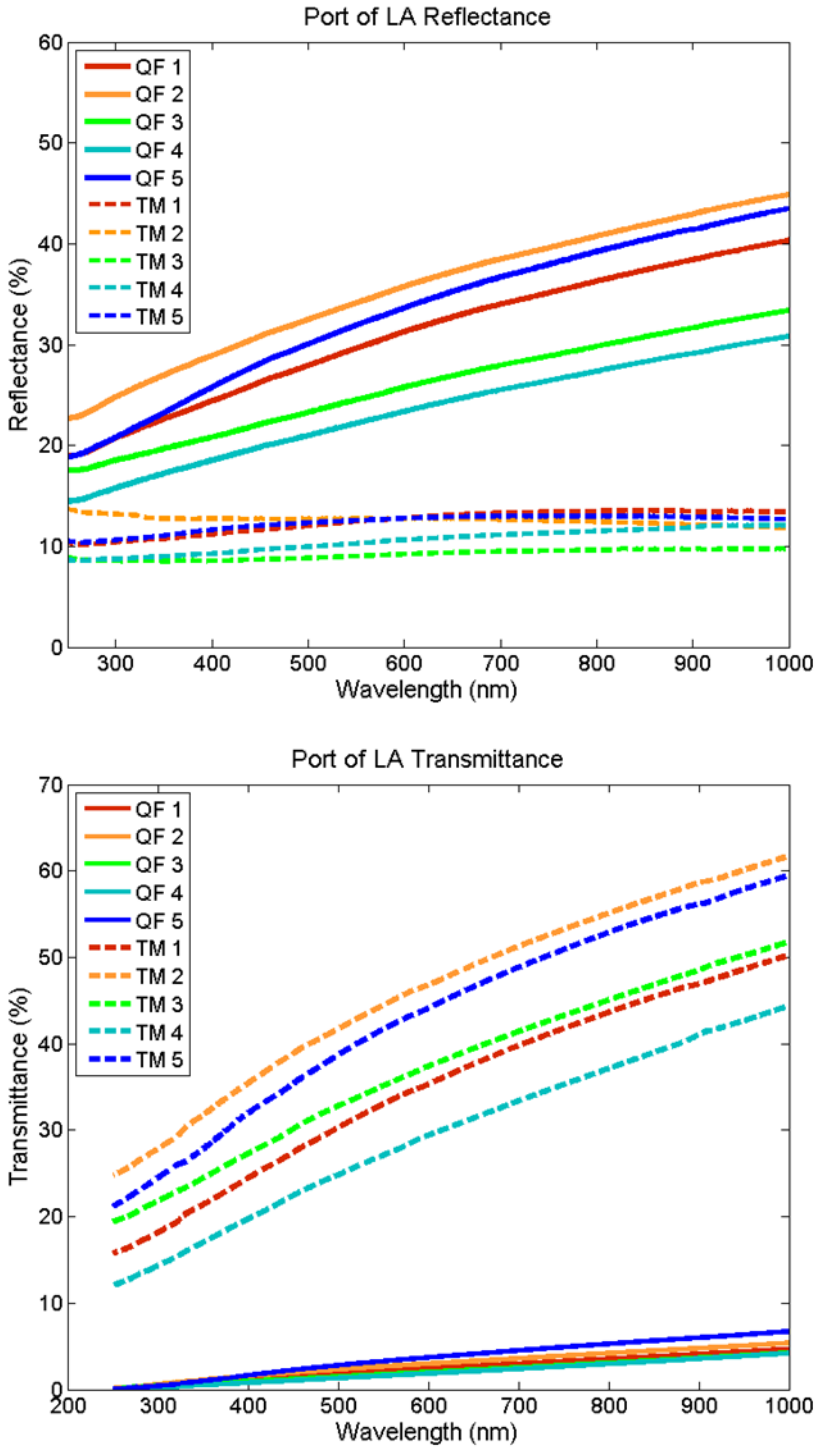


**Figure 3-8.** Reflectance (top) and transmittance (bottom) spectra for QF (solid lines) and TM (dashed lines) filter samples from the Port of LA site. Lines of QF and TM pairs are the same color. These spectra are similar to those of the diesel samples, indicating dominant contribution from BC. Order of response is similar but not the same between QF and TM.

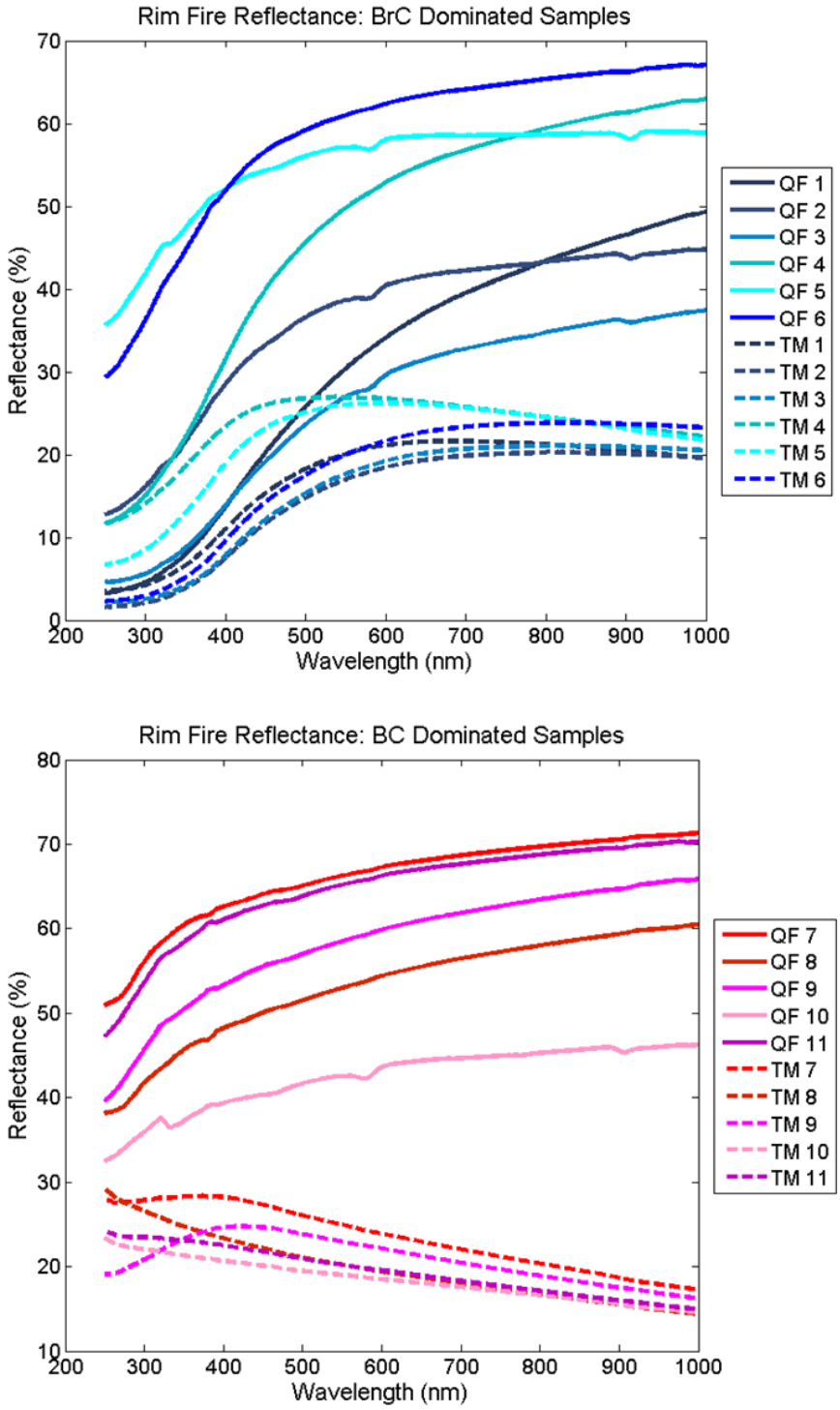


**Figure 3-9.** Reflectance spectra for Rim Fire filter samples dominated by BrC (top) and BC (bottom). QF curves are solid and TM curves are dashed. Difference in response is clearly visible from 300 – 550 nm. Order of response is similar but not the same between QF and TM pairs (indicated by same color).

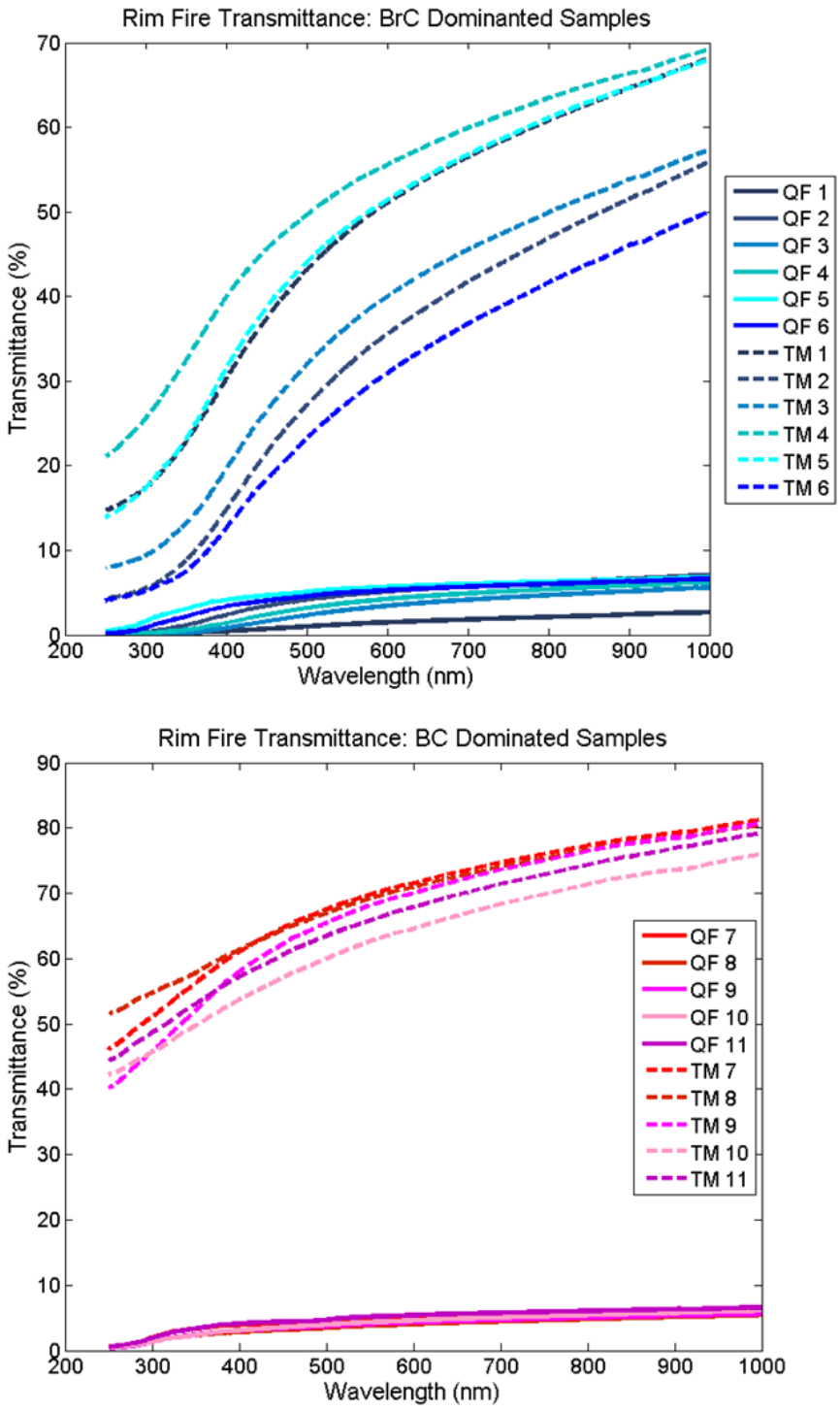


**Figure 3-10.** Rim Fire transmittance spectra for samples dominated by BrC (top) and BC (bottom). QF curves are solid and TM curves are dashed. Difference in response is clearly visible from 300 – 500 nm. Order of response is similar but not the same between QF and TM pairs (indicated by same color).

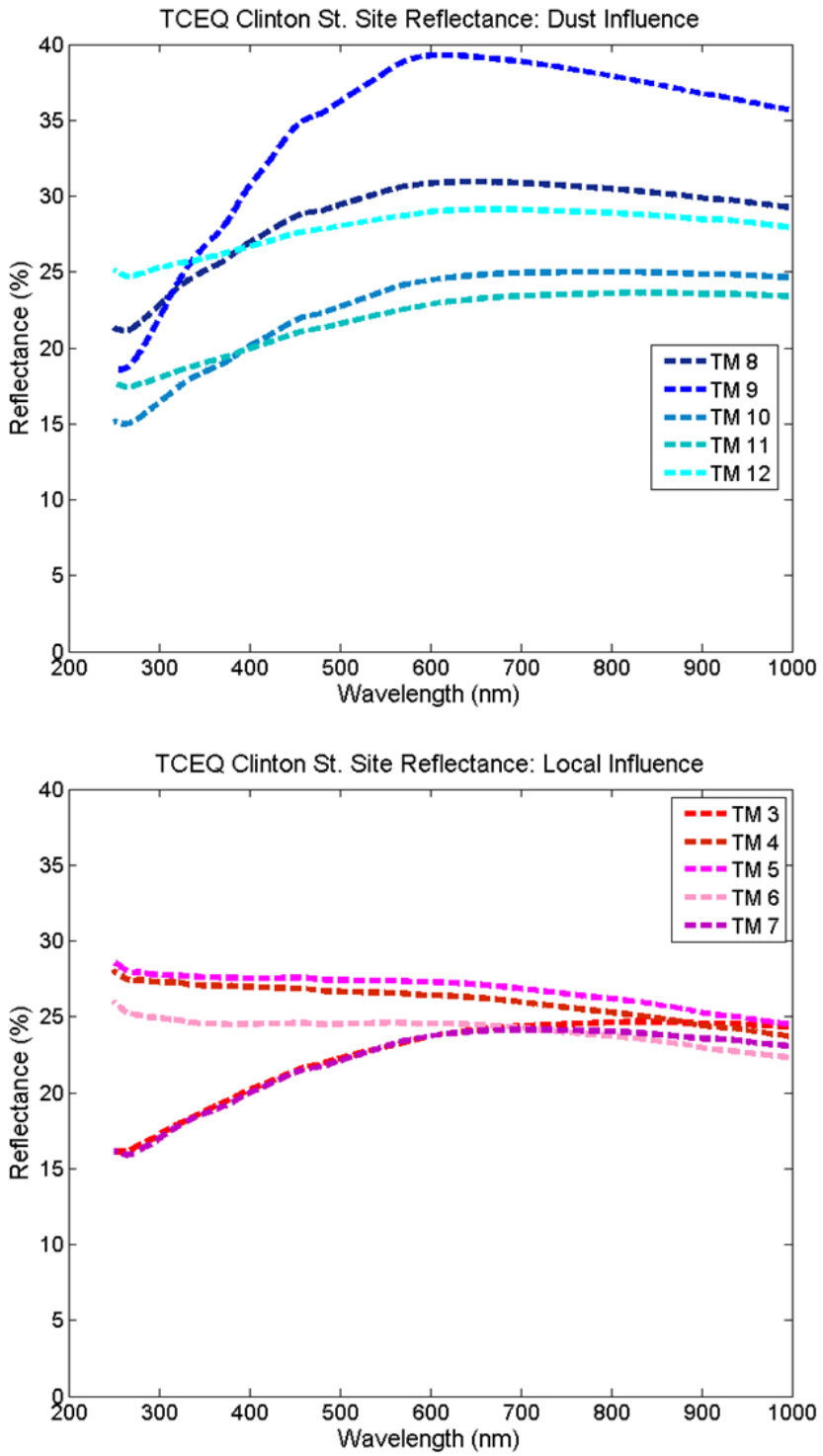


**Figure 3-11.** Reflectance spectra for TCEQ Clinton St. site TM samples. The top panel shows reflectance spectra for days under the influence of transported African dust and the bottom panel shows reflectance spectra for days under high local influence. There are no reflectance measurements of the QF samples.

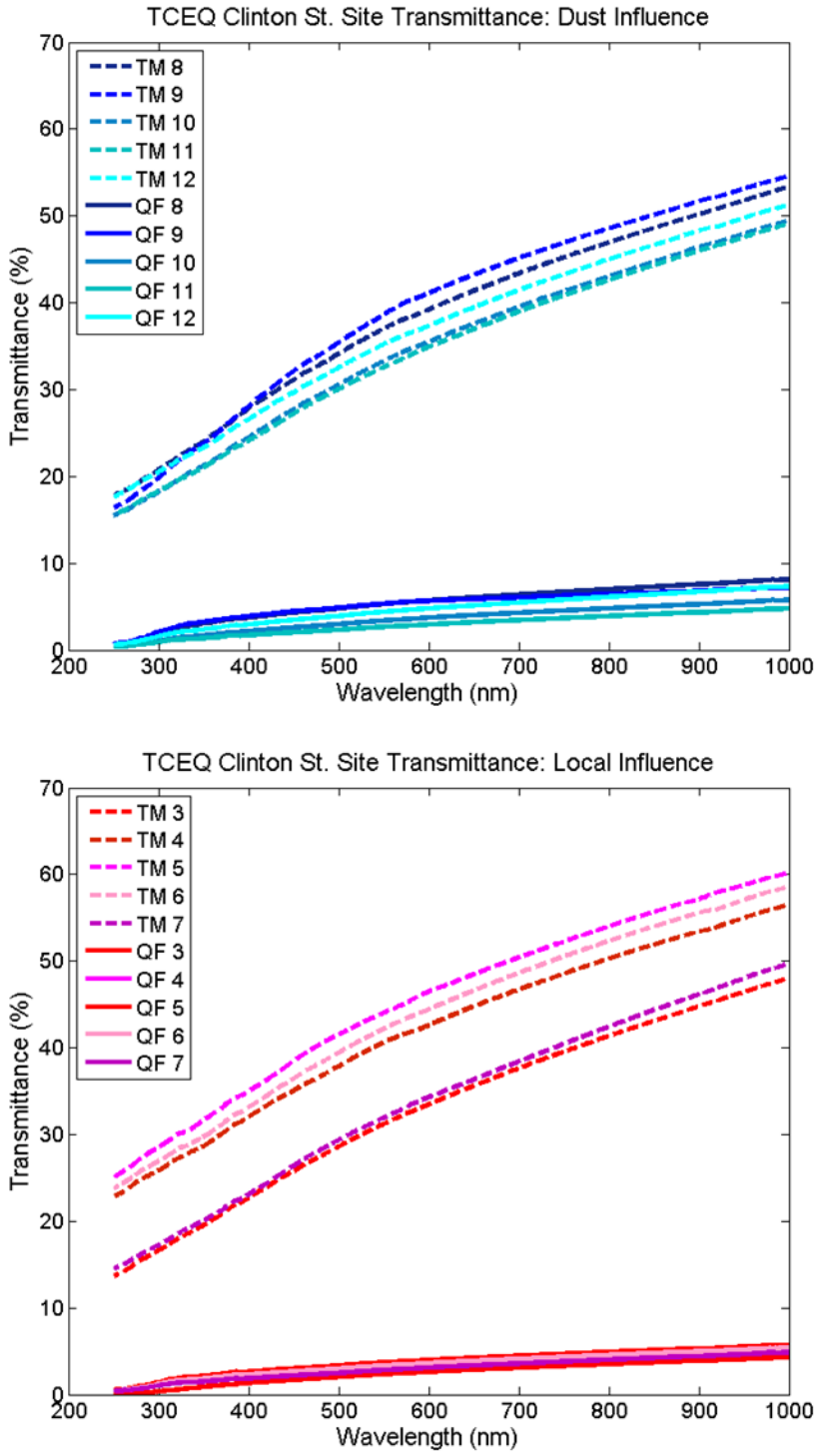


**Figure 3-12.** Transmittance spectra for TCEQ Clinton St. site samples. The top panel shows transmittance spectra for days under the influence of African dust transport and the bottom panel shows transmittance spectra for days under high local influence. QF curves are solid and TM curves are dashed. The response order of the samples is similar between TM and OF.

## 3.2 Attenuation and Absorption Calculations

Using the methods described in Section 2.2.3, attenuation (ATN), $\beta_{ATN}$, $\tau_a$ and $\beta_{abs}$ were calculated for each filter sample at every wavelength (1 nm resolution). $\beta_{ATN}$ and $\beta_{abs}$ were compared for each sample to examine the differences in absorption calculation methods. $\beta_{ATN}$ and $\beta_{abs}$ were also compared between collocated QF and TM samples to examine the differences between filter media types. For select source samples (as detailed in Section 3.2.1), $\beta_{ATN}$ and $\beta_{abs}$ values were also compared to values obtained by other light absorption methods including: a densitometer (centered at 550 nm) (Tobias Associates, Ivyland, PA), a dual-wavelength Transmissometer (370 and 880 nm) (Magee Scientific, Berkeley, CA), and a three-wavelength photoacoustic spectrometer (405, 532, and 781 nm) (DRI, Reno, NV).

For archived samples, blank filter measurements were approximated by using a project blank from the same filter batch or a similar blank filter. For the layered source samples, blank measurements of each filter were made before sampling.

Some samples do not have $\tau_a$ or $\beta_{abs}$ values due to computational errors in Equations 17 and 18 (i.e. no solution between 0 and 1), which may have been caused by using a blank filter measurement from a different filter. These samples are not used in comparisons needing $\beta_{abs}$. Additionally, the NCAQ source samples (see Table 2-4) do not have $\beta_{ATN}$ and $\beta_{abs}$ due to lack of relevant sampling information. For these samples, ATN and $\tau_a$ were used for comparisons of $\beta_{ATN}$ and $\beta_{abs}$.

### 3.2.1 Source Samples

Figure 3-13 displays a representative mass-normalized $\beta_{abs}$ spectra for each source type. As was evident in the reflectance and transmittance comparisons, the wavelength dependencies of the source types are clearly visible in this figure. The diesel and flaming wood smoke samples follow rather closely to a $\lambda^{-1}$ power law approximation and absorb more light across the spectrum than the other samples. The dust sample absorbs rather equally across the spectrum while the biomass sample absorption rapidly increases in the visible and UV wavelengths.

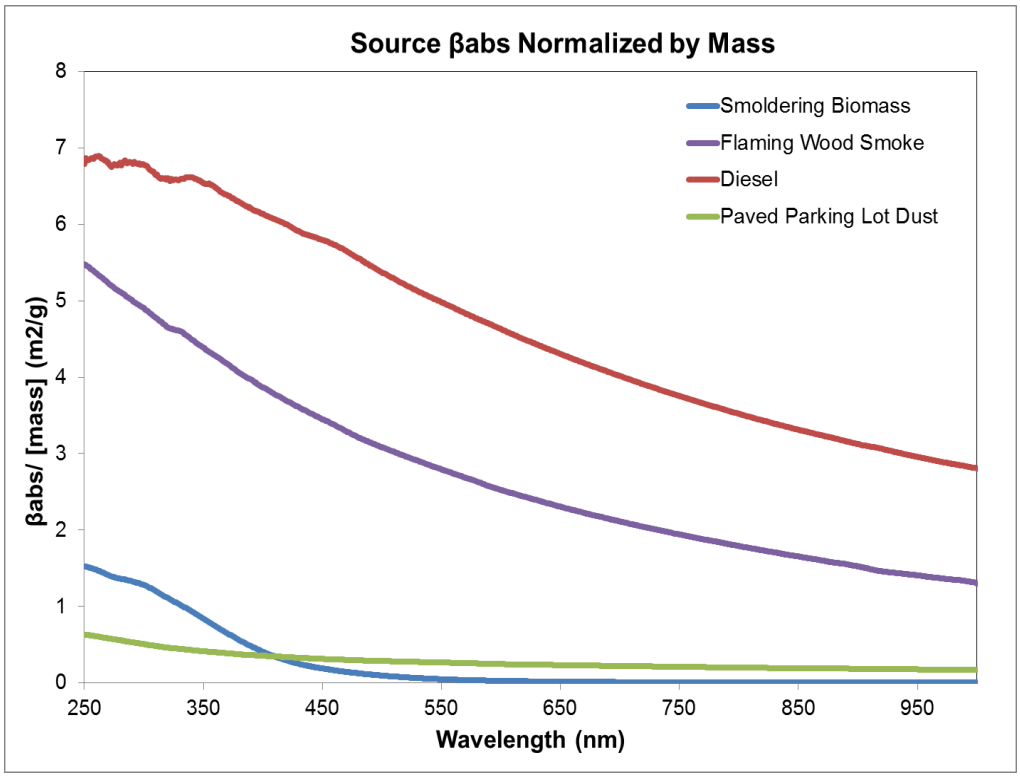


**Figure 3-13.** Absorption coefficient spectra for each source type, normalized by the sample mass concentration.

Figure 3-14 compares representative mass normalized $\beta_{ATN}$ and $\beta_{abs}$ spectra for each source type. $\beta_{ATN}$ and $\beta_{abs}$ are essentially identical for the diesel sample (Figure 3-14 d) but for the other source types there is an obvious difference between the two coefficients, especially at longer wavelengths.

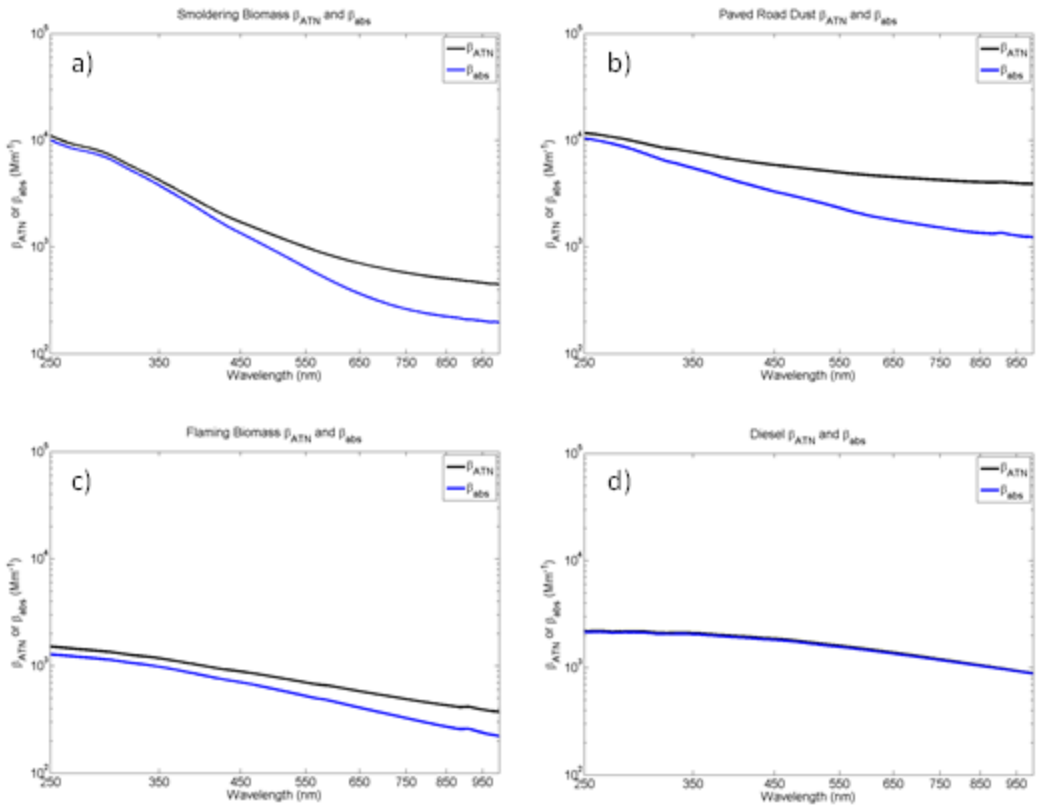


**Figure 3-14.** $\boldsymbol{\beta_{ATN}}$(black curve) and $\boldsymbol{\beta_{abs}}$(blue curve) for four TM source samples including: a) smoldering biomass, b) dust, c) flaming wood and d) diesel. The diesel sample $\boldsymbol{\beta_{abs}}$ is well represented by $\boldsymbol{\beta_{ATN}}$but there are discrepancies between the $\boldsymbol{\beta_{ATN}}$ and $\boldsymbol{\beta_{abs}}$ of other source types, especially with increasing wavelength.

Direct (1:1) comparison between $\beta_{ATN}$ and $\beta_{abs}$ for source samples reflects good agreement with high correlations. When excluding values where the attenuation is

greater than five[2], the source samples $\beta_{ATN}$ and $\beta_{Abs}$ are well represented by a linear relationship. The slope and intercept of these relationships are listed in Table 3-1. For all samples, the $\beta_{ATN}$ value is always larger than the $\beta_{Abs}$, as is expected, and the slope between $\beta_{ATN}$ and $\beta_{Abs}$ is approximately one (average of 1.10). The dust samples have the most variable slope values and they are generally less than one, Note: only TM dust samples were compared because there are not $\beta_{Abs}$ values for the QF red dust samples. QF samples have an average slope and intercept of 1.25 + 0.17 while the TM samples have an average slope and intercept of 0.94 + 0.13.

For the source samples that were collected simultaneously on both TM and QF media, which include the DBI biomass samples and the red dust samples, comparisons were made between the attenuation, $\beta_{ATN}$ and $\beta_{abs}$ values for the QF and TM samples. Table 3-2 lists the slopes and intercepts of the linear comparisons between the QF and TM samples. Across the board, the TM values are 40 – 60% lower than the QF values. On average, the TM biomass values are approximately one third of the QF values (average slope of 0.31) and the TM red dust values are approximately two thirds of the QF values (average slope of 0.67). Again, there are no $\beta_{Abs}$ values for the red dust QF samples due to computational issues potentially caused by the surrogate blank filter measurement.

[2] Many filter-based light transmission samplers, like the aethalometer, switch to a new sample spot when the attenuation of the sample reaches one (Arnott, 2015, personal correspondence).

**Table 3-1.** Relationships Between Sample $\boldsymbol{\beta_{ATN}}$ and $\boldsymbol{\beta_{abs}}$ Calculations

| Sample ID | Source Type | $\beta_{ATN}$ vs. $\beta_{abs}$ | | |
|---|---|---|---|---|
| | | Slope | Intercept ($m^2/g$) | $R^2$ |
| BIOTKF072 | Bitterbrush Stems | 1.03 | 0.06 | 0.999 |
| BIOTKF086 | Carpet Leaves | 1.06 | 0.04 | 0.999 |
| BIOTKF088 | Wet Duff | 0.95 | 0.17 | 0.999 |
| BIOTKF102 | Wet Litter | 0.97 | 0.07 | 0.999 |
| REST339 | Paved Parking Lot Dust | 1.04 | 0.16 | 0.995 |
| REST1856 | Paved Road Dust | 0.85 | 0.09 | 0.999 |
| REST2015 | Taconite Dust | 0.73 | 0.04 | 0.998 |
| REST2102 | De-icing Material | 0.96 | 0.12 | 0.996 |
| STRST061 | Diesel | 1.03 | 0.06 | 0.999 |
| STRST064 | Diesel | 1.03 | 0.04 | 0.999 |
| STRST111 | Acetylene Flame | 1.02 | 0.04 | 0.999 |
| STRST133 | Flaming Wood Smoke | 1.06 | 0.51 | 0.999 |
| STRST136 | Flaming Wood Smoke | 1.14 | 0.50 | 0.999 |
| DBIT001 | Pine Needle | 0.93 | 0.21 | 0.996 |
| DBIT002 | Pine Needle | 0.96 | 0.25 | 0.986 |
| DBIT003 | Pine Needle | 0.92 | 0.18 | 0.966 |
| DBIT005 | Cheat Grass | 0.91 | 0.16 | 0.963 |
| DBIT006 | Cheat Grass | 0.92 | 0.18 | 0.997 |
| DBIT007 | Cheat Grass | 0.94 | 0.29 | 0.987 |
| DBIQ1001 | Pine Needle | 1.10 | 0.48 | 0.984 |
| DBIQ1002 | Pine Needle | 1.10 | 0.32 | 0.961 |
| DBIQ1003 | Pine Needle | 1.14 | 0.29 | 0.963 |
| DBIQ1005 | Cheat Grass | 1.39 | 0.22 | 0.905 |
| DBIQ1006 | Cheat Grass | 1.07 | 0.36 | 0.984 |
| DBIQ1007 | Cheat Grass | 1.16 | 0.24 | 0.955 |
| NCAQ091 | Diesel | 1.12 | 0.17 | 0.999 |
| NCAQ092 | Diesel | 1.08 | 0.19 | 0.999 |
| NCAQ093 | Diesel | 1.02 | 0.26 | 0.999 |
| NCAQ094 | Diesel | 2.40 | 0.06 | 0.996 |
| NCAQ095 | Diesel | 1.02 | 0.06 | 0.999 |
| NCAQ042 | Peat | 1.19 | 0.09 | 0.987 |
| NCAQ072 | Peat | 1.65 | 0.04 | 0.988 |
| NCAQ077 | Peat | 1.11 | 0.20 | 0.987 |
| NCAQ079 | Peat | 1.04 | 0.18 | 0.993 |
| NCAQ053 | Pine Cone | 1.18 | 0.13 | 0.991 |
| NCAQ080 | Pine Needle | 1.77 | -0.09 | 0.999 |
| NCAQ081 | Pine Needle | 1.45 | -0.05 | 0.999 |

| | | | | |
|---|---|---|---|---|
| NCAQ082 | Pine Needle | 1.26 | 0.04 | 0.999 |
| NCAQ083 | Pine Needle | 1.14 | 0.21 | 0.999 |
| NCAQ084 | Pine Needle | 1.10 | 0.37 | 0.999 |
| NCAQ085 | Pine Needle | 1.07 | 0.34 | 0.999 |
| NCAQ086 | Pine Needle | 1.04 | 0.34 | 0.998 |

**Table 3-2.** Comparisons between collocated QF and TM source samples.

| Filter Pair | Source Type | QF vs. TM | Slope | Intercept[a] | $R^2$ | n |
|---|---|---|---|---|---|---|
| DBIT001/Q1001 | Pine Needle | ATN | 0.32 | 0.22 | 0.99 | 688 |
| | | $\beta_{ATN}$ | 0.36 | 0.11 | 0.99 | |
| | | $\beta_{abs}$ | 0.35 | 0.1 | 0.99 | |
| DBIT002/Q1002 | Pine Needle | ATN | 0.31 | 0.31 | 0.98 | 642 |
| | | $\beta_{ATN}$ | 0.35 | 0.13 | 0.98 | |
| | | $\beta_{abs}$ | 0.36 | 0.07 | 0.97 | |
| DBIT003/Q1003 | Pine Needle | ATN | 0.24 | 0.38 | 0.96 | 649 |
| | | $\beta_{ATN}$ | 0.28 | 0.41 | 0.96 | |
| | | $\beta_{abs}$ | 0.29 | 0.34 | 0.95 | |
| DBIT005/Q1005 | Cheat Grass | ATN | 0.20 | 0.21 | 0.95 | 669 |
| | | $\beta_{ATN}$ | 0.26 | 0.34 | 0.96 | |
| | | $\beta_{abs}$ | 0.29 | 0.21 | 0.93 | |
| DBIT006/Q1006 | Cheat Grass | ATN | 0.32 | 0.20 | 0.99 | 642 |
| | | $\beta_{ATN}$ | 0.35 | 0.10 | 0.99 | |
| | | $\beta_{abs}$ | 0.38 | 0.07 | 0.98 | |
| DBIT007/Q1006 | Cheat Grass | ATN | 0.27 | 0.32 | 0.98 | 665 |
| | | $\beta_{ATN}$ | 0.32 | 0.27 | 0.98 | |
| | | $\beta_{abs}$ | 0.33 | 0.09 | 0.96 | |
| REST2183/Q2193[b] | Red Dust (PM 2.5) | ATN | 0.63 | 0.06 | 0.81 | 751 |
| | | $\beta_{ATN}$ | 0.7 | 0.0001 | 0.81 | |
| REST2184/Q2194 | Red Dust (PM10) | ATN | 0.87 | 0.07 | 0.91 | 751 |
| | | $\beta_{ATN}$ | 0.95 | 5.00E-05 | 0.91 | |
| REST2185/Q2195 | Red Dust (PM 2.5) | ATN | 0.56 | 0.07 | 0.95 | 751 |
| | | $\beta_{ATN}$ | 0.62 | 0.0001 | 0.95 | |
| REST2186/Q2196 | Red Dust (PM10) | ATN | 0.49 | 0.07 | 0.83 | 751 |
| | | $\beta_{ATN}$ | 0.53 | 4.00E-05 | 0.83 | |

[a] Intercept units for $\beta_{ATN}$ and $\beta_{abs}$ are $Mm^{-1}$; ATN is unitless.

[b] No $\beta_{abs}$ values for red dust QF samples.

### 3.2.1.1 Comparison with Other Light Absorption Methods

Several TM source samples were measured with a Tobias TBX densitometer, which uses a light source centered at 550 nm to measure $\beta_{abs}$ (see Section 1.6). Comparisons of the densitometer and Lambda 35 measurements of $\beta_{abs}$ are presented in Table 3-3. The densitometer reports higher $\beta_{abs}$ than the Lambda 35 at 550 nm for most samples. The two flaming wood smoke samples (STRST 133 and 136) have percent differences of 0.12 and 23%, exhibiting large variability. The best comparison is found for the two diesel samples with 0.5 and 9.2% difference. The largest differences were found for dust (38 – 87%) and biomass (28 – 122%) samples.

**Table 3-3.** Source Sample $\beta_{abs}$ ($Mm^{-1}$) from Densitometer and Lambda 35

| Sample ID | Source Type | Densitometer $\beta_{abs}$ (@ 550 nm) ($Mm^{-1}$) | Lambda 35 $\beta_{abs}$ (@ 550 nm) ($Mm^{-1}$) | % Difference[a] |
|---|---|---|---|---|
| BIOTK072 | Bitterbrush Stems | 2376 ± 157 | 1777 ± 91 | 28.8 |
| BIOTK086 | Carpet Leaves | 933 ± 162 | 645 ± 33 | 36.4 |
| BIOTK088 | Wet Duff | 642 ± 82 | 154 ± 8 | 122.6 |
| BIOTK102 | Wet Litter | 2050 ± 127 | 1368 ± 70 | 39.9 |
| REST339 | Paved Parking Lot Dust | 15253 ± 1583 | 7702 ± 393 | 65.8 |
| REST1856 | Paved Road Dust | 5927 ± 663 | 2332 ± 119 | 87.1 |
| REST2015 | Taconite Dust | 10869 ± 696 | 7375 ± 377 | 38.3 |
| REST2102 | De-icing Material | 16849 ± 3177 | 7154 ± 365 | 80.8 |
| STRST061 | Diesel | 1577± 80 | 1569 ± 80 | 0.5 |
| STRST064 | Diesel | 2001± 157 | 2194 ± 112 | 9.19 |
| STRTQ111 | Acetylene Flame | 1545 ± 78 | 1842 ± 94 | 17.57 |
| STRTQ133 | Flaming Wood Smoke | 665 ± 48.6 | 527 ± 27 | 23.18 |
| STRTQ136 | Flaming Wood Smoke | 333 ± 39 | 333 ± 17 | 0.12 |

[a] Percent difference calculated as $100 * |A - B| / \frac{(A+B)}{2}$

The samples in Table 3-3 were also measured with a Magee SootScan Model OT21 dual wavelength (370 & 880 nm) transmissometer. This instrument measures light transmission through a blank and sample filter on top of a diffusing filter at two wavelengths and reports the sample attenuation as $ATN = (100)\ln\left(\frac{blank\ filter\ transmission}{sample\ filter\ transmission}\right)$. The samples analyzed with this instrument did not have transmission measurements made through the blank filter prior to sampling, so the attenuation values were calculated using archived blank filters. $\beta_{ATN}$ values were calculated for each sample at both wavelengths using Equation 17, and were compared to the $\beta_{ATN}$ values found using the Lambda 35 at those wavelengths. These values are reported in Table 3-4

Better comparisons are found for the diesel and flaming wood smoke (i.e. BC dominated) samples with 5 -17% difference at 880 nm. The wet duff sample (BIOTKF088) has the best comparison at 370 nm with a 15.5% difference. On average, the comparisons are better at 880 nm (average 36.7% difference) than at 370 nm (average 101.5% difference). This may be due to the differences in measurement method, specifically due to the effect of the diffusing filter on the sample filter.

**Table 3-4.** Source Sample $\beta_{ATN}$ ($Mm^{-1}$) from Magee Transmissometer and Lambda 35

| Sample ID | Source Type | Magee $\beta_{ATN}$ ($Mm^{-1}$) | | Lambda 35 $\beta_{ATN}$ ($Mm^{-1}$) | | % Difference[a] | |
|---|---|---|---|---|---|---|---|
| | | 880 nm | 370 nm | 880 nm | 370 nm | 880 nm | 370 nm |
| BIOTK072 | Bitterbrush Stems | 1331 ± 67 | 13573 ± 679 | 1180 ± 59 | 2939 ± 147 | 12 | 129 |
| BIOTK086 | Carpet Leaves | 68 ± 3 | 527 ± 26 | 494 ± 25 | 3438 ± 172 | 151 | 147 |
| BIOTK088 | Wet Duff | 181 ± 9 | 2182 ± 109 | 530 ± 27 | 2549 ± 128 | 98 | 16 |
| BIOTK102 | Wet Litter | 1125 ± 56 | 18409 ± 920 | 1224 ± 61 | 3329 ± 167 | 8 | 139 |
| REST339 | Paved Parking Lot Dust | 7365 ± 368 | 23634 ± 1182 | 10176 ± 510 | 16691 ± 836 | 32 | 34 |
| REST1856 | Paved Road Dust | 3014 ± 151 | 12580 ± 629 | 4040 ± 202 | 7246 ± 363 | 29 | 54 |
| REST2015 | Taconite Dust | 5403 ± 270 | 36636 ± 1832 | 5804 ± 291 | 8186 ± 410 | 7 | 127 |
| REST2102 | De-icing Material | 5835 ± 292 | 20232 ± 1012 | 11665 ± 584 | 31962 ± 1601 | 67 | 45 |
| STRST061 | Diesel | 1214 ± 61 | 42609 ± 2130 | 1022 ± 51 | 2060 ± 103 | 17 | 182 |
| STRST064 | Diesel | 1645 ± 82 | 60309 ± 3015 | 1525 ± 76 | 2619 ± 131 | 8 | 183 |
| STRST133 | Flaming Wood Smoke | 395 ± 20 | 3033 ± 152 | 416 ± 21 | 1110 ± 56 | 5 | 93 |
| STRST136 | Flaming Wood Smoke | 291 ± 15 | 1293 ± 65 | 275 ± 14 | 620 ± 31 | 6 | 70 |

[a] Percent difference calculated as $100 * |A - B| / \frac{(A+B)}{2}$

A biomass burning project that concurrently sampled PM with a 3-$\lambda$ PAS (405, 532, and 781 nm) and onto QF and TM filters allowed for a direct comparison of filter-based and in-situ absorption measurements. Table 3-5 summarizes the ratios of $\beta_{abs}$ between the QF and TM filter media and between filter and PAS for the three wavelengths. As illustrated in Figure 3-15, $\beta_{abs}$ values obtained from the QF and TM filters were regularly higher than those measured by the PAS[3], though the TM values

[3] Due to the nature of the laboratory burning sampling, PAS $\beta_{abs}$values were averaged over the same time period as the filter sampling for comparison to filter $\beta_{abs}$values.

tend to fall within the standard deviation of the PAS values at 405 nm. On average, QF $\beta_{abs}$ values were higher than PAS values by factors of 3.7, 5.4 and 6.2 at 405, 532 and 781 nm, respectively, and TM $\beta_{abs}$ measurements were higher than PAS values by factors of 1.8, 3.9, and 5.2 at 405, 532, and 781 nm, respectively. Table 3-5 also highlights the difference between $\beta_{abs}$ obtained from QF and TM samples – QF samples give higher $\beta_{abs}$ values than TM, on average, by factors of 2.1, 1.4, and 1.2 at 405, 532 and 781 nm, respectively.

The differences between QF, TM and PAS values are consistent with reports of filter enhancement in the literature (Bond et al., 1999, Arnott et al., 2005, Andreae and Gelencser 2006, Lack et al., 2008). Lack et. al (2008) observed that the level of agreement between the PAS and filter-based measurements depends on the amount of organic aerosol in the sample – specifically, disagreement between 50 and 80% was found for samples with high organic aerosol. As the comparisons in this study were made with biomass burning samples, much of the disagreement between the PAS and filter-based values may be attributable to the source type. The nature of the sample collection (laboratory control burning and sampling of biomass material) also introduces large uncertainties in $\beta_{abs}$ measurements.

**Table 3-5.** Ratios of $\beta_{abs}$ Values Obtained During Collocated Biomass Sampling

| | QF/TM | | | TM/PAS | | | QF/PAS | | |
|---|---|---|---|---|---|---|---|---|---|
| Sample | 405 nm | 532 nm | 781 nm | 405 nm | 532 nm | 781 nm | 405 nm | 532 nm | 781 nm |
| DBI001 | 2.0 | 1.4 | 1.3 | 1.9 | 3.9 | 5.2 | 3.8 | 5.6 | 6.5 |
| DBI002 | 2.0 | 1.4 | 1.3 | 2.3 | 6.4 | 8.5 | 4.5 | 9.3 | 11.2 |
| DBI003 | 2.0 | 1.6 | 1.4 | 1.6 | 2.9 | 3.8 | 3.3 | 4.5 | 5.3 |
| DBI005 | 2.1 | 1.4 | 1.1 | 1.8 | 3.2 | 4.5 | 3.8 | 4.3 | 5.1 |
| DBI006 | 2.2 | 1.4 | 1.0 | 1.4 | 3.4 | 5.2 | 3.2 | 4.6 | 5.0 |
| DBI007 | 2.2 | 1.3 | 1.0 | 1.6 | 3.3 | 4.3 | 3.4 | 4.3 | 4.3 |
| Average | 2.1 | 1.4 | 1.2 | 1.8 | 3.9 | 5.2 | 3.7 | 5.4 | 6.2 |

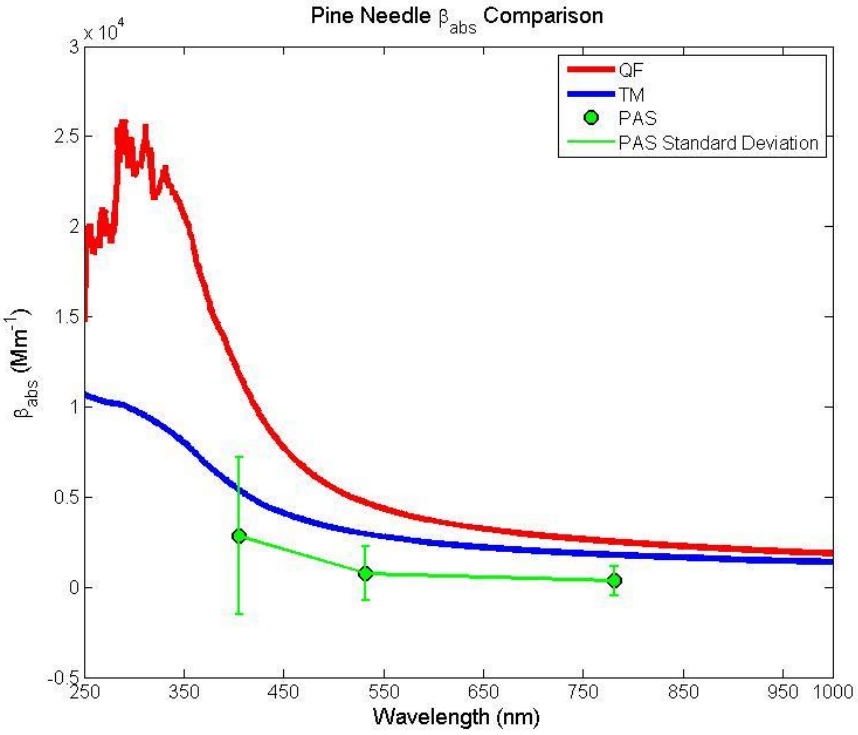


**Figure 3-15.** Comparison of biomass burning $\boldsymbol{\beta_{abs}}$ values obtained from TM, QF, and photoacoustic samples of burning pine needles (sample DBIT001 and DBIQ1001).

### 3.2.2 Layered Source Samples

Due to the heavily loaded nature of the layered source samples, only measurements with ATN < 5 were considered for further calculations. As mentioned above, several filter-based light transmission samplers, like the aethalometer, switch to a new sample spot when the attenuation of the sample reaches one so ATN < 5 is still a very high value to be considered (Arnott, 2015, personal correspondence). While this limits the comparisons that can be made across the measured wavelength spectrum as well as between QF and TM filter media, there are still useful relationships to be examined.

When comparing the attenuation and absorption calculations (ATN, $\beta_{ATN}$, $\beta_{abs}$) for the layered source samples, the QF values are generally higher than the TM values. This is consistent with observations from the source samples. Figure 3-16 shows the comparison between the TM and QF $\beta_{ATN}$ of a layered sample before and after the removal of measurements of attenuation greater than five.

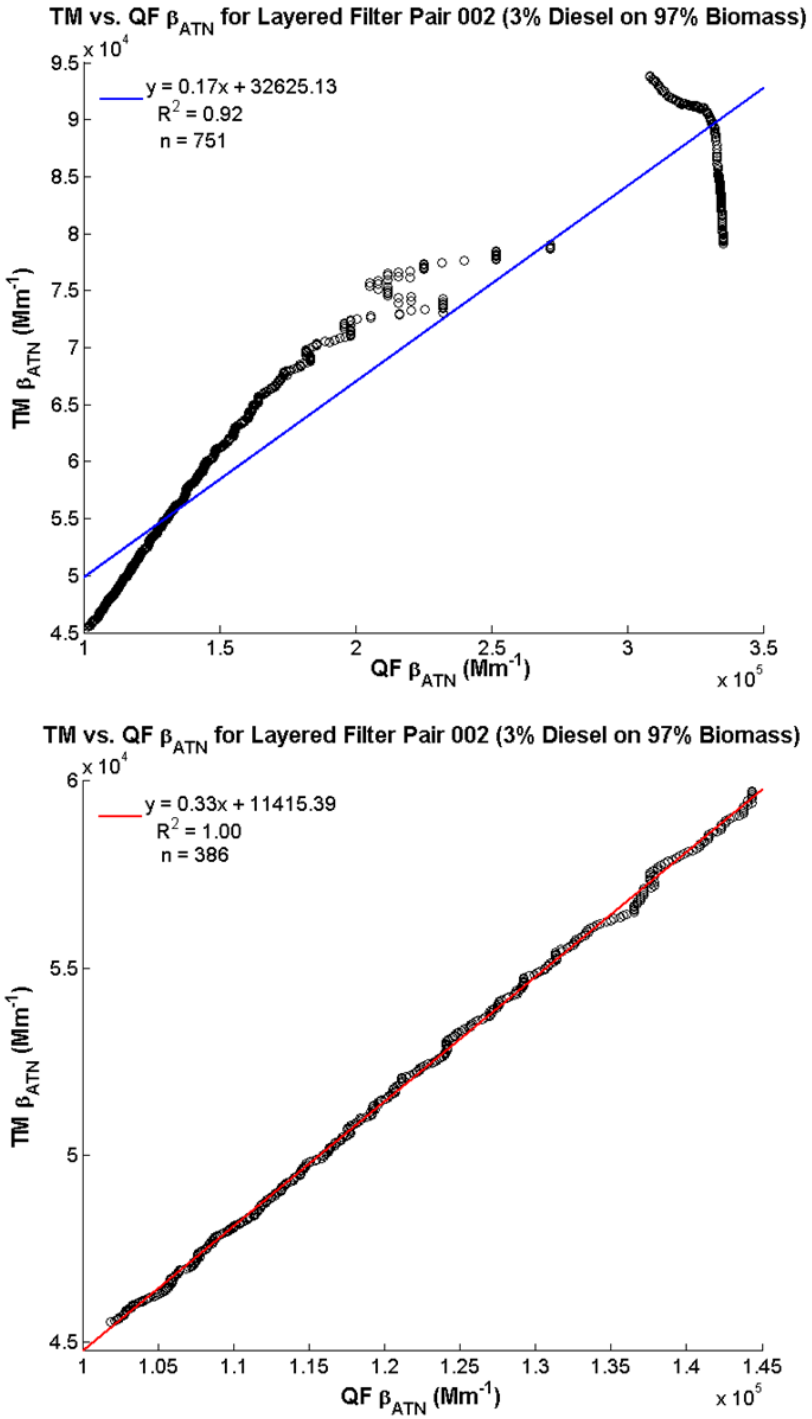


**Figure 3-16.** Relationship between TM and QF $\boldsymbol{\beta_{abs}}$ values for a paired layered source sample. The top plot examines the full relationship while the bottom plot examines the linear relationship at attenuation values less than five.

For attenuation values less than five, the relationship between the TM vs. QF for ATN, $\beta_{abs}$ and $\beta_{ATN}$ values is linear. Table 3-6 lists the slopes and intercepts of the linear relationships between layered sample filter types. On average, the TM attenuation is approximately half of the QF attenuation (average slope of 0.52) with a positive offset of 0.06. The TM $\beta_{ATN}$ and $\beta_{abs}$ are slightly larger than half of the QF $\beta_{ATN}$ and $\beta_{abs}$ with 0.55 and 0.58 slopes, respectively, and positive intercepts of 1260 and 4296 $Mm^{-1}$ (on scales of $1x10^4$).

The shift from a linear relationship at low attenuation values to a non-linear relationship at higher values provides insight into the filter loading and filter matrix effects of this light absorption method. The non-linearity occurs when the QF attenuation values continue to increase while the TM values stay relatively flat. This could be an indication that heavy particle loading on TM filters causes a shadowing effect. This loading/matrix effect begins at the shorter wavelengths and gradually affects the measurements at higher wavelengths with increasing mass loadings.

To explore this relationship, the lowest usable wavelength (e.g. the lowest wavelength where the attenuation was less than five) for the layered and several source samples was plotted against sample masses and carbon loadings in Figures 3-17 and 3-18, respectively.

**Table 3-6.** Layered Sample TM & QF Linear Relationship Slopes and Intercepts

| Sample Pair | Layering Order and Mass Ratio | TM vs. QF Slope | | Intercept[a] | $R^2$ | n |
|---|---|---|---|---|---|---|
| MJT/Q002 | Diesel on Biomass 3:97 | ATN | 0.31 | 0.36 | 1.00 | 386 |
| | | $\beta_{ATN}$ | 0.33 | 11415 | 1.00 | |
| | | $\beta_{abs}$ | 0.35 | 13625 | 1.00 | |
| MJT/Q003 | Diesel on Biomass 71:29 | ATN | 0.61 | 0.37 | 0.99 | 140 |
| | | $\beta_{ATN}$ | 0.67 | 4986 | 0.99 | |
| | | $\beta_{abs}$ | 0.67 | 5212 | 0.99 | |
| MJT/Q005 | Diesel on Biomass 30:70 | ATN | 0.58 | 0.28 | 1.00 | 286 |
| | | $\beta_{ATN}$ | 0.63 | 4448 | 1.00 | |
| | | $\beta_{abs}$ | 0.62 | 5026 | 1.00 | |
| MJT/Q008 | Biomass on Diesel 73:27 | ATN | 0.49 | 0.21 | 1.00 | 274 |
| | | $\beta_{ATN}$ | 0.56 | 2433 | 1.00 | |
| | | $\beta_{abs}$ | 0.55 | 2769 | 1.00 | |
| MJT/Q012 | Biomass on Diesel 66:34 | ATN | 0.43 | 0.14 | 0.98 | 634 |
| | | $\beta_{ATN}$ | 0.48 | 4070 | 0.98 | |
| | | $\beta_{abs}$ | 0.48 | 7646 | 0.98 | |
| MJT/Q013 | Biomass on Diesel 55:45 | ATN | 0.58 | - 0.17 | 1.00 | 560 |
| | | $\beta_{ATN}$ | 0.65 | - 4788 | 1.00 | |
| | | $\beta_{abs}$ | 0.63 | - 1527 | 1.00 | |
| MJT/Q014 | Biomass on Diesel 21:79 | ATN | 0.78 | - 0.53 | 1.00 | 453 |
| | | $\beta_{ATN}$ | 0.87 | - 10819 | 1.00 | |
| | | $\beta_{abs}$ | 0.85 | -8256 | 1.00 | |
| MJT/Q015 | Biomass on Diesel 13:87 | ATN | 0.72 | -0.41 | 1.00 | 300 |
| | | $\beta_{ATN}$ | 0.81 | -6852 | 1.00 | |
| | | $\beta_{abs}$ | 88.5 | -3770602 | 0.99 | |
| MJT/Q018 | Diesel on Biomass 8:92 | ATN | 0.33 | 0.12 | 1.00 | 553 |
| | | $\beta_{ATN}$ | 0.37 | 4328 | 1.00 | |
| | | $\beta_{abs}$ | 0.37 | 9481 | 1.00 | |
| MJT/Q019 | Diesel on Biomass 32:68 | ATN | 0.40 | 0.22 | 0.98 | 94 |
| | | $\beta_{ATN}$ | 0.45 | 3374 | 0.98 | |
| | | $\beta_{abs}$ | 0.43 | 4693 | 0.98 | |

[a] Intercept units for $\beta_{ATN}$ and $\beta_{abs}$ are $Mm^{-1}$; ATN is unitless.

[b] No $\beta_{abs}$ values for red dust QF samples.

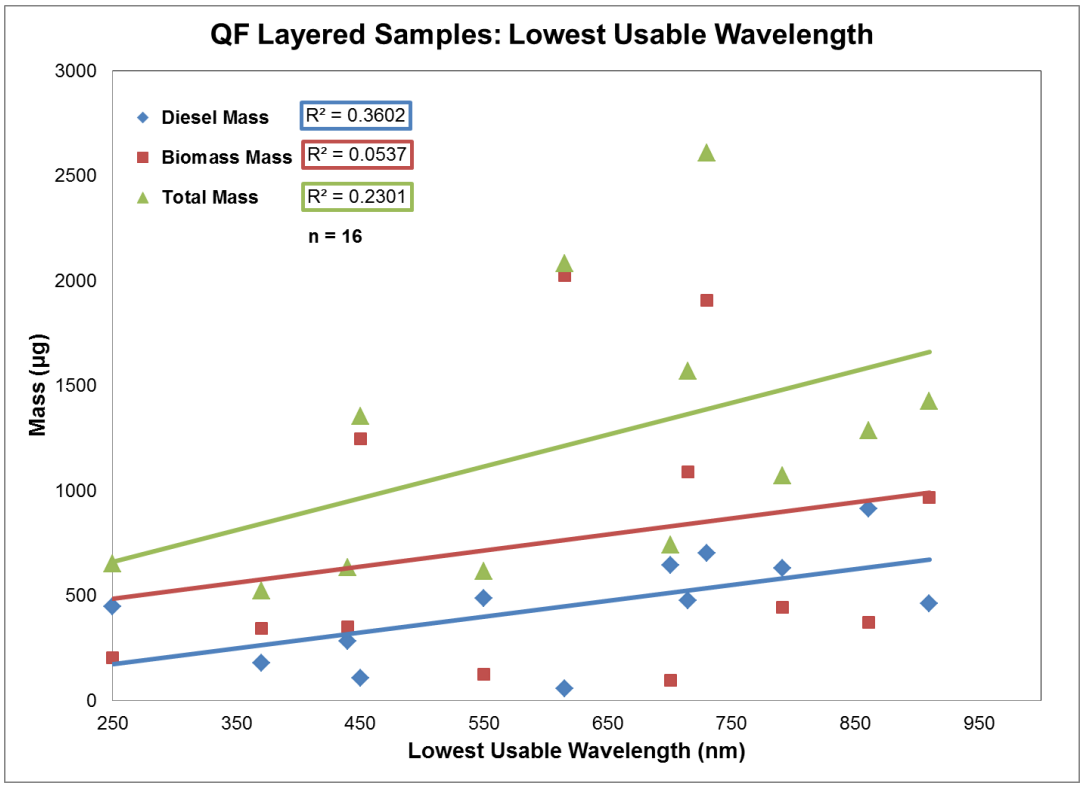


**Figure 3-17.** Relationships between lowest usable wavelength (ATN < 5) and mass loadings on QF layered samples.

For the layered QF samples no correlations were found with mass loadings, with $R^2$ ranging from 0.05 (biomass) to 0.36 (diesel). Table 3-7 details the layered sample mass loadings and lowest usable wavelengths. Four QF layered samples (i.e. MJQ004, 006, 009 and 010) had attenuation values greater than 5 for all wavelengths (listed as NaN), and three of these samples had the highest diesel mass loadings. Only four of these layered samples were analyzed using thermal/optical carbon analysis so the breakdown could not be further analyzed by OC, EC and TC loadings.

**Table 3-7.** Layered Sample Lowest Usable Wavelengths and Mass Loadings

| Filter ID | Lowest Usable Wavelength (nm) [a] | Biomass Mass (µg) | Diesel Mass (µg) | Total Mass (µg) | % Biomass | % Diesel |
|---|---|---|---|---|---|---|
| MJQ002 | 615 | 2025 | 58 | 2083 | 97 | 3 |
| MJQ003 | 861 | 371 | 915 | 1287 | 29 | 71 |
| MJQ004 | NaN | 647 | 661 | 1308 | 49 | 51 |
| MJQ005 | 715 | 1090 | 478 | 1569 | 70 | 30 |
| MJQ006 | NaN | 134 | 2463 | 2597 | 5 | 95 |
| MJQ008 | 730 | 1908 | 701 | 2609 | 73 | 27 |
| MJQ009 | NaN | 1632 | 1480 | 3112 | 52 | 48 |
| MJQ010 | NaN | 696 | 2286 | 2982 | 23 | 77 |
| MJQ012 | 370 | 345 | 178 | 523 | 66 | 34 |
| MJQ013 | 440 | 350 | 284 | 634 | 55 | 45 |
| MJQ014 | 550 | 127 | 488 | 615 | 21 | 79 |
| MJQ015 | 701 | 96 | 646 | 742 | 13 | 87 |
| MJQ016 | 791 | 442 | 630 | 1072 | 41 | 59 |
| MJQ017 | 250 | 202 | 448 | 650 | 31 | 69 |
| MJQ018 | 450 | 1248 | 106 | 1354 | 92 | 8 |
| MJQ019 | 910 | 966 | 461 | 1427 | 68 | 32 |

[a]NaN entries indicate that all attenuation values were greater than 5 (i.e. there is no lowest usable wavelength).

Most of the QF source samples that had attenuation values greater than five were not weighed but were examined by thermal/optical carbon analysis so the lowest usable wavelengths were compared to TC, OC and EC loadings. All sample carbon loadings and shortest usable wavelengths are detailed in Table 3-8.

For the OC dominated samples of peat and pine cone, Figure 3-18 shows that the lowest usable wavelength is most dependent on the TC (or OC) loading, which ultimately corresponds to the mass loading. Sample loading needs to be high (>300 µg/filter) for the attenuation to exceed 5 at longer wavelengths.

For the pine needle samples, which have higher EC/TC ratios than the peat and pine cone samples but are still generally OC dominated, the lowest usable wavelength is

most dependent on the TC loading and least dependent on the EC loading. When the TC exceeds ~40 μg/filter, however, the wavelength seems to be equally dependent on each carbon loading fraction. The relationship seems to depend most on the TC loading though because there are other samples with: 1) similar EC/TC ratios but lower TC or 2) similar EC loadings but lower TC that do not have attenuation values greater than 5 at longer wavelengths.

For the diesel samples, which are EC dominated, the lowest usable wavelength is most dependent on the TC loading and closely followed by the EC loading. As was noted for the pine needle samples, longer wavelengths aren't affected until the TC loading is above 40 μg/filter.

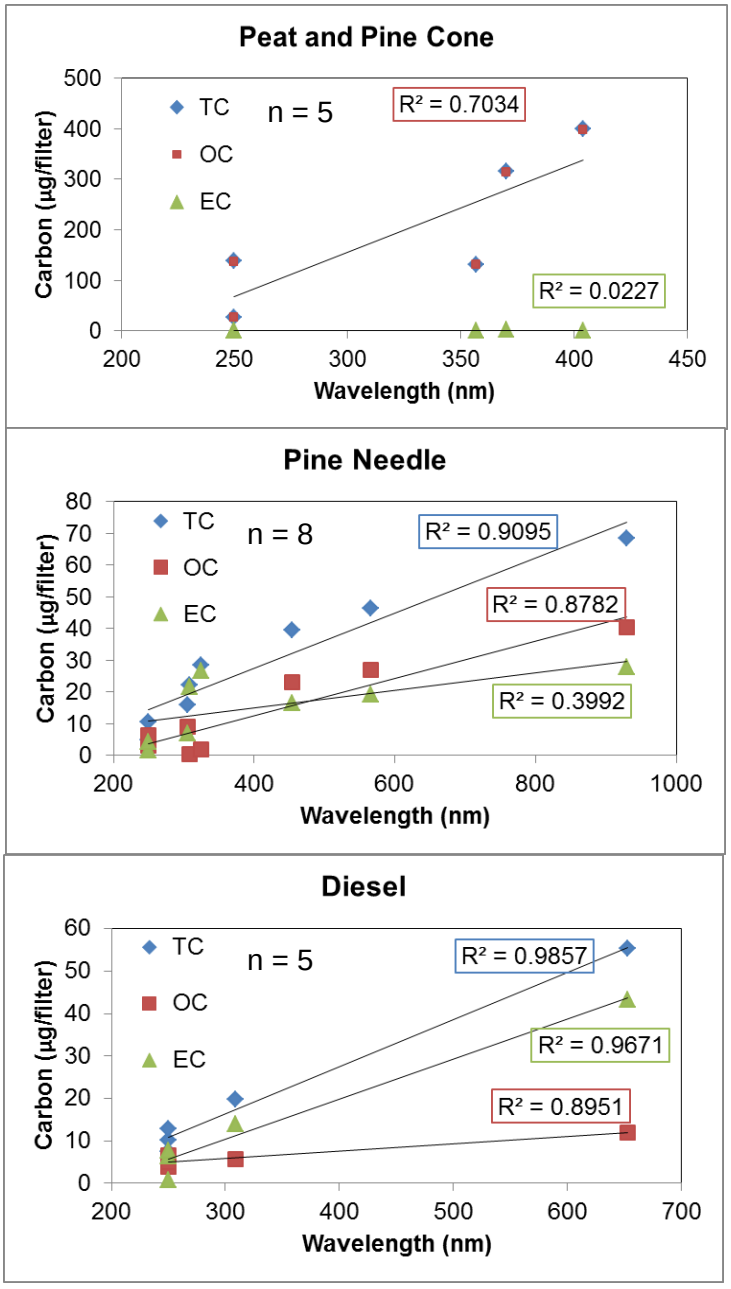


**Figure 3-18.** Relationships between lowest usable wavelength (ATN< 5) and carbon loadings using thermal/optical analysis on QF source samples. For all samples the best correlation is seen with TC loading, though for the attenuation to be large at higher wavelengths the loading needs to be much greater for OC-dominated samples (e.g. smoldering peat and pine cone) than for EC-dominated (e.g. flaming pine needle and diesel exhaust).

**Table 3-8.** QF Source Sample Lowest Usable Wavelength and Carbon Loadings

| Sample ID | Source Type | Lowest Usable Wavelength (nm) | TC[a] | OC[a] | EC[a] | EC/TC |
|---|---|---|---|---|---|---|
| NCAQ042 | Peat | 250 | 139.01 | 137.41 | 1.6 | 0.01 |
| NCAQ072 | Peat | 250 | 27.3 | 26.87 | 0.43 | 0.02 |
| NCAQ077 | Peat | 357 | 131.95 | 130.81 | 1.14 | 0.01 |
| NCAQ079 | Peat | 370 | 316.31 | 314.42 | 1.89 | 0.01 |
| NCAQ053 | Pine Cone | 404 | 399.06 | 398.26 | 0.8 | 0 |
| NCAQ080 | Pine Needle | 250 | 4.87 | 3.2 | 1.67 | 0.34 |
| NCAQ081 | Pine Needle | 250 | 10.58 | 6.33 | 4.25 | 0.4 |
| NCAQ082 | Pine Needle | 306 | 16.06 | 8.96 | 7.1 | 0.44 |
| NCAQ083 | Pine Needle | 308 | 22.2 | 0.49 | 21.71 | 0.98 |
| NCAQ084 | Pine Needle | 324 | 28.38 | 1.77 | 26.61 | 0.94 |
| NCAQ085 | Pine Needle | 454 | 39.43 | 22.97 | 16.46 | 0.42 |
| NCAQ086 | Pine Needle | 566 | 46.35 | 27.06 | 19.29 | 0.42 |
| NCAQ087 | Pine Needle | 929 | 68.33 | 40.41 | 27.93 | 0.41 |
| NCAQ091 | Diesel | 250 | 10.24 | 3.86 | 6.38 | 0.62 |
| NCAQ092 | Diesel | 250 | 12.8 | 5.1 | 7.7 | 0.6 |
| NCAQ093 | Diesel | 309 | 19.78 | 5.78 | 14 | 0.71 |
| NCAQ094 | Diesel | 250 | 7.37 | 6.68 | 0.69 | 0.09 |
| NCAQ095 | Diesel | 653 | 55.29 | 11.99 | 43.3 | 0.78 |

[a] Carbon fractions listed in units of μg/filter

### 3.2.3 Ambient Samples

The ambient samples also display similar relationships between TM and QF attenuation (ATN), $\beta_{ATN}$ and $\beta_{abs}$, as summarized in Table 3-9. Figures 3-19 to 3-21 show linear relationships between the $\beta_{ATN}$ from the TM and QF filter samples for the Port of LA, Rim Fire and TCEQ Clinton, respectively. High correlations ($R^2$ of 0.98 – 1) are found for all ambient samples with some deviations at the low and high ends of the sample $\beta_{ATN}$ spectrum.

Average TM ATN values are 34% of the QF for the Port of LA, 32% for Rim Fire, and 37% for TCEQ Clinton St. site, respectively. Average TM $\beta_{ATN}$ and $\beta_{abs}$ values are 38 and 47% of the QF values for the Port of LA, 36 and 44% for Rim Fire, and 41% ($\beta_{ATN}$ only) for TCEQ Clinton St. samples, respectively. All of the ambient samples have low average intercept values, but the average TCEQ intercept values are the lowest at 0.02 (ATN, unitless) and 0 ($\beta_{ATN}$, $Mm^{-1}$).

**Table 3-9.** Ambient Sample TM & QF Linear Relationship Slopes and Intercepts

| Sample Pair | Ambient Sample | TM vs. QF Slope | | Intercept[a] | $R^{2}$ [b] |
|---|---|---|---|---|---|
| 1 | Port of LA | ATN | 0.43 | 0.17 | 0.99 |
| | | $\beta_{ATN}$ | 0.48 | 5.79 | 0.99 |
| | | $\beta_{abs}$ | 0.59 | 5.04 | 0.99 |
| 2 | Port of LA | ATN | 0.3 | 0.09 | 0.99 |
| | | $\beta_{ATN}$ | 0.34 | 3.09 | 0.99 |
| | | $\beta_{abs}$ | 0.41 | 4.68 | 0.98 |
| 3 | Port of LA | ATN | 0.32 | 0.17 | 0.99 |
| | | $\beta_{ATN}$ | 0.36 | 6.2 | 0.99 |
| | | $\beta_{abs}$ | 0.43 | 7.35 | 0.99 |
| 4 | Port of LA | ATN | 0.39 | 0.26 | 0.99 |
| | | $\beta_{ATN}$ | 0.43 | 9.81 | 0.99 |
| | | $\beta_{abs}$ | 0.5 | 9.17 | 0.99 |
| 5 | Port of LA | ATN | 0.27 | 0.23 | 0.97 |
| | | $\beta_{ATN}$ | 0.3 | 8.62 | 0.97 |
| | | $\beta_{abs}$ | 0.4 | 7.4 | 0.96 |
| 1 | Rim Fire | ATN | 0.92 | -0.89 | 0.96 |
| | | $\beta_{ATN}$ | 1.03 | -36.77 | 0.96 |
| | | $\beta_{abs}$ | 0.87 | -9.67 | 0.98 |
| 2 | Rim Fire | ATN | 0.28 | 0.13 | 0.98 |
| | | $\beta_{ATN}$ | 0.32 | 5.38 | 0.98 |
| | | $\beta_{abs}$ | 0.41 | -0.31 | 0.98 |
| 3 | Rim Fire | ATN | 0.31 | 0.07 | 0.98 |
| | | $\beta_{ATN}$ | 0.34 | 2.95 | 0.98 |
| | | $\beta_{abs}$ | 0.4 | -0.09 | 0.98 |

| | | | | | |
|---|---|---|---|---|---|
| 4 | Rim Fire | ATN | 0.41 | 0.04 | 0.98 |
| | | $\beta_{ATN}$ | 0.46 | 1.74 | 0.98 |
| | | $\beta_{abs}$ | 0.55 | 0.94 | 0.99 |
| 5 | Rim Fire | ATN | 0.18 | -0.03 | 0.98 |
| | | $\beta_{ATN}$ | 0.21 | -1.32 | 0.98 |
| | | $\beta_{abs}$ | 0.34 | -2.04 | 0.99 |
| 6 | Rim Fire | ATN | 0.18 | -0.02 | 0.98 |
| | | $\beta_{ATN}$ | 0.2 | -0.92 | 0.98 |
| | | $\beta_{abs}$ | 0.32 | -0.34 | 0.98 |
| 7 | Rim Fire | ATN | 0.14 | -0.02 | 0.89 |
| | | $\beta_{ATN}$ | 0.16 | -0.72 | 0.89 |
| | | $\beta_{abs}$ | 0.33 | 0.6 | 0.91 |
| 8 | Rim Fire | ATN | 0.24 | -0.04 | 0.96 |
| | | $\beta_{ATN}$ | 0.27 | -1.49 | 0.96 |
| | | $\beta_{abs}$ | 0.41 | 0.32 | 0.96 |
| 3 | TCEQ Clinton | ATN | 0.27 | 0.22 | 0.93 |
| | | $\beta_{ATN}$ | 0.3 | 0 | 0.93 |
| 4 | TCEQ Clinton | ATN | 0.29 | 0.04 | 0.99 |
| | | $\beta_{ATN}$ | 0.32 | 0 | 0.99 |
| 5 | TCEQ Clinton | ATN | 0.3 | -0.01 | 0.99 |
| | | $\beta_{ATN}$ | 0.34 | 0 | 0.99 |
| 6 | TCEQ Clinton | ATN | 0.31 | 0 | 1.00 |
| | | $\beta_{ATN}$ | 0.34 | 0 | 1.00 |
| 8 | TCEQ Clinton | ATN | 0.46 | -0.09 | 1.00 |
| | | $\beta_{ATN}$ | 0.52 | 0 | 1.00 |
| 9 | TCEQ Clinton | ATN | 0.4 | 0.06 | 1.00 |
| | | $\beta_{ATN}$ | 0.45 | 0 | 1.00 |
| 10 | TCEQ Clinton | ATN | 0.56 | -0.08 | 1.00 |
| | | $\beta_{ATN}$ | 0.62 | 0 | 1.00 |
| 11 | TCEQ Clinton | ATN | 0.36 | 0.03 | 1.00 |
| | | $\beta_{ATN}$ | 0.4 | 0 | 1.00 |
| 12 | TCEQ Clinton | ATN | 0.38 | -0.05 | 1.00 |
| | | $\beta_{ATN}$ | 0.42 | 0 | 1.00 |
| 13 | TCEQ Clinton | ATN | 0.35 | 0.08 | 1.00 |
| | | $\beta_{ATN}$ | 0.39 | 0 | 1.00 |

[a] Intercept units for $\beta_{ATN}$ and $\beta_{abs}$ are $Mm^{-1}$; ATN is unitless.

[b] n = 751 for all samples (no ATN >5)

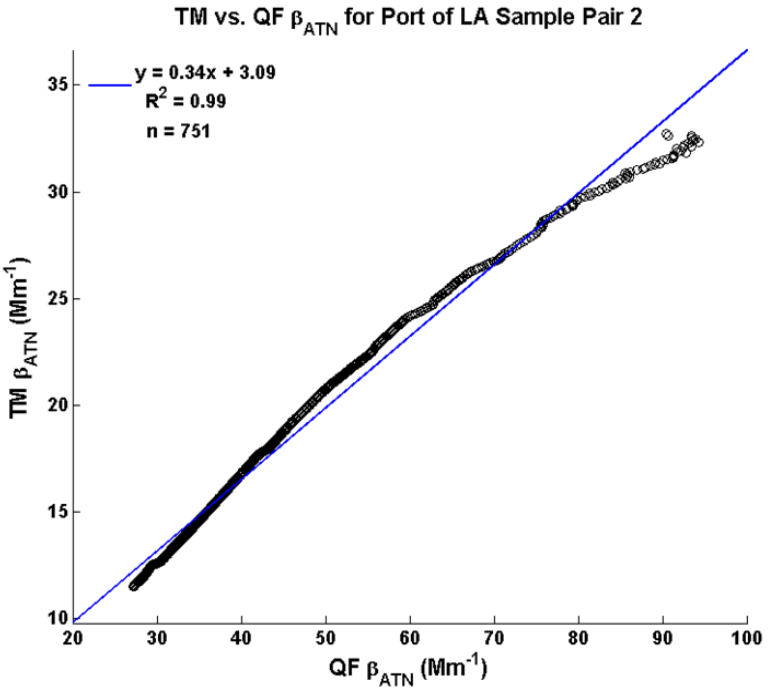


**Figure 3-19.** QF and TM comparison of $\beta_{ATN}$ values for a pair of Port of LA filters. The average slope for the Port of LA filters is 0.38.

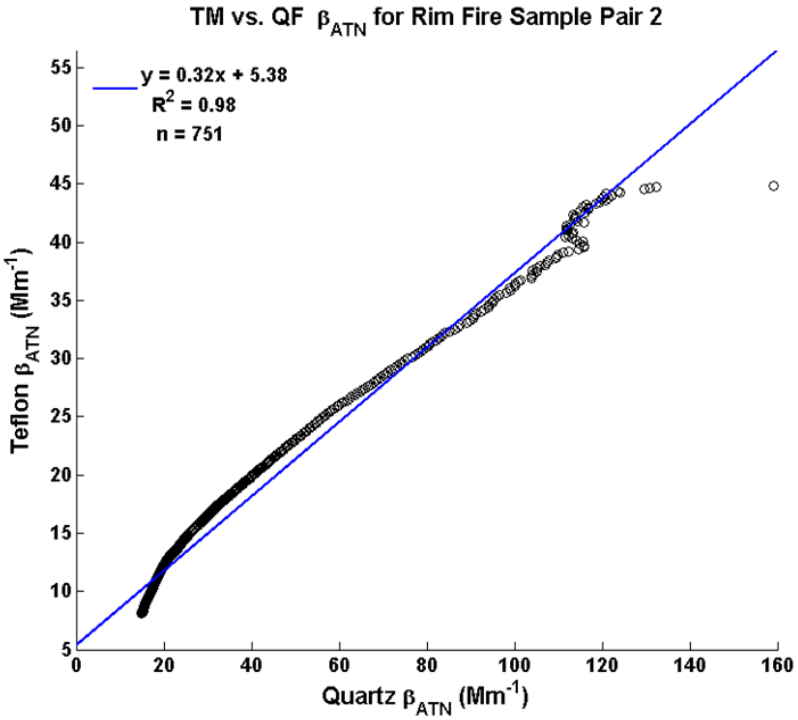


**Figure 3-20.** QF and TM comparison of $\beta_{ATN}$ values for a pair of Rim Fire filters. The average slope for the Rim Fire filters is 0.36.

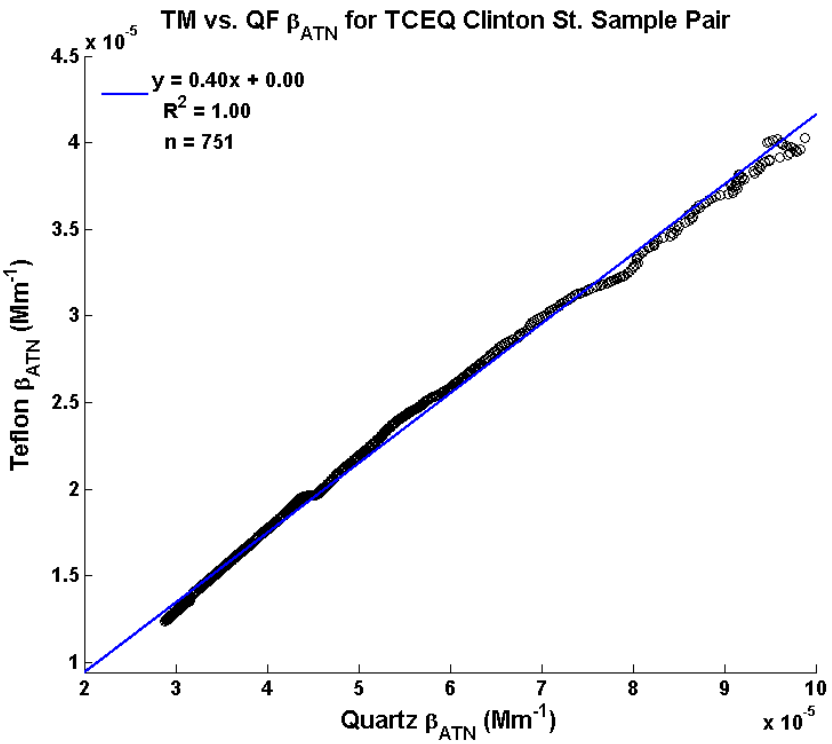


**Figure 3-19.** QF and TM comparison of $\beta_{ATN}$ values for a pair of TCEQ Clinton filters. The average slope for the TCEQ Clinton filters is 0.41.

## 3.3 Absorption Ångström Exponents (AAEs)

AAEs were calculated for all samples using attenuation and $\beta_{abs}$ values. The attenuation and $\beta_{abs}$ curves were fitted 1) across the entire spectrum and 2) for points at eight wavelengths (e.g. 370, 405, 445, 532, 635, 780, 808, and 980 nm, used in DRI Model 2015 thermal/optical carbon analyzer) with a power law approximation. Using Equation 10 in Section 1.2, the AAEs were calculated for four wavelength pairs: 250 & 1000 nm (Lambda 35 scan range), 350 & 1000 nm (beginning of solar radiation reaching Earth's surface), 370 & 880 nm (wavelengths used by the Magee Transmissometer), and 400 & 700 nm (visible range). These values are tabulated and are compared to sample EC concentration $\left(\frac{\mu g}{m^3}\right)$.

### 3.3.1 Source Samples

Tables 3-10 and 3-11 list the AAE values calculated for the source samples using $\beta_{abs}$ and $\beta_{ATN}$, respectively. High AAEs (2.1 -5.1) are found for high-moisture biomass burning samples (leaves, duff, and litter), pine cone burning (4.1 – 4.7), and peat burning (4.1 – 4.8), indicative of smoldering aerosol. The values obtained for these samples are consistent with many reported in literature (Foot and Kilsby 1989, Lindberg et al., 1993, Dubovik et al., 1998, Kirchstetter et al., 2004a, Clarke et al., 2007, Russell et al., 2010, Kirchstetter and Thatcher 2012), though several BC dominated samples (e.g. acetylene flame, some laboratory-generated diesel) have AAE values of less than one (0.67 – 0.73). The QF AAEs are 32 to 198% larger than those for TM, on average, and the standard deviation among the QF AAE values is generally higher than that for TM. This is also

seen in the comparison of the concurrent QF and TM biomass burning samples (sample ID: DBI). The AAEs of both the QF and TM DBI biomass burning samples are lower than those found using PAS data (see Table 3-12), which is to be expected given the increased difference between QF, TM and PAS $\beta_{abs}$ values with increasing wavelength. AAEs calculated using $\beta_{abs}$ tend to be larger than those calculated using $\beta_{ATN}$ except for samples with high EC concentrations, which gives similar AAEs.

Table 3-13 summarizes the carbon content (TC, OC, and EC) of individual samples and their corresponding average $\beta_{abs}$ AAE values. There is generally the least amount of deviation between the AAE values for samples with higher amounts of EC. Colorful dusts (e.g. red soil, taconite) and smoldering biomass burning samples have the highest standard deviations (up to 1.18 for the smoldering pine cone sample) as they are not well represented by the power law curve fit. The power law fit tends to underestimate the rapid increase in absorption with decreasing wavelength for samples containing BrC, and the irregular curves produced by colorful dusts are difficult to approximate. For these samples, the largest AAE values are those calculated using the visible wavelength pair, 400 & 700 nm.

Plotting the source sample AAE values against sample EC fraction in Figure 3-22 reinforces an observation similar to the one made previously – the lower the sample EC/TC, the more variable the AAE values.

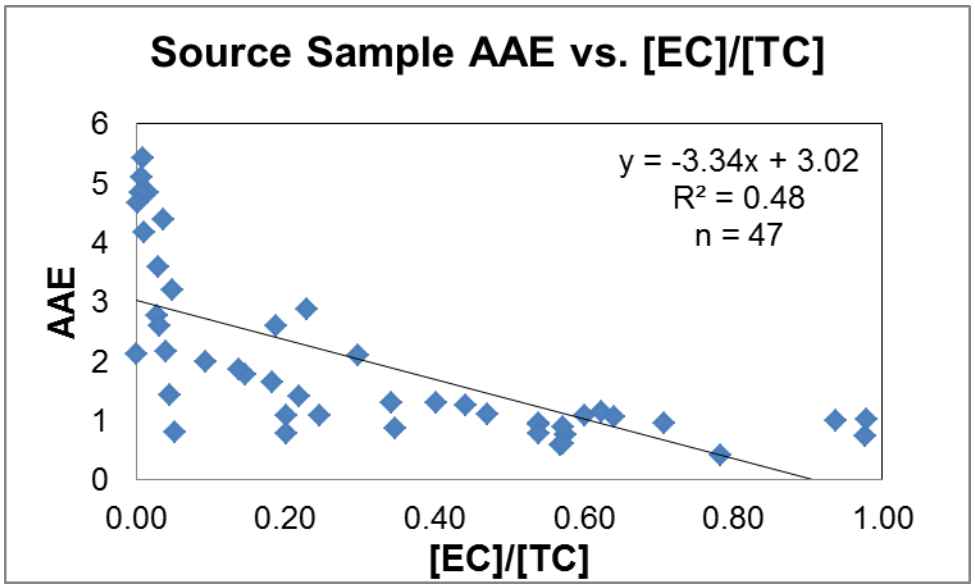


**Figure 3-20.** Source sample average AAE values plotted as a function of the fraction of EC in TC for each samples. EC and TC were determined using the DRI Model 2001 Carbon Analyzer for thermal/optical carbon analysis following IMRPOVE_A thermal/optical reflectance protocol (Chow et al., 2007). This figure includes data points from four layered samples.

**Table 3-10.** Source Sample AAE Values from $\boldsymbol{\beta_{abs}}$[a]

| Source Type | Sample ID | AAE λs (nm) | | | | | | Avg | Std Dev |
|---|---|---|---|---|---|---|---|---|---|
| | | All | 8 -λ | 250 & 1000 | 350 & 1000 | 370 & 880 | 400 & 700 | | |
| Bitterbrush Stems | BIOTKF072 | 1.09 | 1.09 | 1.04 | 1.10 | 1.10 | 1.08 | 1.08 | 0.02 |
| 50% wet leaves | BIOTKF086 | 1.43 | 2.93 | 2.84 | 2.82 | 3.04 | 3.52 | 2.77 | 0.70 |
| 100% wet duff | BIOTKF088 | 3.08 | 5.75 | 4.24 | 5.02 | 5.80 | 6.71 | 5.10 | 1.29 |
| 100% wet litter | BIOTKF102 | 1.43 | 1.35 | 1.32 | 1.41 | 1.45 | 1.55 | 1.42 | 0.08 |
| Smoldering Pine Needle | DBIT001 | 1.63 | 1.59 | 1.46 | 1.65 | 1.69 | 1.81 | 1.49 | 0.12 |
| | DBIT002 | 1.75 | 1.74 | 1.54 | 1.77 | 1.84 | 2.03 | | 0.16 |
| | DBIT003 | 1.07 | 1.01 | 1.00 | 1.09 | 1.08 | 1.07 | | 0.04 |
| | DBIQ001 | 2.12 | 2.19 | 1.48 | 2.27 | 2.35 | 2.60 | 2.20 | 0.38 |
| | DBIQ002 | 2.75 | 2.33 | 2.39 | 2.71 | 2.54 | 2.78 | | 0.19 |
| | DBIQ003 | 2.13 | 1.60 | 1.98 | 1.91 | 1.78 | 1.73 | | 0.19 |
| Cheat Grass | DBIT005 | 2.06 | 2.14 | 1.87 | 2.16 | 2.17 | 2.18 | 2.52 | 0.12 |
| | DBIT006 | 2.49 | 2.75 | 2.06 | 2.55 | 2.74 | 3.03 | | 0.33 |
| | DBIT007 | 2.77 | 2.99 | 2.36 | 2.86 | 3.00 | 3.22 | | 0.29 |
| | DBIQ005 | 3.39 | 3.00 | 3.15 | 3.12 | 3.17 | 3.29 | 3.72 | 0.14 |
| | DBIQ006 | 3.33 | 3.90 | 2.44 | 3.64 | 3.86 | 4.40 | | 0.67 |
| | DBIQ007 | 4.77 | 4.04 | 4.93 | 3.95 | 4.11 | 4.55 | | 0.42 |
| Peat | NCAQ042 | 3.86 | 4.40 | 2.80 | 4.00 | 4.50 | 5.46 | 4.82 | 0.88 |
| | NCAQ072 | 4.76 | 4.89 | 3.89 | 4.76 | 5.15 | 5.58 | | 0.56 |
| | NCAQ077 | 5.07 | 5.72 | 4.56 | 5.37 | 5.75 | 6.06 | | 0.54 |
| | NCAQ079 | 4.40 | 5.48 | 3.35 | 4.90 | 5.30 | 5.58 | | 0.85 |
| Flaming Pine Needle | NCAQ080 | 1.36 | 1.23 | 1.39 | 1.31 | 1.28 | 1.24 | 1.17 | 0.06 |
| | NCAQ081 | 1.40 | 1.21 | 1.40 | 1.30 | 1.26 | 1.20 | | 0.09 |
| | NCAQ082 | 1.58 | 1.15 | 1.26 | 1.24 | 1.19 | 1.13 | | 0.17 |
| | NCAQ083 | 1.07 | 1.01 | 0.94 | 1.06 | 1.02 | 0.97 | | 0.05 |
| | NCAQ084 | 1.08 | 0.99 | 0.89 | 1.03 | 0.97 | 0.94 | | 0.07 |
| Pine Cone | NCAQ053 | 4.36 | 5.17 | 2.93 | 4.13 | 4.90 | 6.47 | 4.66 | 1.18 |
| Flaming Wood | STRST133 | 1.38 | 1.45 | 1.26 | 1.42 | 1.46 | 1.45 | 1.25 | 0.07 |
| | STRST136 | 1.08 | 1.14 | 1.04 | 1.16 | 1.13 | 1.08 | | 0.05 |
| Paved Parking Lot Dust | REST339 | 0.90 | 0.82 | 0.95 | 0.86 | 0.84 | 0.85 | 0.87 | 0.05 |
| Paved Road Dust | REST1856 | 1.56 | 1.45 | 1.53 | 1.42 | 1.51 | 1.66 | 1.52 | 0.08 |
| Taconite | REST2015 | 0.71 | 0.90 | 0.74 | 0.93 | 0.64 | 0.79 | 0.79 | 0.11 |
| De-icing Material | REST2102 | 2.16 | 2.00 | 2.04 | 1.94 | 2.09 | 2.42 | 2.11 | 0.17 |
| Red Dust | REST2183 | 2.26 | 2.32 | 1.82 | 1.78 | 2.36 | 3.11 | 2.69 | 0.48 |
| | REST2184 | 2.05 | 2.25 | 1.73 | 1.97 | 2.18 | 2.51 | | 0.27 |
| | REST2185 | 3.50 | 3.97 | 3.61 | 4.28 | 3.32 | 3.39 | | 0.37 |
| | REST2186 | 2.60 | 2.87 | 2.47 | 2.91 | 2.53 | 2.68 | | 0.18 |
| Diesel | STRST061 | 0.73 | 0.83 | 0.64 | 0.81 | 0.80 | 0.76 | 0.67 | 0.07 |
| | STRST064 | 0.57 | 0.65 | 0.53 | 0.64 | 0.62 | 0.54 | | 0.05 |
| | NCAQ091 | 1.15 | 1.17 | 0.98 | 1.18 | 1.18 | 1.22 | 1.12 | 0.08 |
| | NCAQ092 | 1.05 | 1.11 | 1.00 | 1.10 | 1.12 | 1.14 | | 0.05 |
| | NCAQ093 | 0.90 | 1.04 | 0.65 | 1.01 | 1.03 | 1.07 | | 0.16 |
| | NCAQ094 | 2.03 | 1.93 | 1.96 | 2.01 | 1.97 | 1.98 | | 0.04 |
| | NCAQ095 | 0.27 | 0.61 | 0.06 | 0.45 | 0.43 | 0.67 | | 0.22 |
| Acetylene | STRST111 | 0.72 | 0.77 | 0.59 | 0.75 | 0.76 | 0.78 | 0.73 | 0.07 |

[a] See Equation 10 in Section 1.2 for AAE calculation and Equation 22 in Section 2.2.3. AAEs under "All" and "8-λ" were found using a power law curve fit. Average AAEs made for groups of source type (by filter type) but standard deviation shown is for each filter sample.

**Table 3-11.** Source Sample AAE Values from $\boldsymbol{\beta_{ATN}}$[a]

| Source Type | Sample ID | AAE λs (nm) | | | | | | Avg | Std Dev |
|---|---|---|---|---|---|---|---|---|---|
| | | All | 8 -λ | 250 & 1000 | 350 & 1000 | 370 & 880 | 400 & 700 | | |
| Bitterbrush Stems | BIOTKF072 | 1.05 | 1.04 | 1.01 | 1.06 | 1.05 | 1.04 | 1.04 | 0.02 |
| 50% wet leaves | BIOTKF086 | 2.35 | 2.10 | 2.32 | 2.14 | 2.24 | 2.51 | 2.28 | 0.15 |
| 100% wet duff | BIOTKF088 | 1.82 | 1.58 | 1.69 | 1.73 | 1.81 | 2.03 | 1.78 | 0.15 |
| 100% wet litter | BIOTKF102 | 1.16 | 1.05 | 1.10 | 1.13 | 1.15 | 1.22 | 1.14 | 0.06 |
| Smoldering Pine Needle | DBIT001 | 1.20 | 1.12 | 1.10 | 1.20 | 1.22 | 1.29 | 1.10 | 0.07 |
| | DBIT002 | 1.25 | 1.19 | 1.14 | 1.26 | 1.29 | 1.40 | | 0.09 |
| | DBIT003 | 0.86 | 0.80 | 0.83 | 0.88 | 0.86 | 0.84 | | 0.03 |
| | DBIQ001 | 1.49 | 1.54 | 0.93 | 1.62 | 1.67 | 1.83 | 1.74 | 0.31 |
| | DBIQ002 | 2.29 | 1.85 | 2.01 | 2.25 | 2.04 | 2.18 | | 0.17 |
| | DBIQ003 | 1.87 | 1.36 | 1.74 | 1.66 | 1.52 | 1.45 | | 0.19 |
| Cheat Grass | DBIT005 | 1.36 | 1.35 | 1.27 | 1.40 | 1.40 | 1.40 | 1.53 | 0.05 |
| | DBIT006 | 1.74 | 1.83 | 1.44 | 1.74 | 1.89 | 2.16 | | 0.24 |
| | DBIT007 | 1.42 | 1.41 | 1.24 | 1.40 | 1.49 | 1.66 | | 0.14 |
| | DBIQ005 | 2.70 | 2.32 | 2.51 | 2.38 | 2.45 | 2.59 | 2.63 | 0.14 |
| | DBIQ006 | 2.30 | 2.73 | 1.56 | 2.53 | 2.72 | 3.18 | | 0.54 |
| | DBIQ007 | 2.96 | 2.94 | 2.18 | 2.85 | 3.02 | 3.43 | | 0.41 |
| Peat | NCAQ042 | 3.56 | 4.18 | 2.51 | 3.68 | 4.20 | 5.02 | 4.13 | 0.84 |
| | NCAQ072 | 4.56 | 4.92 | 3.78 | 4.79 | 5.05 | 5.20 | | 0.51 |
| | NCAQ077 | 4.02 | 4.09 | 3.27 | 3.72 | 4.11 | 4.60 | | 0.44 |
| | NCAQ079 | 4.47 | 4.34 | 2.48 | 3.75 | 4.23 | 4.56 | | 0.78 |
| Flaming Pine Needle | NCAQ080 | 1.56 | 1.42 | 1.56 | 1.52 | 1.48 | 1.42 | 1.17 | 0.06 |
| | NCAQ081 | 1.48 | 1.30 | 1.48 | 1.41 | 1.35 | 1.26 | | 0.09 |
| | NCAQ082 | 1.23 | 1.12 | 1.23 | 1.23 | 1.16 | 1.08 | | 0.06 |
| | NCAQ083 | 0.95 | 0.92 | 0.85 | 0.96 | 0.92 | 0.86 | | 0.04 |
| | NCAQ084 | 0.91 | 0.89 | 0.80 | 0.92 | 0.86 | 0.83 | | 0.05 |
| Pine Cone | NCAQ053 | 4.44 | 4.50 | 2.49 | 3.57 | 4.26 | 5.54 | 4.13 | 1.02 |
| Flaming Wood | STRST133 | 1.09 | 1.12 | 1.01 | 1.10 | 1.13 | 1.14 | 1.01 | 0.05 |
| | STRST136 | 0.91 | 0.94 | 0.90 | 0.96 | 0.94 | 0.90 | | 0.03 |
| Paved Parking Lot Dust | REST339 | 0.61 | 0.56 | 0.65 | 0.59 | 0.57 | 0.55 | 0.59 | 0.04 |
| Paved Road Dust | REST1856 | 0.74 | 0.63 | 0.79 | 0.65 | 0.67 | 0.72 | 0.70 | 0.06 |
| Taconite | REST2015 | 0.44 | 0.53 | 0.45 | 0.53 | 0.40 | 0.49 | 0.47 | 0.05 |
| De-icing Material | REST2102 | 1.26 | 1.08 | 1.30 | 1.15 | 1.16 | 1.22 | 1.20 | 0.08 |
| Red Dust | REST2183 | 0.90 | 0.83 | 0.87 | 0.74 | 0.87 | 1.06 | 1.03 | 0.10 |
| | REST2184 | 0.98 | 1.02 | 0.87 | 0.90 | 1.02 | 1.24 | | 0.13 |
| | REST2185 | 1.08 | 1.10 | 1.04 | 1.04 | 1.07 | 1.22 | | 0.07 |
| | REST2186 | 1.16 | 1.18 | 1.10 | 1.11 | 1.13 | 1.31 | | 0.08 |
| Red Dust | RESQ2193 | 2.44 | 2.71 | 1.71 | 2.50 | 2.84 | 3.52 | 2.35 | 0.59 |
| | RESQ2194 | 1.46 | 1.72 | 1.10 | 1.51 | 1.71 | 2.09 | | 0.33 |
| | RESQ2195 | 2.47 | 2.52 | 1.98 | 2.00 | 2.55 | 3.25 | | 0.47 |
| | RESQ2196 | 2.47 | 2.99 | 1.87 | 2.86 | 2.87 | 3.20 | | 0.47 |
| Diesel | STRST061 | 0.74 | 0.84 | 0.65 | 0.82 | 0.81 | 0.76 | 0.68 | 0.07 |
| | STRST064 | 0.58 | 0.66 | 0.53 | 0.65 | 0.62 | 0.54 | | 0.05 |
| | NCAQ091 | 1.06 | 1.08 | 0.90 | 1.10 | 1.10 | 1.11 | 1.07 | 0.08 |
| | NCAQ092 | 0.97 | 1.02 | 0.93 | 1.03 | 1.03 | 1.04 | | 0.05 |
| | NCAQ093 | 0.92 | 0.96 | 0.58 | 0.93 | 0.95 | 0.99 | | 0.15 |
| | NCAQ094 | 1.87 | 1.80 | 1.76 | 1.89 | 1.84 | 1.82 | | 0.05 |
| | NCAQ095 | 0.92 | 0.92 | 0.05 | 0.43 | 0.42 | 0.66 | | 0.34 |
| Acetylene | STRST111 | 0.73 | 0.78 | 0.59 | 0.76 | 0.76 | 0.78 | 0.73 | 0.07 |

[a] See Equation 10 in Section 1.2 for AAE calculation and Equation 17 in Section 2.2.2 for $\beta_{ATN}$. AAEs under "All" and "8-λ" were found using a power law curve fit.

**Table 3-12.** Collocated Smoldering Biomass Sample AAEs from QF, TM and PAS

| Source Type | Curve Fit 3-λ (405, 532, 781 nm) | | | 405 and 781 nm λ Pair | | | Std Dev.[a] |
|---|---|---|---|---|---|---|---|
| | QF | TM | PAS | QF | TM | PAS | |
| Pine Needles | 2.30 | 1.64 | 3.10 | 2.35 | 1.67 | 3.18 | 0.76 |
| Pine Needles | 2.42 | 1.83 | 3.74 | 2.48 | 1.86 | 3.85 | 1.02 |
| Pine Needles | 1.57 | 1.01 | 2.26 | 1.6 | 1.02 | 2.31 | 0.65 |
| Cheat Grass | 3.06 | 2.13 | 3.49 | 3.1 | 2.13 | 3.53 | 0.72 |
| Cheat Grass | 4.14 | 2.90 | 4.80 | 4.18 | 2.92 | 4.87 | 0.99 |
| Cheat Grass | 4.22 | 3.10 | 4.55 | 4.27 | 3.12 | 4.62 | 0.79 |

[a] Standard deviation of all AAEs (i.e. QF, TM and PAS) listed for a sample.

**Table 3-13.** Source and Layered Sample Carbon Fractions and Average AAE Values

| Sample ID | Source Type | TC[a] | OC[a] | EC[a] | EC/TC | OC/TC | AAE[b] | Std. Dev.[c] |
|---|---|---|---|---|---|---|---|---|
| BIOTK072 | Bitterbrush Stems | 809.0 | 609.8 | 199.2 | 0.25 | 0.75 | 1.08 | 0.02 |
| BIOTK086 | Carpet Leaves | 8704.8 | 8461.8 | 243.0 | 0.03 | 0.97 | 2.77 | 0.70 |
| BIOTK088 | Wet Duff Composite | 2399.1 | 2382.8 | 16.3 | 0.01 | 0.99 | 5.10 | 1.29 |
| BIOTK102 | Wet Plant Litter | 2976.3 | 2843.1 | 133.2 | 0.04 | 0.96 | 1.42 | 0.08 |
| REST339 | Paved Parking Lot Dust | 15.8 | 10.7 | 5.5 | 0.35 | 0.67 | 0.87 | 0.05 |
| REST2015 | Taconite Dust | 3.0 | 2.9 | 0.2 | 0.05 | 0.95 | 0.79 | 0.11 |
| REST2102 | De-icing material | 1.1 | 1.1 | 0.0 | 0.00 | 1.00 | 2.11 | 0.17 |
| STRST061 | Diesel | 289.0 | 123.0 | 166.5 | 0.58 | 0.43 | 0.76 | 0.07 |
| STRST064 | Diesel | 426.8 | 184.9 | 242.5 | 0.57 | 0.43 | 0.59 | 0.05 |
| STRTQ111 | Acetylene Soot | 330.1 | 8.0 | 322.5 | 0.98 | 0.02 | 0.73 | 0.07 |
| STRTQ133 | Wood Smoke | 246.1 | 193.6 | 53.9 | 0.22 | 0.79 | 1.40 | 0.07 |
| STRTQ136 | Wood Smoke | 77.6 | 42.4 | 36.5 | 0.47 | 0.55 | 1.10 | 0.05 |
| DBIT001 | Pine needles | 1235.4 | 1186.4 | 226.6 | 0.18 | 0.96 | 1.64 | 0.12 |
| DBIT002 | Pine needles | 1508.3 | 1461.3 | 221.9 | 0.15 | 0.97 | 1.78 | 0.16 |
| DBIT003 | Pine needles | 640.4 | 552.2 | 410.3 | 0.64 | 0.86 | 1.05 | 0.04 |
| DBIT005 | Cheat Grass | 319.6 | 304.1 | 95.0 | 0.30 | 0.95 | 2.10 | 0.12 |
| DBIT006 | Cheat Grass | 1249.1 | 1211.1 | 234.0 | 0.19 | 0.97 | 2.60 | 0.33 |
| DBIT007 | Cheat Grass | 625.5 | 602.3 | 142.7 | 0.23 | 0.96 | 2.87 | 0.29 |
| DBIQ2001 | Pine needles | 1235.4 | 1186.4 | 48.9 | 0.04 | 0.96 | 2.17 | 0.38 |
| DBIQ2002 | Pine needles | 1508.3 | 1461.3 | 47.1 | 0.03 | 0.97 | 2.58 | 0.19 |
| DBIQ2003 | Pine needles | 640.4 | 552.2 | 88.2 | 0.14 | 0.86 | 1.86 | 0.19 |
| DBIQ2005 | Cheat Grass | 319.6 | 304.1 | 15.5 | 0.05 | 0.95 | 3.19 | 0.14 |
| DBIQ2006 | Cheat Grass | 1249.1 | 1211.1 | 38.1 | 0.03 | 0.97 | 3.60 | 0.67 |
| DBIQ2007 | Cheat Grass | 625.5 | 602.3 | 23.1 | 0.04 | 0.96 | 4.39 | 0.42 |

| | | | | | | | | |
|---|---|---|---|---|---|---|---|---|
| NCAQ042 | Peat | 139.0 | 137.4 | 1.6 | 0.01 | 0.99 | 4.17 | 0.88 |
| NCAQ072 | Peat | 27.3 | 26.9 | 0.4 | 0.02 | 0.98 | 4.84 | 0.56 |
| NCAQ077 | Peat | 132.0 | 130.8 | 1.1 | 0.01 | 0.99 | 5.42 | 0.54 |
| NCAQ079 | Peat | 316.3 | 314.4 | 1.9 | 0.01 | 0.99 | 4.84 | 0.85 |
| NCAQ080 | Pine Needle | 4.9 | 3.2 | 1.7 | 0.34 | 0.66 | 1.30 | 0.06 |
| NCAQ081 | Pine Needle | 10.6 | 6.3 | 4.3 | 0.40 | 0.60 | 1.30 | 0.09 |
| NCAQ082 | Pine Needle | 16.1 | 9.0 | 7.1 | 0.44 | 0.56 | 1.26 | 0.17 |
| NCAQ083 | Pine Needle | 22.2 | 0.5 | 21.7 | 0.98 | 0.02 | 1.01 | 0.05 |
| NCAQ084 | Pine Needle | 28.4 | 1.8 | 26.6 | 0.94 | 0.06 | 0.98 | 0.07 |
| NCAQ053 | Pine Cone | 399.1 | 398.3 | 0.8 | 0.00 | 1.00 | 4.66 | 1.18 |
| NCAQ091 | Diesel | 10.2 | 3.9 | 6.4 | 0.62 | 0.38 | 1.15 | 0.08 |
| NCAQ092 | Diesel | 12.8 | 5.1 | 7.7 | 0.60 | 0.40 | 1.09 | 0.05 |
| NCAQ093 | Diesel | 19.8 | 5.8 | 14.0 | 0.71 | 0.29 | 0.95 | 0.16 |
| NCAQ094 | Diesel | 7.4 | 6.7 | 0.7 | 0.09 | 0.91 | 1.98 | 0.04 |
| NCAQ095 | Diesel | 55.3 | 12.0 | 43.3 | 0.78 | 0.22 | 0.41 | 0.22 |
| MJQ012[d] | B on D (66:34) | 9326.7 | 3988.0 | 5338.7 | 0.57 | 0.43 | 0.89 | NA |
| MJQ013[d] | B on D (55:45) | 9449.1 | 4346.3 | 5102.8 | 0.54 | 0.46 | 0.94 | NA |
| MJQ017[d] | D on B (31:69) | 1502.3 | 692.0 | 810.1 | 0.54 | 0.46 | 0.96 | NA |
| MJQ018[d] | D on B (92:8) | 24309.9 | 19419.7 | 4890.1 | 0.20 | 0.80 | 1.08 | NA |
| MJT012[d] | B on D (66:34) | 9326.7 | 3988.0 | 5338.7 | 0.57 | 0.43 | 0.60 | NA |
| MJT013[d] | B on D (55:45) | 9449.1 | 4346.3 | 5102.8 | 0.54 | 0.46 | 0.78 | NA |
| MJT017[d] | D on B (31:69) | 1502.3 | 692.0 | 810.1 | 0.54 | 0.46 | NA | NA |
| MJT018[d] | D on B (92:8) | 24309.9 | 19419.7 | 4890.1 | 0.20 | 0.80 | 0.77 | NA |

[a] Units of μg/m$^3$

[b] Averaged sample $\beta_{abs}$ AAE value, calculated from values in Table 3-10.

[c] Standard deviation of the averaged AAE value.

[d] AAE is not averaged. No standard deviation.

### 3.3.2 Layered Source Samples

Due to the heavily loaded nature of these samples, AAE calculations were not performed at the previously stated wavelength pairs for all samples. Therefore, fewer comparisons are made between QF and TM AAE values, as shown in Table 3-14 for ATN < 5. Many AAEs for the layered samples were below 1, though the extremely low values are indicative of sample overloading. These low values occurred most often for the TM samples. Across the board, the QF AAEs are higher than TM. Both $\beta_{abs}$ and $\beta_{ATN}$

derived AAEs are almost always equal within filter type, with the exception of a TM sample (sample #15) with high and variable AAEs of 1.14 and 2.73.

Comparisons between AAE values calculated from $\beta_{ATN}$ ($AAE_{ATN}$) and from $\beta_{abs}$ ($AAE_{abs}$) are shown in Figure 3-23. The QF $AAE_{ATN}$ is generally smaller than $AAE_{abs}$ but, with the removal of one outlier (sample # 15), the relationship between TM $AAE_{ATN}$ and $AAE_{abs}$ became linear.

**Table 3-14.** Layered Source Sample AAE Values[a]

| Sample # | QF Wavelength Pair (nm)[b] | QF AAE $\beta_{abs}$ | QF AAE $\beta_{ATN}$ | TM Wavelength Pair (nm)[b] | TM AAE $\beta_{abs}$ | TM AAE $\beta_{ATN}$ |
|---|---|---|---|---|---|---|
| MJQ/T002 | 615 & 1000 | 0.72 | 0.90 | 250 & 1000 | 0.57 | 0.52 |
| MJQ/T003 | 861 &1000 | 1.07 | 1.06 | 585 & 1000 | 0.95 | 0.97 |
| MJQ/T004 | -- | -- | -- | 544 & 1000 | 0.93 | 0.94 |
| MJQ/T005 | 715 &1000 | 0.93 | 0.95 | 250 & 1000 | 0.51 | 0.50 |
| MJQ/T006 | -- | -- | -- | 615 & 1000 | 0.10 | 0.12 |
| MJQ/T008 | 730 &1000 | 0.54 | 0.56 | 250 & 1000 | 0.33 | 0.33 |
| MJQ/T009 | -- | -- | -- | 250 & 1000 | 0.09 | 0.10 |
| MJQ/T010 | -- | -- | -- | 792 & 1000 | 0.17 | 0.16 |
| MJQ/T012 | 370 & 1000 | 0.80 | 0.89 | 250 & 1000 | 0.60 | 0.59 |
| MJQ/T013 | 440 & 1000 | 0.89 | 0.94 | 250 & 1000 | 0.78 | 0.78 |
| MJQ/T014 | 550 & 1000 | 0.90 | 0.92 | 380 & 1000 | 1.07 | 1.08 |
| MJQ/T015 | 701 & 1000 | 0.93 | 0.93 | 490 & 1000 | 2.73 | 1.14 |
| MJQ/T016 | 791 & 1000 | 0.95 | 0.97 | -- | -- | -- |
| MJQ/T017 | 250 & 1000 | 0.88 | 0.96 | 360 & 1000 | -- | 1.04 |
| MJQ/T018 | 450 & 1000 | 0.87 | 1.08 | 250 & 1000 | 0.77 | 0.74 |
| MJQ/T019 | 910 & 1000 | 0.78 | 0.83 | 250 & 1000 | 0.55 | 0.54 |

[a] AAEs calculated using data at wavelengths only where attenuation (ATN) is less than 5.
[b] Lowest wavelength in pair is the lowest wavelength where attenuation is less than 5.

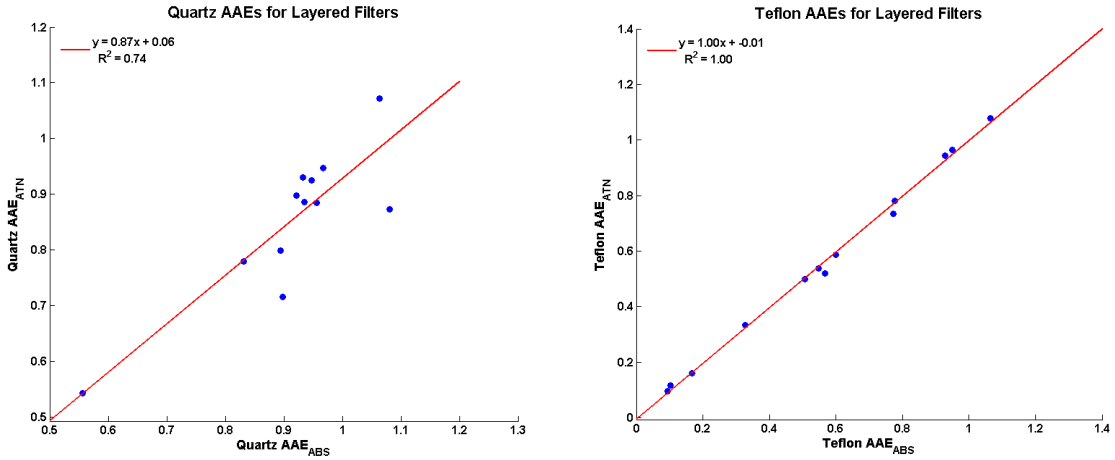


**Figure 3-21.** Relationships between QF AAE values (left) and TM AAE values (left) calculated using $\beta_{ATN}$ and $\beta_{abs}$ for the QF and TM samples shown in Table 3-14, with the removal of one outlier (sample #15 for TM).

### 3.3.3 Ambient Samples

As shown in Tables 3-15 and 3-16, the AAE values for the QF and TM Port of LA samples are all in the range of 0.91 – 1 and 0.73 – 0.79, respectively, with very little deviation, except for one QF sample (SLAFQ68323) which has an AAE ranging from 1.1 – 1.2. These values are indicative of high BC contributions, as would be expected from ship emissions and heavy-duty trucks. On average, QF samples have a higher AAE value (by 0.23 ± 0.12) than TM samples and AAE values calculated from $\beta_{abs}$ are higher (by 0.08 ± 0.04) than $\beta_{ATN}$.

**Table 3-15.** $\boldsymbol{\beta_{abs}}$ AAE Values for Port of LA Samples

| Source Type | Sample ID | AAE λs (nm) | | | | | | Avg. | Std. Dev. |
|---|---|---|---|---|---|---|---|---|---|
| | | All [a] | 8 -λ [a] | 250 & 1000 | 350 & 1000 | 370 & 880 | 400 & 700 | | |
| Port of LA (TM) | SLAFT6759 | 0.83 | 0.86 | 0.79 | 0.85 | 0.85 | 0.84 | 0.79 | 0.02 |
| | SLAFT6804 | 0.78 | 0.80 | 0.75 | 0.80 | 0.80 | 0.78 | | 0.02 |
| | SLAFT6808 | 0.66 | 0.69 | 0.63 | 0.69 | 0.68 | 0.67 | | 0.02 |
| | SLATF6824 | 0.74 | 0.76 | 0.72 | 0.77 | 0.75 | 0.73 | | 0.02 |
| | SLAFT6832 | 0.88 | 0.91 | 0.85 | 0.90 | 0.91 | 0.90 | | 0.02 |
| Port of LA (QF) | SLAFQ6759 | 1.00 | 0.98 | 0.99 | 0.99 | 0.99 | 0.99 | 1.01 | 0.01 |
| | SLAFQ6804 | 1.02 | 0.97 | 1.00 | 1.00 | 0.99 | 0.98 | | 0.02 |
| | SLAFQ6808 | 0.89 | 0.90 | 0.87 | 0.91 | 0.90 | 0.89 | | 0.01 |
| | SLAFQ6824 | 0.98 | 0.97 | 0.95 | 0.99 | 0.97 | 0.96 | | 0.01 |
| | SLAFQ6832 | 1.26 | 1.17 | 1.20 | 1.23 | 1.22 | 1.22 | | 0.03 |

[a] AAE calculated using power law curve fit of $\boldsymbol{\beta_{abs}}$ data points.

**Table 3-16.** $\boldsymbol{\beta_{ATN}}$ AAE Values for Port of LA Samples

| Source Type | Sample ID | AAE λs (nm) | | | | | | Avg. | Std. Dev. |
|---|---|---|---|---|---|---|---|---|---|
| | | All [a] | 8 -λ [a] | 250 & 1000 | 350 & 1000 | 370 & 880 | 400 & 700 | | |
| Port of LA (TM) | SLAFT6759 | 0.73 | 0.75 | 0.71 | 0.75 | 0.74 | 0.74 | 0.73 | 0.02 |
| | SLAFT6804 | 0.77 | 0.78 | 0.75 | 0.78 | 0.78 | 0.76 | | 0.01 |
| | SLAFT6808 | 0.64 | 0.66 | 0.61 | 0.66 | 0.66 | 0.64 | | 0.02 |
| | SLATF6824 | 0.68 | 0.69 | 0.66 | 0.70 | 0.68 | 0.66 | | 0.01 |
| | SLAFT6832 | 0.82 | 0.84 | 0.79 | 0.84 | 0.85 | 0.83 | | 0.02 |
| Port of LA (QF) | SLAFQ6759 | 0.88 | 0.87 | 0.89 | 0.88 | 0.87 | 0.85 | 0.91 | 0.01 |
| | SLAFQ6804 | 0.88 | 0.84 | 0.87 | 0.86 | 0.85 | 0.82 | | 0.02 |
| | SLAFQ6808 | 0.80 | 0.80 | 0.79 | 0.82 | 0.80 | 0.77 | | 0.02 |
| | SLAFQ6824 | 0.88 | 0.88 | 0.86 | 0.91 | 0.88 | 0.84 | | 0.02 |
| | SLAFQ6832 | 1.21 | 1.15 | 1.14 | 1.20 | 1.18 | 1.16 | | 0.03 |

[a] AAE calculated using power law curve fit of $\boldsymbol{\beta_{ATN}}$ data points.

The Rim Fire samples exhibit a wide range of AAE values, as shown in Table 3-17 and 3-18. In contrast to the Port of LA samples, the TM AAE values are higher than the QF AAEs, although $\beta_{abs}$ derived AAEs are higher than those of $\beta_{ATN}$. These samples are further separated into two visually different groups: one under high impact of

smoke transport (highlighted in brown) and the other is not. Average AAEs for the first group, ranging from 1.58-2.14, are larger than those for the second group and are consistent with values reported for biomass burning. However, only AAEs calculated using $\beta_{abs}$ return values of 2 or greater. Average AAEs for the second group ranged from 0.7 – 1.18 with many values below 1 for the QF samples. Because of the day-to-day variation in the samples, statistical comparisons of the individual Rim Fire AAEs are not useful.

**Table 3-17.** $\beta_{abs}$ AAE Values for Rim Fire Samples

| Source Type | Sample ID | AAE λs (nm) | | | | | | Avg. | Std. Dev. |
|---|---|---|---|---|---|---|---|---|---|
| | | All [a] | 8 -λ [a] | 250 & 1000 | 350 & 1000 | 370 & 880 | 400 & 700 | | |
| Rim Fire (TM) | SDKT083[b] | 1.88 | 1.90 | 1.70 | 1.94 | 1.97 | 2.07 | 2.14 | 0.12 |
| | SDKT085 | 1.91 | 1.79 | 1.84 | 1.91 | 1.89 | 1.94 | | 0.05 |
| | SDKT082 | 2.04 | 2.09 | 1.84 | 2.10 | 2.14 | 2.28 | | 0.14 |
| | SDKT086 | 2.13 | 2.10 | 1.97 | 2.16 | 2.20 | 2.31 | | 0.11 |
| | SDKT088 | 2.72 | 2.62 | 2.63 | 2.70 | 2.73 | 2.68 | | 0.04 |
| | SDKT090 | 2.20 | 2.05 | 2.18 | 2.17 | 2.14 | 2.14 | | 0.05 |
| | SDKT089 | 1.14 | 1.13 | 1.13 | 1.13 | 1.13 | 1.14 | 1.18 | 0.01 |
| | SDKT091 | 1.09 | 1.08 | 1.05 | 1.08 | 1.09 | 1.10 | | 0.02 |
| | SDKT093 | 1.35 | 1.30 | 1.38 | 1.36 | 1.29 | 1.24 | | 0.05 |
| Rim Fire (QF) | SDKQ0459[b] | 1.51 | 1.61 | 1.28 | 1.58 | 1.64 | 1.83 | 1.58 | 0.18 |
| | SDKQ0464 | 1.56 | 1.26 | 1.73 | 1.43 | 1.44 | 1.54 | | 0.16 |
| | SDKQ0469 | 1.77 | 1.68 | 1.59 | 1.76 | 1.84 | 2.06 | | 0.16 |
| | SDKQ0479 | 2.15 | 2.06 | 1.94 | 2.15 | 2.24 | 2.44 | | 0.17 |
| | SDKQ0489 | 1.03 | 0.72 | 1.23 | 0.84 | 0.84 | 0.93 | | 0.18 |
| | SDKQ0494 | 1.64 | 1.29 | 1.79 | 1.44 | 1.44 | 1.53 | | 0.17 |
| | SDKQ0499 | 1.09 | 0.87 | 1.31 | 0.92 | 0.92 | 0.97 | 0.91 | 0.16 |
| | SDKQ0505 | 1.00 | 0.87 | 1.13 | 0.90 | 0.90 | 0.94 | | 0.10 |
| | SDKQ0515 | 0.80 | 0.67 | 0.89 | 0.72 | 0.73 | 0.78 | | 0.07 |

[a] AAE calculated using power law curve fit of $\beta_{abs}$ data points.

[b] Samples under influence of smoke transport are highlighted in brown.

**Table 3-18.** $\beta_{ATN}$ AAE Values for Rim Fire Samples

| Source Type | Sample ID | AAE λs (nm) | | | | | | Avg. | Std. Dev. |
|---|---|---|---|---|---|---|---|---|---|
| | | All [a] | 8 -λ [a] | 250 & 1000 | 350 & 1000 | 370 & 880 | 400 & 700 | | |
| Rim Fire (TM) | SDKT083 [b] | 1.47 | 1.46 | 1.35 | 1.52 | 1.52 | 1.56 | 1.46 | 0.07 |
| | SDKT085 | 1.25 | 1.15 | 1.24 | 1.23 | 1.21 | 1.21 | | 0.04 |
| | SDKT082 | 1.49 | 1.49 | 1.39 | 1.53 | 1.54 | 1.60 | | 0.07 |
| | SDKT086 | 1.49 | 1.45 | 1.41 | 1.51 | 1.52 | 1.54 | | 0.05 |
| | SDKT088 | 1.50 | 1.35 | 1.54 | 1.42 | 1.41 | 1.40 | | 0.07 |
| | SDKT090 | 1.68 | 1.56 | 1.68 | 1.63 | 1.62 | 1.60 | | 0.05 |
| | SDKT089 | 1.05 | 1.04 | 1.05 | 1.03 | 1.04 | 1.04 | 1.06 | 0.01 |
| | SDKT091 | 0.98 | 0.97 | 0.96 | 0.96 | 0.97 | 0.97 | | 0.01 |
| | SDKT093 | 1.20 | 1.17 | 1.25 | 1.21 | 1.15 | 1.10 | | 0.05 |
| Rim Fire (QF) | SDKQ0459 [b] | 0.80 | 0.86 | 0.67 | 0.85 | 0.88 | 1.02 | 1.26 | 0.11 |
| | SDKQ0464 | 1.61 | 1.40 | 1.71 | 1.52 | 1.54 | 1.68 | | 0.11 |
| | SDKQ0469 | 1.59 | 1.55 | 1.42 | 1.61 | 1.66 | 1.86 | | 0.14 |
| | SDKQ0479 | 1.52 | 1.48 | 1.34 | 1.53 | 1.61 | 1.79 | | 0.15 |
| | SDKQ0489 | 0.95 | 0.69 | 1.10 | 0.79 | 0.79 | 0.88 | | 0.14 |
| | SDKQ0494 | 1.19 | 0.90 | 1.30 | 1.01 | 1.02 | 1.11 | | 0.14 |
| | SDKQ0499 | 0.65 | 0.45 | 0.87 | 0.49 | 0.49 | 0.55 | 0.71 | 0.16 |
| | SDKQ0505 | 0.73 | 0.62 | 0.86 | 0.64 | 0.65 | 0.69 | | 0.09 |
| | SDKQ0515 | 0.88 | 0.77 | 0.93 | 0.82 | 0.82 | 0.88 | | 0.06 |

[a] AAE calculated using power law curve fit of $\beta_{ATN}$ data points.

[b] Samples under influence of smoke transport are highlighted in brown.

Tables 3-19 and 3-20 show AAEs of 0.71 – 1.06 for the TCEQ Clinton samples under local influence, which are similar to those found for Port of LA samples. On the days that African dust was predicted to be present in the Houston area (highlighted in grey), the AAE values are increased, ranging from 0.96 to 1.46. As it was for the Rim Fire samples, statistical comparisons of the TCEQ samples are more variable than useful especially because there are no QF AAEs calculated from $\beta_{abs}$. Similar to the Port of LA samples, $\beta_{abs}$ derived AAEs for TM are higher than those of $\beta_{ATN}$ and AAEs for QF are higher than those for TM samples.

**Table 3-19. $\boldsymbol{\beta_{abs}}$** AAE Values for TCEQ Clinton St. Samples (TM only)

| Source Type | Sample ID | AAE λs (nm) | | | | | | Avg. | Std. Dev. |
|---|---|---|---|---|---|---|---|---|---|
| | | All [a] | 8 -λ [a] | 250 & 1000 | 350 & 1000 | 370 & 880 | 400 & 700 | | |
| Clinton St. (TM) | TC135T14050 | 0.93 | 0.94 | 0.91 | 0.94 | 0.94 | 0.94 | 0.87 | 0.01 |
| | TC135T14053 | 0.76 | 0.77 | 0.74 | 0.78 | 0.77 | 0.76 | | 0.02 |
| | TC135T14055 | 0.90 | 0.93 | 0.87 | 0.92 | 0.92 | 0.91 | | 0.02 |
| | TC135T14056 | 0.81 | 0.85 | 0.77 | 0.85 | 0.85 | 0.84 | | 0.03 |
| | TC135T14102 | 0.93 | 0.95 | 0.89 | 0.95 | 0.95 | 0.96 | | 0.03 |
| | TC135T14108[b] | 1.14 | 1.15 | 1.10 | 1.17 | 1.15 | 1.16 | 1.15 | 0.02 |
| | TC135T14109 | 1.76 | 1.79 | 1.66 | 1.77 | 1.80 | 1.94 | | 0.09 |
| | TC135T14111 | 0.96 | 0.97 | 0.93 | 0.97 | 0.97 | 0.98 | | 0.02 |
| | TC135T14112 | 0.87 | 0.90 | 0.84 | 0.90 | 0.89 | 0.89 | | 0.02 |
| | TC135T14113 | 0.94 | 0.98 | 0.90 | 0.98 | 0.97 | 0.96 | | 0.03 |

[a] AAE calculated using power law curve fit of $\boldsymbol{\beta_{abs}}$ data points.

[b] Samples impacted by African dust transport are highlighted in gray.

**Table 3-20.** $\boldsymbol{\beta_{ATN}}$ AAE Values for TCEQ Clinton St. Samples

| Source Type | Sample ID | AAE λs (nm) | | | | | | Avg. | Std. Dev. |
|---|---|---|---|---|---|---|---|---|---|
| | | All [a] | 8 -λ [a] | 250 & 1000 | 350 & 1000 | 370 & 880 | 400 & 700 | | |
| Clinton St. (TM) | TC135T14050 | 0.77 | 0.77 | 0.76 | 0.78 | 0.77 | 0.76 | 0.81 | 0.01 |
| | TC135T14053 | 0.72 | 0.74 | 0.71 | 0.75 | 0.73 | 0.70 | | 0.02 |
| | TC135T14055 | 0.84 | 0.86 | 0.83 | 0.86 | 0.85 | 0.84 | | 0.01 |
| | TC135T14056 | 0.81 | 0.85 | 0.79 | 0.85 | 0.84 | 0.83 | | 0.03 |
| | TC135T14102 | 0.89 | 0.92 | 0.86 | 0.92 | 0.92 | 0.89 | | 0.02 |
| | TC135T14108 [b] | 1.00 | 1.00 | 0.98 | 1.02 | 1.01 | 1.01 | 0.96 | 0.02 |
| | TC135T14109 | 1.20 | 1.17 | 1.16 | 1.17 | 1.20 | 1.29 | | 0.05 |
| | TC135T14111 | 0.88 | 0.88 | 0.85 | 0.89 | 0.89 | 0.89 | | 0.02 |
| | TC135T14112 | 0.85 | 0.87 | 0.82 | 0.87 | 0.87 | 0.87 | | 0.02 |
| | TC135T14113 | 0.86 | 0.88 | 0.84 | 0.89 | 0.88 | 0.88 | | 0.02 |
| Clinton St. (QF) | TC135Q14050 | 1.01 | 0.89 | 1.30 | 0.93 | 0.92 | 0.92 | 0.85 | 0.16 |
| | TC135TQ4053 | 0.79 | 0.81 | 0.77 | 0.84 | 0.82 | 0.82 | | 0.03 |
| | TC135Q14055 | 0.81 | 0.84 | 0.80 | 0.86 | 0.84 | 0.85 | | 0.02 |
| | TC135Q14056 | 0.81 | 0.84 | 0.84 | 0.86 | 0.84 | 0.85 | | 0.02 |
| | TC135Q14102 | 0.74 | 0.75 | 0.71 | 0.75 | 0.76 | 0.78 | | 0.02 |
| | TC135Q14108 [b] | 1.21 | 1.21 | 1.18 | 1.23 | 1.22 | 1.22 | 0.98 | 0.02 |
| | TC135Q14109 | 0.92 | 0.83 | 0.94 | 0.85 | 0.87 | 0.95 | | 0.05 |
| | TC135Q14111 | 0.91 | 0.90 | 0.89 | 0.91 | 0.91 | 0.93 | | 0.02 |
| | TC135Q14112 | 0.76 | 0.78 | 0.68 | 0.79 | 0.78 | 0.81 | | 0.04 |
| | TC135Q14113 | 1.09 | 1.12 | 1.02 | 1.14 | 1.13 | 1.12 | | 0.04 |

[a] AAE calculated using power law curve fit of $\boldsymbol{\beta_{ATN}}$ data points.
[b] Samples impacted by African dust transport are highlighted in gray.

Carbon content and average AAEs for the ambient samples examined are summarized in Table 3-21. High AAEs for the Rim Fire samples corresponded to high OC/TC ratios of 0.89 – 0.92. EC concentrations for the Port of LA samples exceeded 1.6 μg/m$^3$ with EC/TC ratios ranging from 0.34 – 0.40 and average QF AAEs of 0.97 – 1.22. This is consistent with measurements for other BC dominated source samples. When examining the relationship between AAE and sample EC/TC (Figure 3-24), AAE scattering at low EC/TC levels is similar to that shown in Figure 3-22 (source samples). There is not much change in AAEs as EC/TC increased from 0.2 to 0.45.

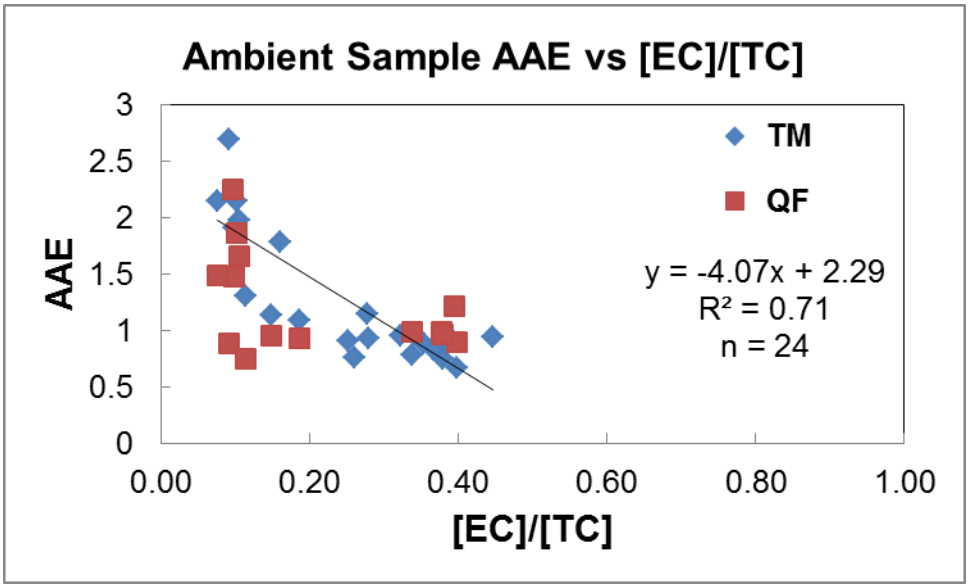


**Figure 3-22.** Relationship between ambient sample AAE values and the sample TC fraction. Data is differentiated between TM and QF AAE values, though the relationship holds for both filter media. EC and TC were determined using the DRI Model 2001 Carbon Analyzer for thermal/optical carbon analysis following IMRPOVE_A thermal/optical reflectance protocol (Chow et al., 2007).

**Table 3-21.** Ambient Sample Carbon Fractions and Average[a] AAE Values

| TID | Sample | OC | EC | TC | EC/TC | OC/TC | TM AAE | QF AAE |
|---|---|---|---|---|---|---|---|---|
| SLAFT/Q6759 | Port of LA | 3.18 | 1.90 | 5.04 | 0.38 | 0.63 | 0.83 | 0.99 |
| SLAFT/Q6804 | Port of LA | 3.17 | 1.61 | 4.74 | 0.34 | 0.67 | 0.79 | 0.99 |
| SLAFT/Q6808 | Port of LA | 2.97 | 1.94 | 4.87 | 0.40 | 0.61 | 0.67 | 0.89 |
| SLAFT/Q6824 | Port of LA | 4.19 | 2.54 | 6.69 | 0.38 | 0.63 | 0.74 | 0.97 |
| SLAFT/Q6832 | Port of LA | 2.72 | 1.75 | 4.43 | 0.40 | 0.61 | 0.89 | 1.22 |
| SDKT083/Q0459 | Rim Fire | 18.76 | 2.22 | 20.98 | 0.11 | 0.89 | 1.97 | 1.66 |
| SDKT085/Q0464 | Rim Fire | 7.64 | 0.84 | 8.48 | 0.10 | 0.90 | 1.91 | 1.47 |
| SDKT082/Q0469 | Rim Fire | 13.67 | 1.56 | 15.23 | 0.10 | 0.90 | 2.15 | 1.86 |
| SDKT086/Q0479 | Rim Fire | 7.97 | 0.86 | 8.83 | 0.10 | 0.90 | 2.20 | 2.25 |
| SDKT088/Q0489 | Rim Fire | 2.34 | 0.24 | 2.57 | 0.09 | 0.91 | 2.70 | 0.89 |
| SDKT090/Q0494 | Rim Fire | 3.23 | 0.27 | 3.49 | 0.08 | 0.92 | 2.15 | 1.48 |
| SDKT089/Q0499 | Rim Fire | 1.84 | 0.32 | 2.16 | 0.15 | 0.85 | 1.13 | 0.96 |
| SDKT091/Q0505 | Rim Fire | 2.22 | 0.51 | 2.74 | 0.19 | 0.81 | 1.08 | 0.92 |
| SDKT093/Q0515 | Rim Fire | 3.35 | 0.43 | 3.78 | 0.11 | 0.89 | 1.30 | 0.75 |
| TC135T/Q14050 | TCEQ Clinton St. | 3.46 | 1.35 | 4.80 | 0.28 | 0.72 | 0.93 | NA |
| TC135T/Q14053 | TCEQ Clinton St. | 2.37 | 0.84 | 3.21 | 0.26 | 0.74 | 0.76 | NA |
| TC135T/Q14055 | TCEQ Clinton St. | 2.30 | 0.77 | 3.07 | 0.25 | 0.75 | 0.91 | NA |
| TC135T/Q14056 | TCEQ Clinton St. | 1.81 | 1.06 | 2.87 | 0.37 | 0.63 | 0.83 | NA |
| TC135T/Q14102 | TCEQ Clinton St. | 1.39 | 1.12 | 2.51 | 0.45 | 0.55 | 0.94 | NA |
| TC135T/Q14108 | TCEQ Clinton St. | 1.43 | 0.55 | 1.99 | 0.28 | 0.72 | 1.15 | NA |
| TC135T/Q14109 | TCEQ Clinton St. | 0.85 | 0.16 | 1.01 | 0.16 | 0.84 | 1.79 | NA |
| TC135T/Q14111 | TCEQ Clinton St. | 1.51 | 0.79 | 2.30 | 0.34 | 0.66 | 0.96 | NA |
| TC135T/Q14112 | TCEQ Clinton St. | 2.16 | 1.19 | 3.35 | 0.35 | 0.65 | 0.88 | NA |
| TC135T/Q14113 | TCEQ Clinton St. | 1.56 | 0.74 | 2.30 | 0.32 | 0.68 | 0.95 | NA |

[a] Averaged sample $\beta_{abs}$ AAE value, calculated using values from Tables 3-15 through 3-20.
[b] Samples under influence of smoke transport are highlighted in brown and those impacted by African dust transport are highlighted in gray.

## 3.4 Absorption Approximations and Contribution to Radiative Forcing (RF)

Because PM light absorption can be obtained in many ways, it is useful to explore how these various approaches can alter a sample's absorption spectra and, in a broad sense, the sample's contribution to RF through absorption.

Past studies have approximated BC absorption by extrapolating from a specific $\beta_{abs}$, usually around 880 nm, using a power law assumption and an AAE value of 1 (Chakrabarty et al. (2010), Kirchstetter and Thatcher (2012), Zhong and Jang (2014), Massabò et al. (2015), Lack and Langridge (2013)). Similarly, absorption can be extrapolated from multi-wavelength absorption measurements and AAE calculations (e.g. Magee Transmissometer at 370 and 880 nm, photoacoustic spectrometer at 405, 532, and 781 nm).

In this section, the $\tau_a$ obtained using the Lambda 35 (i.e. 1 nm resolution) is compared to absorption extrapolation methods: 1) an AAE = 1, extrapolated from the 880 nm data point, 2) an AAE calculated from the 370 and 880 nm data points and extrapolated from the 880 nm data point and 3) an AAE calculated using a power law curve-fit of three data points (405, 532, and 781 nm) and the extrapolation of the curve from the 781 nm data point.

The $\tau_a$value obtained from Equations 17 - 21 was used to represent a sample's absorption optical depth. While this is not truly an accurate representation of optical

depth (extinction over an atmospheric column), it suffices to give a relative approximation. Several source samples (listed in Table 3-22) were chosen to examine the differences inherent in various absorption approximations and between source types. Each source sample's $\tau_a$ was normalized by the average $\tau_a$, denoted as $<\tau_a>$. Figure 3-25 shows the normalized $\tau_a$ spectra for each source type. Elevated normalized $\tau_a$ were found for the smoldering biomass (cheat grass) and paved road dust samples at low wavelengths (300 – 400 nm).

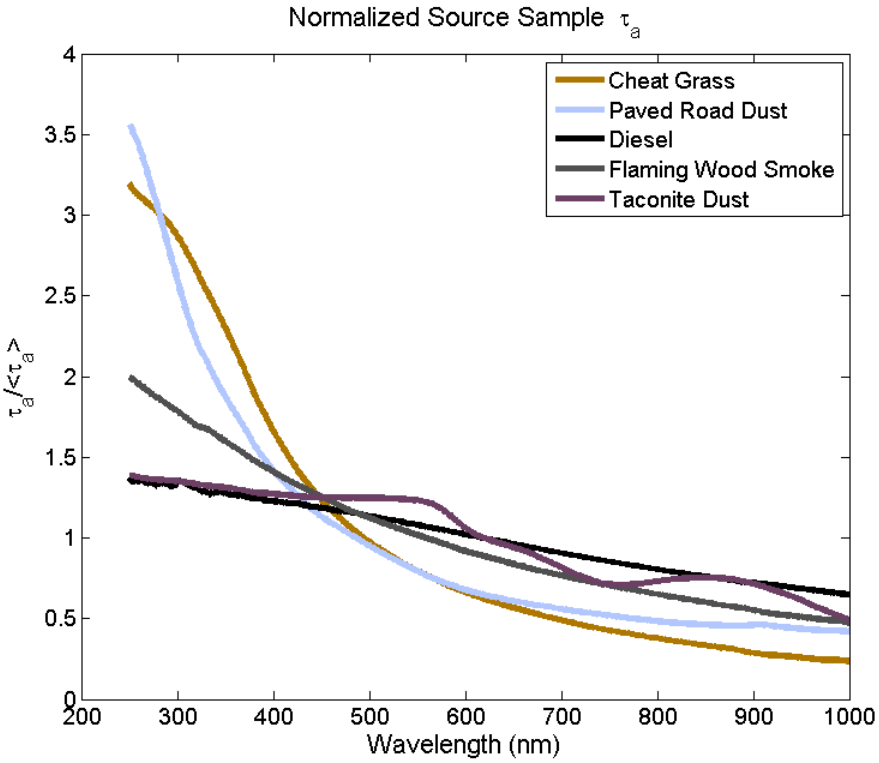


**Figure 3-23.** Normalized $\boldsymbol{\tau_a}$ for various source samples. The area under each curve is approximately equal. Smoldering biomass (cheat grass) and paved road dust have the highest relative absorption at low wavelengths (250 – 400 nm).

The aforementioned absorption approximations were applied to each sample and were compared to each other: 1) across the measured spectrum (250 – 1000 nm) (Figure 3-25); and 2) relative to solar radiation reaching the Earth's surface (i.e. at noon on the summer solstice at Toolik Lake, AK, at noon on the summer solstice and at noon in Reno, NV, in August). These two situations were chosen because the warming climate is of major concern above the Arctic Circle and there is usually a wildfire affecting Reno in August. The solar radiation reaching Earth's surface was approximated using Planck's blackbody equation and the Rayleigh optical depth at each location, as follows:

$$Radiation_{surface} = \int_{350}^{1000} B_{(T,\lambda)} d\lambda =$$

$$= \int_{350}^{1000} \frac{2hc^2}{\lambda^5} \frac{1}{e^{\frac{hc}{\lambda k_B T}} - 1} \left(\frac{R_s}{R_{SE}}\right)^2 e^{-\tau_{Rayleigh(\lambda)}} \, d\lambda \tag{23}$$

where h = 6.63x10$^{-34}$ m$^2$kg/s (Planck's constant), c = 3x10$^8$ m/s (speed of light), $k_B$= 1.38x10$^{-23}$ m$^2$kg/s$^2$K (Boltzmann constant), T is the blackbody temperature (assumed here as the sun, 5778 K), $R_S$ = 432,474 mi (radius of sun), $R_{SE}$ = 9.3x10$^7$ mi (distance from sun to Earth), and $\tau_{Rayleigh(\lambda)}$ is the wavelength dependent Rayleigh optical depth. Multiplying the blackbody radiation of the sun by $\left(\frac{R_s}{R_{SE}}\right)^2$ first approximates how much radiation would reach the top of Earth's atmosphere. Further multiplying by $e^{-\tau_{Rayleigh(\lambda)}}$ gives an approximation for how much radiation makes it through the atmosphere after losses due to Rayleigh scattering. There are many approaches to

calculating $\tau_{Rayleigh(\lambda)}$ (Bodhaine et al, 1999), but the $\tau_{Rayleigh(\lambda)}$ values used in this study were calculated based on location, time of day, and air pressure using an online calculator.[4] The specific inputs for Toolik Lake, AK, and Reno, NV, are listed in Table 3-23. The approach used here essentially provides a direct-beam look at the solar radiation reaching the earth's surface, but multiplying the assumption above by the cosine of the solar zenith angle would allow for a better horizontal representation of the radiation through the atmosphere.

Comparing the absorption approximations as integrated areas across the measured spectra (250 – 1000 nm), as shown in Table 3-22 reveals some important information. First, assuming an AAE of 1 at 880 nm will rarely yield appropriate results by extrapolation. It overestimates for the diesel samples by 12 and 20%. It is also not a good representation for most of the biomass samples (except for sample DBIT003) or for the dust samples. Lack and Langridge (2013) warn of the pitfalls of this estimation method, in terms of trying to delineate BrC and BC contributions. By varying the BC AAE value over the wide range of values reported in literature, they observed BC absorption attribution bias ranging from +20% to -40%.

Extrapolating using the AAEs from 370 and 880 nm does quite well at reproducing the same integrated area, though it still overestimates the biomass curves by 4 – 24%. The power law curve-fit of 3-λ method gets a little closer to unity for four out

[4] W. Patrick Arnott and Ben Sumlin. http://patarnott.com/office/AnalyzeSunPhotometerUNR.pl

of the six biomass samples; however, it still overestimates two sample areas (i.e. DBIT006 and DBIT007) by 24 and 26%.

**Table 3-22.** Integrated Curve Area (250 – 1000 nm) Ratios of Absorption Approximation Methods

| Sample ID | Source Type | Ratio of Method to Lambda 35 Curve | | |
|---|---|---|---|---|
| | | AAE = 1 | 370 & 880 nm | 3λ (405, 532, 781 nm) |
| REST339 | Paved Parking Lot Dust | 1.09 | 0.99 | 0.97 |
| REST1856 | Paved Road Dust | 0.75 | 1.02 | 0.94 |
| REST2015 | Taconite Dust | 1.21 | 1.00 | 1.00 |
| REST2102 | De-icing Material | 0.51 | 1.04 | 0.91 |
| DBIT001 | Pine Needle | 0.72 | 1.10 | 0.99 |
| DBIT002 | Pine Needle | 0.66 | 1.13 | 1.02 |
| DBIT003 | Pine Needle | 0.99 | 1.04 | 0.98 |
| DBIT005 | Cheat Grass | 0.51 | 1.10 | 1.05 |
| DBIT006 | Cheat Grass | 0.36 | 1.23 | 1.26 |
| DBIT007 | Cheat Grass | 0.30 | 1.24 | 1.24 |
| STRST061 | Diesel | 1.12 | 1.00 | 1.03 |
| STRST064 | Diesel | 1.20 | 0.98 | 1.02 |
| STRTQ133 | Flaming Wood Smoke | 0.78 | 1.02 | 1.03 |
| STRTQ136 | Flaming Wood Smoke | 0.94 | 1.01 | 1.02 |

Figure 3-26 shows absorption approximation curves for a pine needle sample plotted with the radiation that reaches the Earth's surface above the Arctic Circle on the summer solstice and at Reno in August. By examining these approximations plotted together, as shown in Figure 3-26, it becomes evident that these methods do not approximate the rapid increase of absorption for the biomass samples well. This was

also noted when fitting the sample curves for AAEs in the previous section. The forcing due to absorption in each location was estimated to be the area under the intersection of the absorption curve and the solar radiation curve, starting from 350 nm. The ratio between each method intersection area and the Lambda 35 intersection area is calculated and the percent of over- or underestimation is reported in Table 3-23.

These calculations re-emphasize that the AAE = 1 approximation is not a great method. For these samples, the RF approximations ranged from -54 to +27% of that estimated by the Lambda 35. The 370 and 880 nm method ranged from -76 to +23% of the Lambda 35 curve, and the 3-λ method produced the best agreement with small deviations (-7.3 to 5.5% with the exclusion of two dust samples, REST339 and REST1856).

**Table 3-23.** Inputs to Rayleigh Optical Depth Calculator

| Variable | Reno, NV | Toolik Lake, AK |
|---|---|---|
| Pressure (mb) | 875.56 | 1013.25 |
| Time Zone | -7 | -8 |
| Hour | 12 | 12 |
| Minute | 0 | 0 |
| Second | 0 | 0 |
| Month | 8 | 6 |
| Day | 1 | 21 |
| Year | 2015 | 2015 |
| Latitude | 39.54117 | 68.66109 |
| Longitude | -119.81406 | -149.37047 |

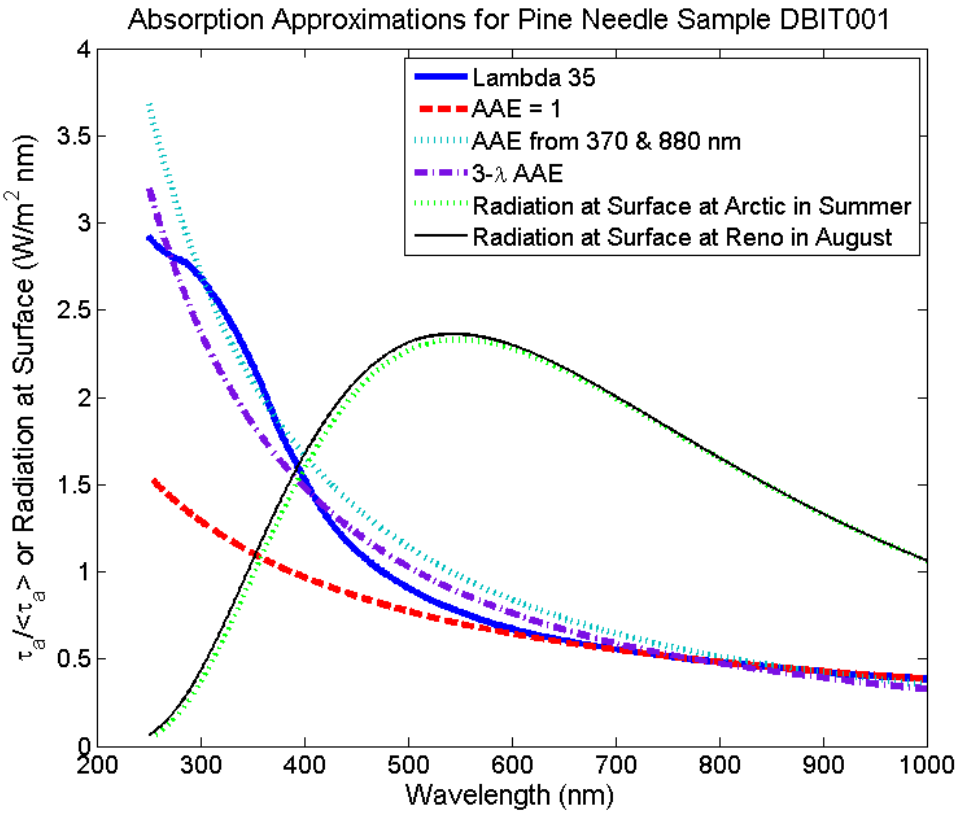


**Figure 3-24.** Absorption curves for a pine needle burning sample compared to the solar radiation reaching the Earth's surface at both Toolik Lake, AK, (arctic in summer) and Reno, NV (in August). Forcing estimates were made by finding the area under the intersection of the absorption curves and the solar radiation curve, starting from 350 nm.

**Table 3-24.** Percent Differences in Absorption RF Estimates by Sample

| Sample ID | Source Type | Reno, NV in August | | | Toolik Lake, AK on Summer Solstice | | |
|---|---|---|---|---|---|---|---|
| | | AAE =1 | 370 & 880 nm | 3λ | AAE =1 | 370 & 880 nm | 3λ |
| REST339 | Paved Parking Lot Dust | 8.1 | 2.5 | 0.7 | -9.3 | 8.7 | 21.0 |
| REST1856 | Paved Road Dust | 7.9 | 2.5 | -15.5 | -9.8 | 8.7 | 0.1 |
| REST2015 | Taconite Dust | 9.2 | -2.6 | -7.1 | 8.8 | -2.6 | -7.3 |
| REST2102 | De-icing Material | -22.1 | 20.1 | 4.5 | -21.3 | 20.2 | 4.6 |
| DBIT001 | Pine Needle | -11.7 | 13.4 | 4.1 | -11.1 | 23.2 | 4.2 |
| DBIT002 | Pine Needle | -19.7 | 15.3 | 4.6 | -18.8 | 15.2 | 5.5 |
| DBIT003 | Pine Needle | 3.4 | 6.2 | 1.8 | 3.5 | 6.2 | 1.8 |
| DBIT005 | Cheat Grass | -34.0 | 4.7 | 2.3 | -33.3 | 4.7 | 2.4 |
| DBIT006 | Cheat Grass | -48.7 | 5.0 | 2.0 | -48.0 | 5.1 | 2.0 |
| DBIT007 | Cheat Grass | -54.8 | 5.9 | 2.6 | -54.1 | 6.0 | 2.7 |
| STRST061 | Diesel | 3.2 | -3.3 | -1.0 | 3.0 | -3.3 | -1.0 |
| STRST064 | Diesel | 3.2 | -3.3 | 1.2 | 3.0 | -3.3 | 1.3 |
| STRTQ133 | Flaming Wood Smoke | -16.4 | -1.4 | -1.4 | -16.0 | -1.4 | -1.4 |
| STRTQ136 | Flaming Wood Smoke | -6.3 | -2.0 | -0.1 | -6.2 | -2.0 | -0.2 |

# 4. Summary, Conclusions and Recommendations

The three study objectives: 1) to compare spectral absorption measurements between QF and TM filter types and between absorption measurement instruments; 2) to examine the variability of AAE for biomass burning and fossil fuel combustion; and 3) to evaluate the extent to which source contributions can be differentiated from ambient samples using light absorption ratios at different wavelengths are met with the collected ambient and source samples. Measurements and comparisons presented in Section 3 are used to test the three hypotheses listed in Section 1.7. Effects from filter media and particle loadings are summarized with recommendation for future studies.

## 4.1 Summary and Conclusions

### 4.1.1 Reflectance and Transmittance

This study examined the UV-Visible Lambda 35 spectrometer for use in measuring diffuse reflectance and transmittance of QF and TM filter samples. Laboratory generated source samples and ambient samples were measured. All samples were characterized using the Beer-Lambert law for attenuation as well as by a two-layer radiative transfer model to estimate $\beta_{abs}$.

By comparing the reflectance and transmittance measurements of source samples, spectral patterns are distinguishable for diesel (BC), biomass (BrC) and dust dominated ambient samples. Biomass burning samples have a characteristic plateau (or

gentle downward slope depending on the filter type) in the visible wavelength region followed by a rapid reduction of reflectance and transmittance signal in the visible and UV wavelengths. Both the reflectance and transmittance curves can be approximated using a high order polynomial curve fit (usually 6$^{th}$ order). More BC-dominated biomass samples, like the flaming wood smoke, can have a reflectance spectrum that is relatively flat (more EC) or one that has a similar rapid reduction in signal to a biomass burning sample (less EC). The reflectance curves of these samples are also approximated using a high order polynomial but the transmittance is better approximated using a 3$^{rd}$ order polynomial. Dust samples tend to have a minor reflectance peak in the visible and the signal falls off at various rates into the UV, though not nearly as rapidly as biomass burning. The reflectance curves can usually be approximated with a 4$^{th}$ order polynomial, though these samples were not extremely well by curve fits over all. The dust transmittance signals decrease with decreasing wavelength and can be approximated with a 3$^{rd}$ order polynomial. The reflectance and transmittance signals for diesel samples decrease slowly with decreasing wavelength and are, as expected, relatively spectrally flat compared to the other source samples. Diesel reflectance curves can be approximated with equations ranging from a 3$^{rd}$ order polynomial for a more lightly loaded sample to a linear fit for a more heavily loaded sample. Diesel transmittance curves can be approximated with a 2$^{nd}$ order polynomial or a linear equation, depending on the mass loading.

Impacts from biomass and dust transport can be found in the reflectance signals of ambient samples from the TCEQ Clinton St. site in Houston, TX, and from samples taken during the Rim Fire in Reno, NV. The biomass reflectance signal was recognizable in a couple of layered source samples, most notably sample #18 with an 8% diesel layer on 92% biomass burning emissions. The other layered samples were too heavily loaded or dominated by diesel to visually observe this signal. The order of the source layers on the filters seemed to play some role in the amount of light transmitted or reflected from the sample – the higher reflectance and transmittance values generally correlated to samples with a top layer of biomass, though mass loading and percentage of diesel also factor in to some extent.

Overall, these results support part of the second Hypothesis of this study – this method can be used to identify BrC, BC and mineral dust in filter samples using reflectance and transmittance spectra. Because the visual and mathematical patterns are distinguishable between source types, most notably for the reflectance measurements, this aspect of the method exhibits promise and should be explored further.

### 4.1.2 Attenuation and Absorption

In terms of the measurement method for the first Hypothesis, the $\beta_{abs}$ calculated from the Lambda 35 measurements compared within error margins with several densitometer measurements (centered at 550 nm) of source sample TM filters. These TM source filters were also measured with a Magee dual-wavelength (370 and 880 nm)

transmissometer and the $\beta_{ATN}$ values were compared with those calculated from the Lambda 35 measurements. These methods also compared within error margins on some filter samples, but did not compare well with others. The values obtained from all three methods are highly dependent on the blank filter measurement used in the absorption or attenuation calculations, and nearly all of these calculations were made with blank measurements of filters different from the sample filters.

When compared with collocated laboratory biomass burning sampling by a 3-$\lambda$ PAS (405, 532, and 781 nm), the Lambda 35 $\beta_{abs}$ for both TM and QF filter samples were found to be higher than the average $\beta_{abs}$ obtained by the PAS at all wavelengths, though the difference was greatest at 781 nm and smallest at 405 nm. This result may indicate that the Lambda 35 filter method overestimates the $\beta_{abs}$ at longer wavelengths. The AAE values from QF and TM were found to be lower than those from the PAS, which would be expected with the large difference found at 781 nm. This is consistent with previous studies that show the discrepancies between PAS and filter-based measurements are largest for samples containing high amounts of OC (e.g. biomass burning). Further studies comparing the Lambda 35 method with the PAS should focus on: 1) samples with low amounts of OC and 2) 24-hour ambient samples in order to reduce uncertainties in the PAS measurements. As it stands with these method comparisons, the first Hypothesis – the method can provide comparable data to PM light absorption techniques currently in use – is not well supported.

AAE values calculated from Lambda 35 measurements of source and ambient samples compare well with values reported in literature for biomass burning, diesel-exhaust, urban influence and dust transport. These source contributions were reflected in the ambient sample AAE values. Overall, the AAE values were higher for QF than TM samples, which may be due to shadowing effects on the TM filters at low wavelengths. The second Hypothesis of this study is further supported by these results.

Overall, comparisons of $\beta_{ATN}$ and $\beta_{abs}$ calculations were quite agreeable. These values were closest for BC dominated samples, as would be expected for particles that generally fall into the Rayleigh regime (scattering is essentially negligible). Comparing these values for dust and biomass burning samples showed some discrepancy at longer wavelengths. It was also notable that $\beta_{ATN}$ and $\beta_{abs}$ are more comparable for TM samples than for QF samples. This may indicate that the two-layer model and Kubelka-Munk equation solving for absorption optical depth is a more reasonable approximation for QF than TM filters. However, more rigorous investigation and optical modeling should be done to confirm this.

Linear relationships are found for attenuation (ATN), $\beta_{ATN}$ and $\beta_{abs}$ values between the paired QF and TM samples. For biomass burning and BrC-dominated samples, the TM ATN, $\beta_{ATN}$ and $\beta_{abs}$ values are, on average, approximately a third of the QF measurements. This ratio is higher for some dust source or ambient samples and for samples with higher EC contributions. Usually the slope between TM and QF is highest for the $\beta_{abs}$ relationship, but closely followed by $\beta_{ATN}$. This could mean that the

two-layer model does, however slightly, remove some filter-matrix effects because the QF and TM $\beta_{abs}$ values are more similar than the QF and TM $\beta_{ATN}$ values.

Several absorption assumptions were examined in terms of effect on radiative forcing estimates including the Lambda 35 curve, extrapolation from a long wavelength (i.e. 880 nm) data point using: 1) an AAE of 1; 2) an AAE calculated from data at 370 nm and 880 nm, and 3) an AAE calculated from a curve fit of three wavelength data points (405, 532 and 781 nm). These curves were compared to direct-beam solar radiation reaching the surface of the Earth in: 1) the arctic on the summer solstice and 2) Reno, NV, in August to compare absorption in an area seriously affected by climate changes as well as in an area under influence from wildfires, respectively. This examination showed that an AAE of 1 is rarely a good assumption, even for EC dominated samples like diesel, and that the dual- and 3-$\lambda$ methods come closer to the "true" absorption curve but still do not capture the features inherent in biomass and dust curves. Additionally, these estimates can cause large discrepancies in RF estimates between 350 and 1000 nm, especially for biomass burning and dust samples. An absorption estimate could vary by -54 to +9% for an AAE of 1, by -76 to +23% for the dual wavelength method, and by -7.3 to 5.5% for the 3-$\lambda$ method (with the removal of two dust samples that varied -15.5 to +21%). These results support the third Hypothesis – that PM absorption is not always well represented by the commonly used AAE power law assumption and extrapolation.

## 4.2 Quartz-fiber, Teflon-membrane and Loading Effects

While the heavily-loaded layered source samples created for this study did not provide as much insight into source ratio effects on absorption as originally hoped, they provided useful insight into filter matrix and loading effects encountered by filter-based light absorption measurement techniques.

As discussed previously, QF and TM attenuation, $\beta_{ATN}$ and $\beta_{abs}$ are generally linearly related with varying slopes. On average, across all samples, TM values for attenuation, $\beta_{ATN}$ and $\beta_{abs}$ are 46% of the QF values. At attenuation values exceeding 5, the relationship between the filter types was no longer linear. The attenuation of the TM filter sample plateaus as the QF attenuation continues to increase. This shift in relationship is indicative of loading effects, particularly shadowing, for TM filters.

Upon examination of the filters that had attenuation values greater than 5, the main culprit seems to be mass loading. However, the amount of mass loading that may lead to high attenuation values at higher wavelengths is dependent on the source type. It takes less mass loading of EC dominated samples to increase attenuation than it does for OC dominated samples, by nearly an order of magnitude.

## 4.3 Recommendations

While the central tenant of this study was to use archived filters, additional evaluation of this method should be obtained through studies where PM is concurrently sampled by multiple light absorption instruments, especially PAS, and onto QF and TM

filters. Comparison with a multi-wavelength aethalometer would also be useful. The PAS comparison in this study was rather limited due to Lambda 35 $\beta_{abs}$ calculation issues (which cut the number of valid filter sample comparisons to six), the nature of the source sampling (which shows large peaks for high emissions), and the source type sampled (samples containing large amounts of organic aerosol). It would be useful to compare samples containing large and small amounts of organic aerosol as well to examine collocated ambient sampling in order to reduce the uncertainties introduced by laboratory-generated source sampling.

This method could greatly benefit from examination of optical modeling with regard to filter media. General filter media comparisons and observations were made in this study but optical modeling could provide more insight into to these comparisons and observations as well as absorption calculations and assumptions. As this UV-Vis spectrometer can also measure absorption of liquid solutions, comparing measurements of the filter PM samples to measurements of PM deposits extracted in distilled de-ionized water could provide further insight into filter-matrix effects on light absorption.

Based on the comparability of the AAEs in source samples to values found in literature, this method could be useful towards determining temporal and spatial variations in source emissions. More studies should be done to further verify the utility of this method in providing absolute values for absorption or source contributions. Due to its non-destructive nature, additional experimentation and analysis of filters in comparison to other analyses would be feasible. Comparisons using the Lambda 35 and

a Fourier Transform Infrared spectrometer (FTIR) may provide additional insight into optical-chemical relationships, with the potential to identify specific chemical functional groups contributing to increased light absorption at UV and visible wavelengths.

## 5. References

Andreae, M. O. and A. Gelencser (2006). "Black carbon or brown carbon? The nature of light-absorbing carbonaceous aerosols." Atmos. Chem. Phys **6**: 3131-3148.

Arnott, W. P. (2014). "Chapter 2: Electromagnetic Theory, Refractive Index, and Definitions of Radiance, Irradiance.", from http://www.patarnott.com/atms749/index.html.

Arnott, W. P., K. Hamasha, H. Moosmüller, P. J. Sheridan and J. A. Ogren (2005). "Towards aerosol light-absorption measurements with a 7-wavelength Aethalometer: Evaluation with a photoacoustic instrument and 3-wavelength nephelometer." Aerosol Sci. Technol **39**(1): 17-29.

Bohren, C. F. (1987). "Multiple scattering of light and some of its observable consequences." Am. J. Phys **55**: 524-524.

Bond, T. C., T. L. Anderson and D. E. Campbell (1999). "Calibration and intercomparison of filter-based measurements of visible light absorption by aerosols." Aerosol Sci. Technol **30**(6): 582-600.

Campbell, D. E., S. Copeland and T. A. Cahill (1995). "Measurement of aerosol absorption coefficient from Teflon filters using integrating plate and integrating sphere techniques." Aerosol Sci. Technol **22**(3): 287-292.

Cappa, C. D., D. A. Lack, J. B. Burkholder and A. R. Ravishankara (2008). "Bias in filter-based aerosol light absorption measurements due to organic aerosol loading: Evidence from laboratory measurements." Aerosol Sci. Technol **42**(12): 1022-1032.

Chakrabarty, R. K., H. Moosmüller, W. P. Arnott, M. A. Garro, J. G. Slowik, E. S. Cross, J. H. Han, P. Davidovits, T. B. Onasch and D. R. Worsnop (2007). "Light scattering and absorption by fractal-like carbonaceous chain aggregates: Comparison of theories and experiment." Appl. Optics **46**(28): 6990-7006.

Chakrabarty, R. K., S. Pervez, J. C. Chow, S. Dewangan, J. A. Robles, G. X. Tian and J. G. Watson (2014). "Funeral pyres in south Asia: Large-scale brown carbon emissions and associated warming." Environmental Science & Technology Letters **1**(1): 44-48.

Chow, J. C., J. G. Watson, L.-W. A. Chen, M.-C. O. Chang, N. F. Robinson, D. L. Trimble and S. D. Kohl (2007). "The IMPROVE_A temperature protocol for thermal/optical carbon analysis: Maintaining consistency with a long-term database." JAWMA **57**(9): 1014-1023.

Chow, J. C., J. G. Watson, M. C. Green and N. H. Frank (2010). "Filter light attenuation as a surrogate for elemental carbon." JAWMA **60**(11): 1365-1375.

CIMEL Electronique. (2015). "CIMEL Multiband Photometer: CE318." from http://www.cimel.fr/?instrument=multi-band-sunsky-photometer&lang=en.

Clarke, A. D., C. McNaughton, V. Kapustin, Y. Shinozuka, S. Howell, J. Dibb, J. Zhou, B. Anderson, V. Brekhovskikh, H. Turner and M. Pinkerton (2007). "Biomass burning and pollution aerosol over North America: Organic components and their influence on spectral optical properties and humidification response." J. Geophys. Res. Atmos **112**(D12).

Droplet Measurement Technologies. (2014, 2014). "The Single Particle Soot Photometer (SP2)." from http://dropletmeasurement.com/single-particle-soot-photometer-sp2.

Dubovik, O., B. N. Holben, Y. J. Kaufman, M. Yamasoe, A. Smirnov, D. Tanre and I. Slutsker (1998). "Single-scattering albedo of smoke retrieved from the sky radiance and solar transmittance measured from ground." J. Geophys. Res. Atmos **103**(D24): 31903-31923.

Feng, Y., V. Ramanathan and V. R. Kotamarthi (2013). "Brown carbon: a significant atmospheric absorber of solar radiation?" Atmos. Chem. Phys **13**(17): 8607-8621.

Fialho, P., A. D. A. Hansen and R. E. Honrath (2005). "Absorption coefficients by aerosols in remote areas: A new approach to decouple dust and black carbon absorption coefficients using seven-wavelength Aethalometer data." J. Aerosol Sci **36**(2): 267-282.

Foot, J. S. and C. G. Kilsby (1989). "Absorption of light by aerosol particles: An intercomparison of techniques and spectral observations." Atmos. Environ **23**(2): 489-495.

Gorbunov, B., R. Hamilton and R. Hitzenberger (2002). "Modeling radiative transfer by aerosol particles on a filter." Aerosol Sci. Technol **36**(2): 123-135.

Hand, J. L., B. A. Schichtel, W. C. Malm, S. Copeland, J. V. Molenar, N. H. Frank and M. L. Pitchford (2014). "Widespread reductions in haze across the United States from the early 1990s through 2011." Atmos. Environ **94**: 671-679.

Hansen, A. D. A., H. Rosen and T. Novakov (1982). "Real-time measurement of the absorption coefficient of aerosol particles." Appl. Optics **21**(17): 3060-3062.

IPCC (2013). "Climate Change 2013: The physical science basis. Contribution of Working Group I to the Fifth Assessment Report of the Intergovernmental Panel on Climate Change." Cambridge University Press.

Kirchstetter, T. W., T. Novakov and P. V. Hobbs (2004a). "Evidence that the spectral dependence of light absorption by aerosols is affected by organic carbon." J. Geophys. Res. Atmos **109**(D21): D21208.

Kirchstetter, T. W., T. Novakov and P. V. Hobbs (2004b). "Evidence that the spectral dependence of light absorption by aerosols is affected by organic carbon." J. Geophys. Res. -Atmospheres **109**(D21): D21208.

Kirchstetter, T. W. and T. L. Thatcher (2012). "Contribution of organic carbon to wood smoke particulate matter absorption of solar radiation." Atmos. Chem. Phys **12**(14): 6067-6072.

Kubelka, P. and F. Munk (1931). "Ein beitrag zur optik der farbanstriche." Z. Tekn. Physik **12**: 593-601.

Lack, D. A. and C. D. Cappa (2010). "Impact of brown and clear carbon on light absorption enhancement, single scatter albedo and absorption wavelength dependence of black carbon." Atmos. Chem. Phys **10**(9): 4207-4220.

Lack, D. A., C. D. Cappa, D. S. Covert, T. Baynard, P. Massoli, B. Sierau, T. S. Bates, P. K. Quinn, E. R. Lovejoy and A. R. Ravishankara (2008). "Bias in filter-based aerosol light absorption measurements due to organic aerosol loading: Evidence from ambient measurements." Aerosol Sci. Technol **42**(12): 1033-1041.

Lack, D. A. and J. M. Langridge (2013). "On the attribution of black and brown carbon light absorption using the Angstrom exponent." Atmos. Chem. Phys **13**(20): 10535-10543.

Li, G., N. Bei, X. Tie and L. T. Molina (2011). "Aerosol effects on the photochemistry in Mexico City during MCMA-2006/MILAGRO campaign." Atmos. Chem. Phys **11**(11): 5169-5182.

Lindberg, J. D., R. E. Douglass and D. M. Garvey (1993). "Carbon and the optical-properties of atmospheric dust." Appl. Optics **32**(30): 6077-6081.

Moosmüller, H., W. P. Arnott and C. F. Rogers (1997). "Methods for real-time, *in situ* measurement of aerosol light absorption." JAWMA **47**(2): 157-166.

Moosmüller, H., R. K. Chakrabarty and W. P. Arnott (2009). "Aerosol light absorption and its measurement: A review." Journal of Quantitative Spectroscopy & Radiative Transfer **110**: 844-878.

NASA Goddard Space Flight Center. (2015). "AERONET: Aerosol Robotic Network." from http://aeronet.gsfc.nasa.gov/new_web/index.html.

Park, R. J., D. J. Jacob, N. Kumar and R. M. Yantosca (2006). "Regional visibility statistics in the United States: Natural and transboundary pollution influences, and implications for the Regional Haze Rule." Atmos. Environ **40**(28): 5405-5423.

Petty, G. W. (2006). A First Course in Atmospheric Radiation (2nd edition). Madison, Sundog Publishing.

Petzold, A. and M. Schönlinner (2004). "Multi-angle absorption photometry - A new method for the measurement of aerosol light absorption and atmospheric black carbon." J. Aerosol Sci **35**(4): 421-441.

Pitchford, M. L. and W. C. Malm (1994). "Development and applications of a standard visual index." Atmos. Environ **28**(5): 1049-1054.

Pitchford, M. L., W. C. Malm, B. A. Schichtel, N. K. Kumar, D. H. Lowenthal and J. L. Hand (2007). "Revised algorithm for estimating light extinction from IMPROVE particle speciation data." JAWMA **57**(11): 1326-1336.

Pope, C. A., M. Ezzati and D. W. Dockery (2009). "Fine-Particulate Air Pollution and Life Expectancy in the United States." New England Journal of Medicine **360**(4): 376-386.

Presser, C., J. M. Conny and A. Nazarian (2014). "Filter Material Effects on Particle Absorption Optical Properties." Aerosol Sci. Technol **48**(5): 515-529.

Russell, P. B., R. W. Bergstrom, Y. Shinozuka, A. D. Clarke, P. F. DeCarlo, J. L. Jimenez, J. M. Livingston, J. Redemann, O. Dubovik and A. W. Strawa (2010). "Absorption Angstrom Exponent in AERONET and related data as an indicator of aerosol composition." Atmos. Chem. Phys **10**(3): 1155-1169.

Sandradewi, J., A. S. H. Prevot, S. Szidat, N. Perron, M. R. Alfarra, V. A. Lanz, E. Weingartner and U. Baltensperger (2008a). "Using aerosol light absorption measurements for the quantitative determination of wood burning and traffic emission contributions to particulate matter." Environ. Sci. Technol **42**(9): 3316-3323.

Sandradewi, J., A. S. H. Prevot, E. Weingartner, R. Schmidhauser, M. Gysel and U. Baltensperger (2008b). "A study of wood burning and traffic aerosols in an Alpine valley using a multi-wavelength Aethalometer." Atmos. Environ **42**(1): 101-112.

Tombach, I. H. and M. L. Pitchford (2007). "Eliminating man-made haze in protected areas: A goal of the Regional Haze Rule." EM **12**(September): 6-11.

Tomza, U., R. Arimoto and B. J. Ray (2001). "Color-related differences in the chemical composition of aerosol-laden filters." Atmos. Environ **35**(9): 1703-1709.

U.S.EPA (1999a). "40 CFR Part 51 - Regional haze regulations: Final rule." Federal Register **64**(126): 35714-35774.

U.S.EPA (1999b). Fact Sheet: Final Regional Haze Regulations for Protection of Visibility in National Parks and Wilderness Areas.

Watson, J. G. (2002). "Visibility: Science and regulation - A summary of the 2002 Critical Review." EM **8**(June): 36-43.

Yang, M., S. G. Howell, J. Zhuang and B. J. Huebert (2009). "Attribution of aerosol light absorption to black carbon, brown carbon, and dust in China - interpretations of atmospheric measurements during EAST-AIRE." Atmos. Chem. Phys **9**(6): 2035-2050.